HIGH-DENSITY STRETCHABLE MICROELECTRODE ARRAYS: AN INTEGRATED TECHNOLOGY PLATFORM FOR NEURAL AND MUSCULAR SURFACE INTERFACING

A Thesis
Presented to
The Academic Faculty

by

Liang Guo

In Partial Fulfillment
of the Requirements for the Degree
Doctor of Philosophy in
Bioengineering

The Wallace H. Coulter Department of Biomedical Engineering
Georgia Institute of Technology and Emory University
May 2011

HIGH-DENSITY STRETCHABLE MICROELECTRODE ARRAYS: AN INTEGRATED TECHNOLOGY PLATFORM FOR NEURAL AND MUSCULAR SURFACE INTERFACING

Approved by:

Professor Stephen P. DeWeerth, Advisor
The Wallace H. Coulter Department of
Biomedical Engineering
*Georgia Institute of Technology and
Emory University*

Professor Mark G. Allen
School of Electrical and Computer
Engineering
Georgia Institute of Technology

Professor Ravi V. Bellamkonda
The Wallace H. Coulter Department of
Biomedical Engineering
*Georgia Institute of Technology and
Emory University*

Professor Adam M. Klein
School of Medicine, Department of
Otolaryngology – Head and Neck Surgery
Emory University

Professor T. Richard Nichols
School of Applied Physiology
Georgia Institute of Technology

Professor Garrett B. Stanley
The Wallace H. Coulter Department of
Biomedical Engineering
*Georgia Institute of Technology and
Emory University*

Date Approved: 24 January 2011

To my beloved wife.

ACKNOWLEDGEMENTS

In the past 5.5 years, the time when the work in this thesis was conducted, I owed many thanks to many people.

About 6.5 years ago, Prof. May Dongmei Wang's seminar presentation at my undergraduate school, Tsinghua University, introduced Georgia Tech BME to me, and I was lucky to get admitted into the prestigious Bioengineering Ph.D. Program one year later. Then, my wonderful journey at Georgia Tech started. I still remember clearly that it was Prof. Robert J. Butera who, after an interview, recommended me to Prof. Stephen P. DeWeerth, and that it was Dr. James D. Ross (then James D. Ross) and Mr. Edgar Brown from the DeWeerth group who interviewed me. And again, with some good luck, I was brought into the DeWeerth group, and the NeuroLab in general, where many fabulous things have happened since then.

I have been enjoying the freedom and leisure in the DeWeerth group. However, such freedom and leisure also made me frustrated at the beginning, because I couldn't find a research project to work on. It was Dr. Kathleen W. Meacham (then Kathleen K. Williams) who persuaded me to work in the cleanroom, which later became the second place other than the NeuroLab where I have spent most of my time. During my early days in the cleanroom, Mr. Brock Wester and Dr. Yoon-Su Choi helped me to learn the basic skills. And later, my research benefited from interactions with many people in the cleanroom, including the wonderful cleanroom manager, Mr. Gary Spinner. During my accelerating years on research, Dr. Kartik Sundar (then Kartik Sundar) helped me with learning of the frog experiment; Dr. Adam M. Klein, Miss Laura J. Kitashima, Mr. Craig R. Villari, and Miss Lindsey Arviso helped with developing the vocal cord prosthesis project. I have benefited a lot from my internship at Axion Biosystems in the summer of 2009, during which I "stole" a lot of microfabrication and electronic packaging skills that later on were reflected in my research. My research has also benefited from interactions with many other

people in the DeWeerth group, NeuroLab and other labs, including Dr. Stefan Clemens, Dr. Shane A. Migliore, Dr. Richard A. Blum, Mr. A. Scott Buscemi, Dr. Maxine McClain, Dr. Swami Rajaraman, Dr. Jianxia Cui, Dr. Isaac Clements, Dr. Laveeta Joseph, Miss Michelle Kuykendal, Ms. JoAnna Anderson, Mr. Chris Tuthill, Mr. Aaron Hughes, Miss Sarah Steinmetz, Mr. Dustin Li, Mr. Gareth Guvanason, Mr. Keith Van Antwerp, Mr. Akhil Srinivasan, Mr. Luke Beardslee, and so on.

There is no doubt that the most important person to my Ph.D. research is my thesis adviser, Prof. Stephen P. DeWeerth. I feel very lucky that I have learned to work with him intimately and efficiently, and that, at some critical moments, he pointed out the right directions for my research. He has also, through his slow pace, trained me to have improved a lot on my writing skills.

After Ph.D. proposal, my thesis committee members started to help me with further development of my research. We continued working with Dr. Klein's team on the vocal cord prosthesis project; we developed a collaboration with Prof. T. Richard Nichols' lab to study multichannel epimysial recording and stimulation on cat muscle; and we developed a collaboration with Prof. Ravi V. Bellamkonda's lab to adapt the PDMS-based sMEA technology to peripheral nerve interfacing. My thesis committee also supported my postdoctoral job hunting. Profs. DeWeerth, Allen, Bellamkonda, and Stanley wrote strong recommendation letters for me.

Besides, my research has also benefited from the collaboration with Prof. Shawn Hochman's lab on the spinal cord surface stimulation project, through which my research has been funded.

Other than research, I have significantly improved my English skills and have learned a lot of American cultures in the fantastic DeWeerth group. While immersed in busy research, I always enjoyed a breath of fresh air during our group meeting by listening to the jokes jumping on the table.

For my personal life during the past 5.5 years, I have received tremendous and intimate emotional supports from my lovely wife, Yi Li, my parents and parents in-law, as well as my younger brother. I am also very grateful to have spent many happy times with and gained

a lot of help from many good friends, such as Drs. Yi Gao, Jack Wei Chen, Zhengchun Peng, Rongwei Zhang, and many many others.

TABLE OF CONTENTS

LIST OF TABLES

LIST OF FIGURES

SUMMARY

Numerous applications in neuroscience research and neural prosthetics, such as retinal prostheses, spinal-cord surface stimulation for prosthetics, electrocorticogram (ECoG) recording for epilepsy detection, etc., involve electrical interaction with soft excitable tissues using a surface stimulation and/or recording approach. These applications require an interface that is able to set up electrical communications with a high throughput between electronics and the excitable tissue and that can dynamically conform to the shape of the soft tissue. Being a compliant and biocompatible material with mechanical impedance close to that of soft tissues, polydimethylsiloxane (PDMS) offers excellent potential as the substrate material for such neural interfaces. However, fabrication of electrical functionalities on PDMS has long been very challenging.

This thesis work has successfully overcome many challenges associated with PDMS-based microfabrication and achieved an integrated technology platform for PDMS-based stretchable microelectrode arrays (sMEAs). This platform features a set of technological advances: (1) we have fabricated uniform current density profile microelectrodes as small as 10 μm in diameter; (2) we have patterned high-resolution (feature as small as 10 μm), high-density (pitch as small as 20 μm) thin-film gold interconnects on PDMS substrate; (3) we have developed a multilayer wiring interconnect technology within the PDMS substrate to further boost the achievable integration density of such sMEA; and (4) we have invented a bonding technology—*via-bonding*—to facilitate high-resolution, high-density integration of the sMEA with integrated circuits (ICs) to form a compact implant. Taken together, this platform provides a high-resolution, high-density integrated system solution for neural and muscular surface interfacing.

sMEAs of example designs are evaluated through *in vitro* and *in vivo* experimentations on their biocompatibility, surface conformability, and surface recording/stimulation capabilities, with a focus on epimysial (i.e. on the surface of muscle) applications. Finally, as an

example medical application, we investigate a prosthesis for unilateral vocal cord paralysis

(UVCP) based on simultaneous multichannel epimysial recording and stimulation.

CHAPTER I

INTRODUCTION

1.1 Interfacing with Excitable Tissues

People with an electrical engineering background are drawn to the disciplines of physiology
and neural engineering because of two fundamental electrophysiological phenomena:

1. Neural and muscular tissues produce currents and electric potentials as reflections
   of their physiological activities. Thus by recording and analyzing these signals, the
   underlying mechanisms of these systems may be resolved.

2. Neural and muscular tissues are electrically excitable. Thus by stimulating electrically,
   the activities and outputs of these systems may be modulated and controlled.

Application of electrical engineering technologies to neural/muscular recording and stimu-
lation thus holds promise for both understanding the underlying physiological mechanisms
and providing unique diagnostic and therapeutic solutions to neurological disorders and dis-
abilities. The communications between neural/muscular tissues and electronics are made
possible through electrodes that transduce ion-based currents in neural/muscular tissues to
electron-based currents in electronics during recording, and vice versa during stimulation.

1.2 Multielectrode Array Technologies: Rigid MEAs

Historically, the majority of applications that interface with the neural/muscular systems
have used single rigid electrodes inserted into the tissue [20], which provide local extracel-
lular access to the targeted excitable cells (neurons or muscle fibers). To improve resolu-
tion and reliability of both recording and stimulation, multiple-electrode approaches have
been developed using semiconductor microfabrication techniques. These rigid-needle multi-
electrode arrays are typically fabricated using silicon, glass, and metals [135, 134, 108, 15,

1
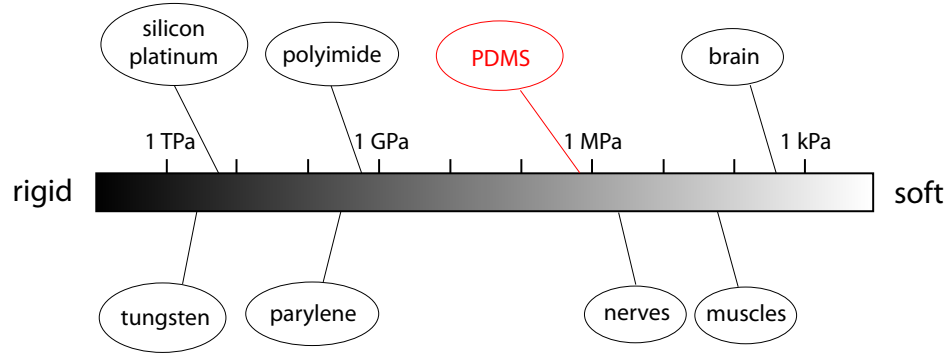
Figure 1: Young's modulus spectrum of common MEA fabrication materials and soft tissues.

60, 104], and provide access to and control of neural circuitry. As a tissue-electronics interface, a microelectrode array (MEA[1]) enables bidirectional communications with a high signal dimensionality between a biological system and an artificial electronic system.

1.3 From Rigid to Flexible MEAs

A significant limitation of the rigid-MEA approaches has been their mechanical impedance mismatch with surrounding tissues. Besides causing trauma during insertion, these devices often fail in the long run due to tissue and/or device damage caused by micro-motions between the hard materials and surrounding tissues [66]. On the other hand, studies also reveal that soft substrates promote neurite branching [7, 35]. Thus, soft MEAs are developed more recently using polymeric substrates such as polyimide [112, 40, 118, 101, 17, 74, 63], parylene [109], SU-8 [21], etc. However, with Young's moduli of ∼2.8 GPa [112], ∼4.5 GPa [109] and ∼5.6 GPa [4], respectively, these materials are still about five orders of magnitude stiffer than nerves (Young's modulus ∼60 kPa [31]) and six orders of magnitude stiffer than brain tissue (Youngs modulus ∼3 kPa [20]) (see Figure 1).

To further reduce the invasiveness of penetrating MEAs, an alternative approach of surface interfacing can be employed by using surface MEAs that interface only with the tissue surface. This approach has worked effectively in applications where reduced accessibility is

---

[1]The phrases *multielectrode array* and *microelectrode array* are often used interchangeably, as most multielectrode arrays are in microscale. I'll use the abbreviation *MEA* specifically for *microelectrode array* hereafter, and use the complete phrase *multielectrode array* to emphasize the meaning of "multiple" when necessary.
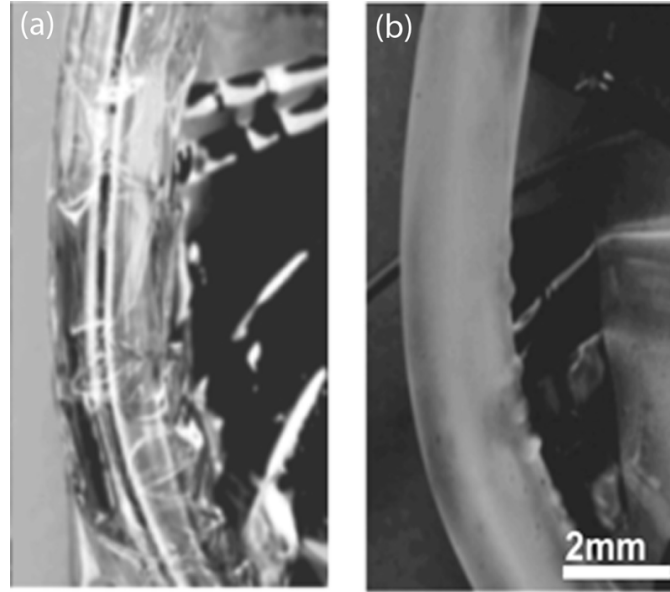
Figure 2: Comparison of conformability between polyimide and PDMS thin films [93]. Polyimide (a) and PDMS (b) thin films were wrapped around a 2 mm diameter bent tube. The PDMS film shows smoother surfaces and, therefore, better conformability than the polyimide film.

an acceptable trade-off and where the functional structures of interest are located at or close to the tissue surface. Indeed, some of these polymer-based flexible MEAs are designed as thin-film devices for surface applications [74, 109, 63]. Although these polymeric substrates exhibit a certain level of flexibility, they are not an ideal solution to the challenge of chronic surface stimulation and recording, primarily because these flexible MEAs cannot conform to the complex tissue surfaces (with the exception of using an ultra-thin film combined with a special mesh structure [63], which, on the other hand, would reduce the device's durability and limit the interconnect density).

1.4 PDMS-Based Stretchable MEA Technology

Being a truly compliant material with a Young's modulus of ∼1.0 MPa [93], polydimethyl-siloxane (PDMS, i.e., silicone rubber) offers excellent potential as the substrate material for such neural interfaces [85, 71, 116, 93]. Moreover, when used as a surface interface, the PDMS-based device also has the capability of conforming to the complex tissue surface to form a uniform and tight contact (see Figure 2). The application of compliant MEAs to neural surface recording and stimulation provides a novel and potentially powerful method

3

for both basic neuroscience research and neural prosthetics. However, fabrication of electrical functionalities on PDMS substrates has long been very challenging, particularly for achieving high-density interconnects and integrated packaging as are frequently required in neuroscience research and neural prostheses (e.g., a high-resolution retinal prosthesis requires at least $600 \sim 1000$ microelectrodes in a $\sim3~cm^2$ area [132]).

1.4.1   Challenge I: Patterning of High-Density Interconnects

The interconnect density achieved on a PDMS substrate is on the order of hundreds of micrometers [93], which is really low when compared to those achievable on silicon and other flexible substrates. The fabrication difficulties stem from the unique properties of the elastomeric substrate: (1) the coefficient of thermal expansion (CTE) of PDMS (310 ppm/°C [68] *vs.* 3 ppm/°C of silicon) is much higher than those of conventional photoresists used in microfabrication; (2) PDMS has a loose polymeric structure that allows the absorption of chemicals and significant swelling when exposed to solvents during fabrication; and (3) PDMS surfaces have poor adhesion to conventional photoresists and thin-film metals. These limitations make it particularly difficult to use conventional lithography methods to pattern high-resolution, high-density interconnects on PDMS substrates.

1.4.2   Challenge II: Implementation of Multilayer Architecture

To further boost the integration capacity and density of PDMS-based stretchable MEAs (sMEAs), multilayer implementations are needed. Although numerous efforts have been made toward multilayer implementations [120, 6, 109], a truly multilayer technology that is reliable and that has high-resolution and high-densitiy capability does not yet exist. As a result, the flexible MEAs in practical use are implemented with only a single conducting layer. The difficulty in achieving multilayer implementations on flexible/compliant substrates has significantly limited the integration capacity and density of such MEAs due to the difficulty in wiring a large number of microelectrode channels.

4

1.4.3   Challenge III: Packaging

In implantation applications, the integration of MEAs with necessary circuits is an essential requirement for considerations of reducing noise during recording and minimizing power consumption during stimulation, as well as using multiplexing to cut down the number of wires needed. The most widely used rigid MEAs [135, 134, 108, 15, 60] are fabricated using silicon substrates for the ease of adopting standard microfabrication technologies and of potential integration with necessary integrated circuits (ICs) [29, 114, 67]. While PDMS offers excellent potential for a better impedance match to soft tissues, the difficulty of reliably and compactly packaging PDMS-based sMEAs with external circuitry (such as amplifiers and stimulators alike in particular) has significantly limited the otherwise widespread application of such appealing devices. This packaging problem becomes even more significant in chronic implantation applications where a high channel-count MEA is needed, e.g. in a retinal prosthesis.

1.5   Summary

Recent trends in MEA technology for prosthetic applications have shifted from the use of rigid materials to the use of soft materials in order to better match the low mechanical impedance of soft tissues. Among the many soft materials employed as the substrate in MEA fabrication, PDMS excels in better impedance matching to soft tissues and capable of conforming to complex tissue surfaces. However, fabrication of electrical functionalities on PDMS substrates is very challenging. Three major challenges exist: (1) patterning of high-density interconnects, (2) implementation of a multilayer architecture, and (3) packaging.

This thesis focuses on addressing these challenges associated with PDMS-based microfabrication. A set of technological advances has been developed, including:

1. the fabrication of conical-well microelectrodes (as small as 10 μm in diameter), which potentially provide an improved physical contact to soft tissue surface and a uniform current density distribution during microstimulation;

2. the patterning of high-density gold interconnects on an individual conducting layer at

5

resolution of 10 μm with a pitch as small as 20 μm for both parallel and serpentine arrangements;

3. the implementation of multilayer interconnects within the PDMS substrate to facilitate the wiring of sMEAs with even higher densities;

4. the development of a multilayer *via-bonding* technology to provide high-resolution, high-density integrated packaging for such PDMS-based sMEAs.

With these advances, we are, therefore, able to offer an integrated system solution to applications involving PDMS-based neural interfaces (e.g., a PDMS-based sMEA can be directly integrated with the silicon die of an amplifier or stimulator and packaged as an integral implant for a neural prosthesis).

In Chapter II, I describe the fabrication of microelectrodes of different profiles, with a focus on conical-well microelectrodes; in Chapter III, I describe an effective lift-off method for patterning high-density gold interconnects on a PDMS substrate; in Chapter IV, I present the implementation of multilayer interconnects within a PDMS substrate for high-density wiring and between PDMS and a rigid substrate (i.e. *via-bonding*) for integrated packaging; in Chapter V, I give *in vitro* and *in vivo* evaluations of example sMEAs on their biocompatibility, surface conformability, and surface recording/stimulation capabilities, with a focus on epimysial (i.e. on the muscle surface) applications; in Chapter VI, I apply this PDMS-based sMEA technology to a prosthesis to address a clinical problem—unilateral vocal cord paralysis (UVCP); and in Chapter VII, I give conclusions of this thesis and an outlook on future neural interfacing technology.

CHAPTER II

FABRICATION OF CONICAL-WELL MICROELECTRODES

This chapter lays foundations for the latter chapters by describing the basic fabrication processes for the PDMS-based sMEA. The more advanced fabrication techniques developed in Chapters III and IV are derived from and added to this basic flow to produce sMEAs in more advanced forms.

PDMS-based sMEAs are usually fabricated as sandwiched structures [85, 71, 116, 93], where thin-film noble metal interconnects, such as platinum and gold, patterned as electrodes and leads are embedded between two PDMS layers: one as the base layer, and the other for insulation with electrodes and/or contact pads exposed through holes. The two key processes associated with the fabrication of such sMEAs are the patterning of the interconnects on the base layer and the opening of the electrodes through the insulation layer. These tasks are challenging, particularly when fabricating sMEAs of high resolution and density. While in the next two chapters I will discuss our high-density interconnect technology, in this chapter I focus on the method for effectively opening microelectrodes as small as 10 μm in diameter through the insulation PDMS layer, with the additional capability of creating a conical-well microelectrode profile that improves the sMEA's performance on neural surface interfacing.

The work presented in this chapter has been published in Refs. [52, 48].

2.1 Introduction

Stimulation-induced neural injury is an important issue in clinical applications involving chronic neural stimulation. The burning of the tissue is primarily caused by excess charge density and charge per phase [90]. In order to minimize such damage, on the electrode design side, the goal is to reduce or eliminate the non-uniformity of stimulation current density at the electrode-tissue interface. It is known that for non-recessed disk electrodes, peak current density builds up at electrode-insulator edges [102]. Recessed electrodes were reported to

reduce the excess current density at electrode edges [113, 121]. Exponentially and conically recessed microelectrodes were considered to produce a uniform current density profile during stimulation [121]. But efforts on improving this issue in the applications involving flexible MEAs have been rare, given the difficulty in fabricating microelectrodes on such substrates with uniform current density profiles.

We have developed a PDMS-based sMEA fabrication method that can achieve micro-electrodes with four different geometries, including simply recessed, conically recessed, exponentially recessed, and conical-well microelectrodes, as small as 10 μm in diameter. Among these geometries, the conical-well microelectrode that features a conical PDMS well surrounding the electrode excels in many aspects. While potentially providing a closer and sealed contact to the target tissue surface and thus achieving a more isolated microenvironment for electrical current exchange between the electrode and tissue surface, the conical-well microelectrodes can also be incorporated with an exponentially or conically recessed inner slope, making such electrodes promising in (chronic) neural surface stimulation applications that require high spatial selectivity and minimal stimulation-induced tissue damage (e.g., spinal-cord surface stimulation). In addition, the fabrication method is reliable and efficient with easy controllability over the conical well depth and recess slope.

In this chapter, we focus on the fabrication of conical-well sMEAs, and we present experimental results for electrode-profile characterization, for electrode-impedance measurement, and for conical well surface-contact testing.

2.2   Methods

2.2.1   Device Fabrication

Briefly, our fabrication process involves curing a thin layer of PDMS onto a glass slide, lift-off patterning thin-film gold interconnects, assisting in the formation of conical wells by lithographically defining sacrificial posts where electrode and contact pad openings will be, covering the sample with another thinner PDMS layer for encapsulation, and then removing the sacrificial posts to expose the electrodes and contact pads. Stepwise processes are shown schematically in Figure 3 and are described in detail below:
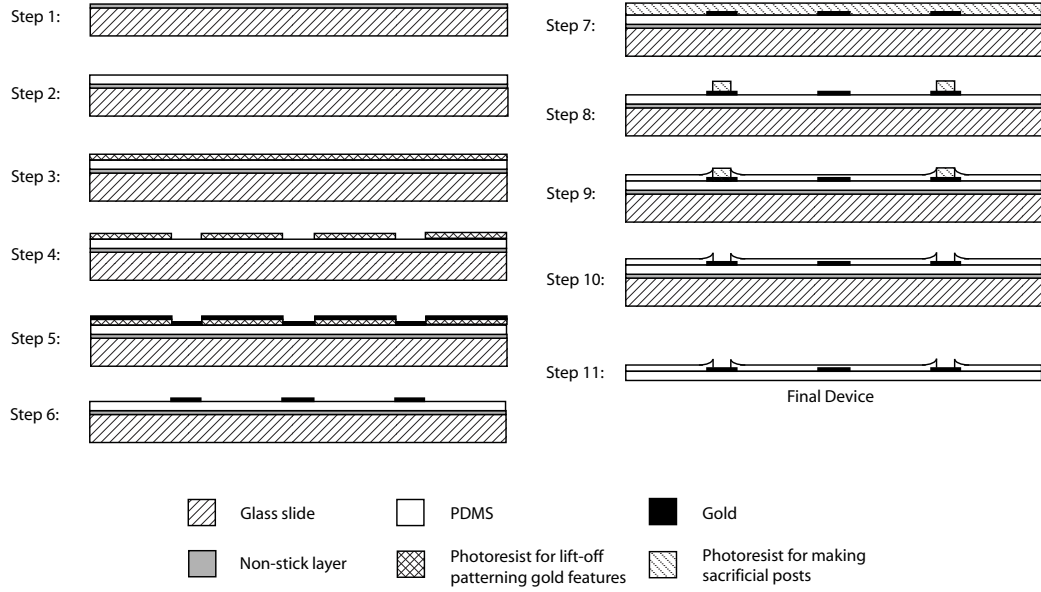
Figure 3: Schematic illustration of stepwise fabrication processes for the PDMS-based conical-well sMEA.

2.2.1.1 Preparing PDMS and Glass Slide

PDMS (Sylgard 184, Dow Corning) elastomer base is mixed with curing agent at $10 : 1$ weight ratio, and the mixture is left at room temperature for at least 40 minutes to let air bubbles rise out. A cleaned glass slide is coated with a 50 Å non-stick gold (Au) layer primed by 10 Å titanium (Ti) in an e-beam evaporator (CVC Products, Inc.), both at 3 Å/s, to facilitate device release in the end (Step 1 in Figure 3). A $\sim$70 μm PDMS base layer is formed by spin-coating the prepolymer onto the glass slide at 1500 rpm for 15 seconds with a ramp rate of 1000 rpm/s. The sample is then cured on a hotplate (Step 2 in Figure 3).

2.2.1.2 Lift-off Patterning Gold Interconnects

Two lift-off methods were developed. The first one involved the use of a positive photoresist (Shipley Megaposit SPR 220 7.0) as the lift-off mask [52, 48]. While 10 μm features were achieved, this method failed to produce interconnects with a high density (e.g., pitch smaller than 100 μm). Later, the second lift-off method was developed using SU-8, a negative photoresist, as the lift-off mask. This SU-8 lift-off method demonstrated 10-μm–wide gold traces with a pitch as small as 20 μm for both parallel and serpentine arrangements of wires as long as 3 cm [49]. In Chapter III, I will discuss this SU-8 lift-off method in detail,

9

whereas I describe the processing recipe for the SPR 220 lift-off method in Chapter IV.

Steps 3 through 6 in Figure 3 illustrate the general processes of a lift-off method. The sample is first briefly treated in oxygen plasma to activate the PDMS surface [59]. Immediately following this treatment, photoresist is spin-coated, cured, and lithographically patterned to form a mask for lift-off metallization (Steps 3 and 4 in Figure 3). Then, a gold film with a thickness in the range of 200~5000 Å is deposited at 1 Å/s in an e-beam evaporator with a priming layer of Ti that is 1/10 of gold thickness (Step 5 in Figure 3). After deposition, the photoresist mask is removed and excess gold film lifted off, leaving only the desired gold features (Step 6 in Figure 3).

2.2.1.3 Defining Sacrificial Posts

Following brief oxygen plasma treatment of the sample, a thick sacrificial layer of negative photoresist (NR5-8000, Futurrex, Inc.) is spin-coated (Step 7 in Figure 3). The sacrificial layer is patterned to leave posts right on top of each gold electrode and contact pad where an opening is to be made (Step 8 in Figure 3). The height of these sacrificial posts determines the depth of the conical electrode wells that will form (see Figure 5b). The processing recipe follows the NR5-8000 product datasheet, except that 90 ℃ is used during both softbake (60 minutes) and postbake (15 minutes) to avoid cracking gold features by high temperature.

2.2.1.4 Spin-Coating PDMS for Encapsulation

Immediately following oxygen plasma treatment, a second PDMS layer is spin-coated to encapsulate the device at 5000 rpm for 150 seconds with a ramp rate of 1000 rpm/s. The uncured sample is left at room temperature for one hour, baked on a 60 ℃ hotplate for one hour, and then baked in a 90 ℃ oven for two hours. The resulting encapsulation thickness is ~10 μm, except for the areas closely surrounding the sacrificial posts (Step 9 in Figure 3). Because of capillary effect, the PDMS prepolymer sticks and rises along the sidewalls of the sacrificial posts. The combination of spin speed, spin duration, and baking conditions is designed to disperse the prepolymer to a film thickness less than the height of the sacrificial posts [28]. Additionally, the processing recipe guarantees that the prepolymer gets rid of the top of sacrificial posts [107, 89]. These conditions and the oxygen plasma pre-treatment

are crucial for successfully achieving the conical-well structure.

2.2.1.5 Opening Electrodes and Contact Pads

To effectively remove the sacrificial posts, a brief reactive ion etcher (RIE) descum process is first applied to remove any potential thin PDMS residues on top of sacrificial posts [37], the sample is then immersed in acetone for about 10 minutes, and the electrode area is rinsed briefly with an acetone stream. Confirmation that all electrodes have been opened can be achieved through microscope inspection; subsequent acetone soaking and rinsing are applied as necessary until all electrodes are opened (Step 10 in Figure 3).

2.2.1.6 Detaching the Device from Glass Slide

The completed device is peeled off its glass slide while immersed in isopropanol, which helps to reduce stress and prevent the film from self-adhesion (Step 11 in Figure 3). Finally, the device is soaked in de-ionized (DI) water for 24 hours to remove any chemical residues that may get involved during fabrication.

Table 1: UV exposure configurations for creating sacrificial posts with different sidewall profiles

Sacrificial Post Sidewall Profile	Contact Mode between Mask and Sample	Exposure Energy (mJ/cm^2 for 1 μm)
vertical	hard	21
tapered	1 mm distance [†]	$14 \pm k \times 5/3$ [‡] ($k = 0, \pm 1, \pm 2, ...$)
exponential	1 mm distance [†]	$14 \pm k \times 5/6$ [‡] ($k = 0, \pm 1, \pm 2, ...$)

[†] A 1-mm-thick glass slide is placed between the photomask and the sample.

[‡] These exposure doses need to be calibrated based on the exposure equipment used.

11

2.2.2 Achievement of Different Microelectrode Profiles

While the emphasis of this chapter is on the conical-well microelectrode, other microelectrode geometries can also be derived from the same fabrication method by carefully controlling two critical parameters during the fabrication process: (1) the micro-shape of the sacrificial posts, and (2) the conversion between hydrophobicity and hydrophilicity of both the PDMS and sacrificial post surfaces. We employ *Aperture Diffraction* to manipulate the UV light intensity profile during the exposure process of NR5-8000 for making sacrificial posts with a tapered profile (also see Chapter IV). Furthermore, we found that the sidewall profile of the sacrificial post could be controlled by adjusting the UV exposure energy to create sacrificial posts with different sidewall slopes (see Table 1 and Figure 17a), as well as exponentially curved sidewall profiles. By varying the parameter k in Table 1 within a certain range, different sidewall slopes can be made. This enables the molding of microelectrode openings (or vias as used in Chapter IV) with complimentary geometries.

Naturally, the surface properties of cured PDMS and NR5-8000 are both hydrophobic, but they can be temporarily converted to hydrophilic upon brief oxygen plasma treatment. Brief oxygen plasma treatment of the PDMS substrate surface before passivation is necessary to ensure good adhesion between the two PDMS layers. Our observation showed

Table 2: Key parameters for fabricating different microelectrode geometries

Electrode Geometry	Sacrificial Post Shape	Sacrificial Post Height	Material Surface Property	
			PDMS (substrate)	NR5-8000 (sacrificial post)
simply recessed	vertical	any	convert to hydrophilic	back to hydrophobic
conically recessed	tapered	low	convert to hydrophilic	convert to hydrophilic
exponentially recessed	exponential	low	convert to hydrophilic	convert to hydrophilic
conical-well	any	depend on well depth	convert to hydrophilic	convert to hydrophilic

that the induced hydrophilicity of PDMS surface could last more than one day when left in air, in spite of the decrease in strength with time, and that of the negative photoresist NR5-8000 we used for making the sacrificial post could only last for less than two hours. This observation was used to independently control the surface properties of PDMS and NR5-8000 as listed in Table 2 before spin-coating the encapsulation PDMS layer.

By manipulating the thickness of the PDMS encapsulation layer and the sacrificial post parameters with respect to height, sidewall profile, and surface property, we can independently control the microelectrode geometry parameters in terms of recess depth, recess slope & profile, and protrusion/in plane. Table 2 gives the key process parameters for fabricating different microelectrode geometries on PDMS-based sMEAs.

2.2.2.1 Simply Recessed Microelectrodes

Simply recessed microelectrodes are formed by: (1) making close contact between the photomask and the NR5-8000 layer, and using the standard exposure dose ($21\ mJ/cm^2$ for $1\ \mu m$ thick film) from the NR5-8000 datasheet during the UV exposure process to create sacrificial posts with a vertical sidewall, and (2) briefly treating the sample by oxygen plasma, and leaving it in the air for two hours before spin-coating the encapsulation PDMS layer. Recess depth is determined by the encapsulation layer thickness, and does not vary with the sacrificial post height.

2.2.2.2 Conically Recessed Microelectrodes

Conically recessed microelectrodes are formed by: (1) placing a 1 mm thick glass slide between the photomask and the NR5-8000 layer, and using approximately 2/3 of the standard exposure dose ($14\ mJ/cm^2$ for $1\ \mu m$ thick film) during the UV exposure process to create sacrificial posts with a tapered sidewall, and (2) spin-coating the encapsulation PDMS layer immediately after oxygen plasma treatment of the sample. Increasing or decreasing the exposure dose by $5/3\ mJ/cm^2$ for $1\ \mu m$ thick film each step within a certain range may result in tapered sacrificial posts with different sidewall slopes. Recess depth is determined by the encapsulation layer thickness, and for planar electrodes the sacrificial posts need to be made only slightly higher than the encapsulation layer thickness.

13

2.2.2.3 Exponentially Recessed Microelectrodes

The fabrication process for exponentially recessed microelectrodes differs from that of conically recessed ones only in the exposure dose: the dose is approximately 5/6 mJ/cm^2 for 1 μm thick film less than that for conically recessed microelectrodes at each slope, resulting in slightly "underexposed" sidewall profiles.

2.2.2.4 Conical-Well Microelectrodes

Conical-well microelectrodes are formed by: (1) making high sacrificial posts, and (2) spin-coating the encapsulation PDMS layer immediately after oxygen plasma treatment of the sample, so that the PDMS prepolymer adheres and rises along the sidewall of sacrificial posts. Well depth and height of protrusion are determined jointly by both the encapsulation layer thickness and the sacrificial post height (Figure 5b). Different recess slope profiles can also be implemented within the conical-well microelectrodes.

2.2.3 Device Characterization and Evaluation

The characterization and evaluation are carried out on the conical-well microelectrodes, because of their combined capability of improving surface contact and producing a uniform current density profile during stimulation.

2.2.3.1 Conical-Well Microelectrode Profile Characterization

In order to determine the dependence of conical well depth on sacrificial post height, three sets of samples were prepared. Within each set, one sample was made with the sacrificial layer spin-coated at 400 rpm, 600 rpm, 700 rpm, 800 rpm, and 1000 rpm, respectively. The spin processes were all 30 seconds in duration with a ramp rate of 200 rpm/s. Subsequent processing parameters for the sacrificial layer, such as bake time, UV exposure dose (the standard exposure dose was used), and development time, were adjusted according to the respective thickness. Other fabrication processes were kept the same. On each sample, two five-electrode sMEAs were made. Therefore, data of thirty individual measurements on samples from three rounds of fabrication was collected for both the post height and the well depth at each spin speed. The profilometer (KLA-Tencor P15 Profilometer) settings

14

in our measurements were: scan speed of 50 $\mu m/s$, sampling rate of 50Hz, applied force of 0.5 mg, stylus tip radius of 2 μm with a 60° cone angle, and vertical range/resolution of 131 μm/0.0781 Å.

2.2.3.2   Conical-Well Microelectrode Impedance Measurement

To measure the electrode impedance, we used the same method and setup as were reported in [93]. A spectrum analyzer (SRS Dynamic Signal Analyzer, SR785) was used to sweep sine waves of an amplitude of 50 mV at frequencies from 100 Hz to 100 kHz. A custom-made voltage comparing circuit was connected to the spectrum analyzer's input channels to interface with the testing sMEAs. Electrical connections between the voltage comparing circuit and each electrode channel were accomplished by using two silver wire leads: one was pressed onto the contact pad and the other was lowered into a droplet of Hanks Balanced Salt Solution (HBSS 1X, Gibco) [(in mM): KCl 5.33, KH_2PO_4 0.441, $NaCl$ 137.93, $NaHCO_3$ 4.17, Na_2HPO_4, D-glucose 5.56, Phenol Red 0.0266], which was placed over the electrode area.

The relationship between the conical well depth (as determined by the sacrificial layer spin speed) and the electrode impedance spectrum was then quantified. One sMEA with the sacrificial layer spin-coated at 400 rpm, 600 rpm, 700 rpm, 800 rpm, and 1000 rpm, respectively, was tested. Five measurements of the electrode impedance spectrum on the five individual electrodes of each sMEA were taken. Because the PDMS surface is hydrophobic, when the sMEA is immersed in water/solution or a solution droplet is applied over the electrode area, an air bubble is usually trapped in each of the conical electrode wells, as shown in Figure 7a. This problem was mitigated by brief oxygen plasma treatment to convert the PDMS surface to hydrophilic in advance [59]. The induced hydrophilicity lasts for more than one day (our observation, as stated above), and can be preserved by storing the sample in DI water [91].

2.2.3.3   Surface Contact Performance of Conical Wells

To test the performance of conical electrode wells when contacting to a surface in solution, an sMEA (with its glass slide attached for the ease of handling and observing) was immersed

15

in DI water in a petri dish. A 25 x 25 x 0.2 mm glass slide (0.3 g) was placed over the electrodes. The conical wells were then inspected under an optical microscope.

2.3 Results

While the fabrication method can be adapted for customized sMEAs with many electrodes, sMEAs each of five electrodes (designed diameter 80 μm, minimum electrode spacing 230 μm) were fabricated for demonstration. Figures 4a and 4b show a five-electrode sMEA, and Figure 4c shows four different microelectrode geometries on four of such sMEAs. Distant scanning electron microscope (SEM) images of the exponentially recessed microelectrodes appeared to be similar to those of conically recessed ones [Figure 4c(ii)], so a close-up image is shown in Figure 4c(iv). While the thickness of the sMEAs demonstrated here and used in the following experiments was 80 μm, it can be easily set from tens of micrometers to more than one millimeter. The following sections describe experimental results on conical-well sMEA characterization and evaluation.

2.3.1 Conical-Well Microelectrode Profile Characterization

The conical-well sMEA features microelectrodes with a unique conical-well structure. To determine and measure the key fabrication parameters for such a structure, the electrode profile was characterized as the sacrificial post height was varied. The sacrificial post height is important, because the uncured PDMS prepolymer adheres to and rises along sidewall of the sacrificial post, and under the given processing conditions, a final height is achieved as a result of the balance between capillary force and gravity.

Figure 5a shows a profilometer scan along the dark line in Figure 4b. Since the profilometer probe scanned from left to right, well depths were measured as the vertical distance between Points A and B in Figure 5a. The inner wall of the well had a slightly conically-recessed shape [Figures 4c(iii) and 5a]. This shape was created by the sacrificial post, which had a complementary, tapered shape even with the standard exposure dose applied during lithography. This tapered shape is due to non-uniform UV exposure dose through the thick photoresist layer [65] (Step 8 in Figure 3). Such a particular shape provides an expected advantage of preventing the top edge of the well from bending inward into the well opening

(a)

(b)

(c)
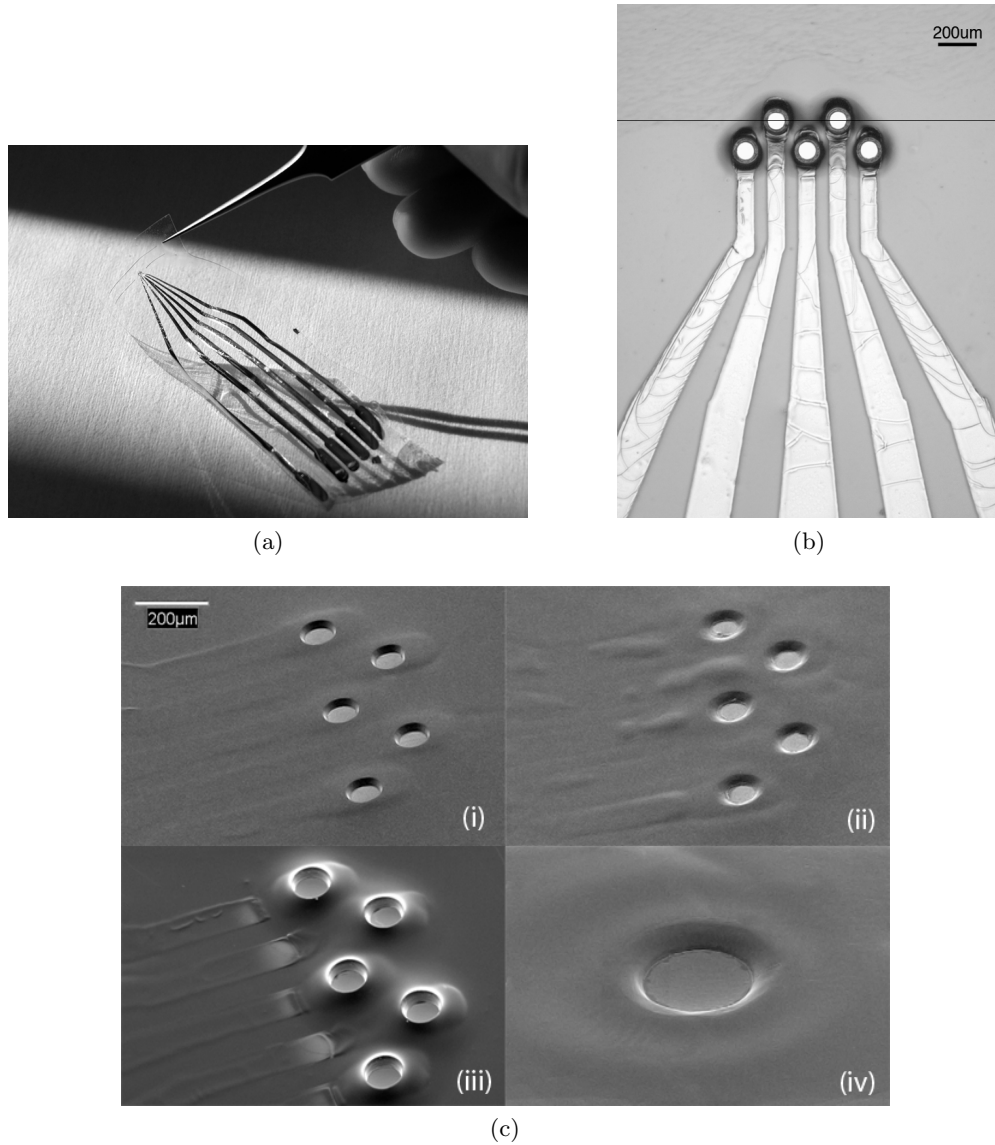
Figure 4: Images of a five-electrode sMEA at different scales. (a) The sMEA. (b) Optical microscope image of the conical-well microelectrodes. The sacrificial layer of this sample was spin-coated at 600 rpm. The dark line over the top two electrodes indicates the scanning track along which the conical-well microelectrode profiles in Figure 5a were measured. (c) SEM images of different microelectrode geometries: (i) simply recessed, (ii) conically recessed, (iii) conical-well, and (iv) exponentially recessed (close-up).

17
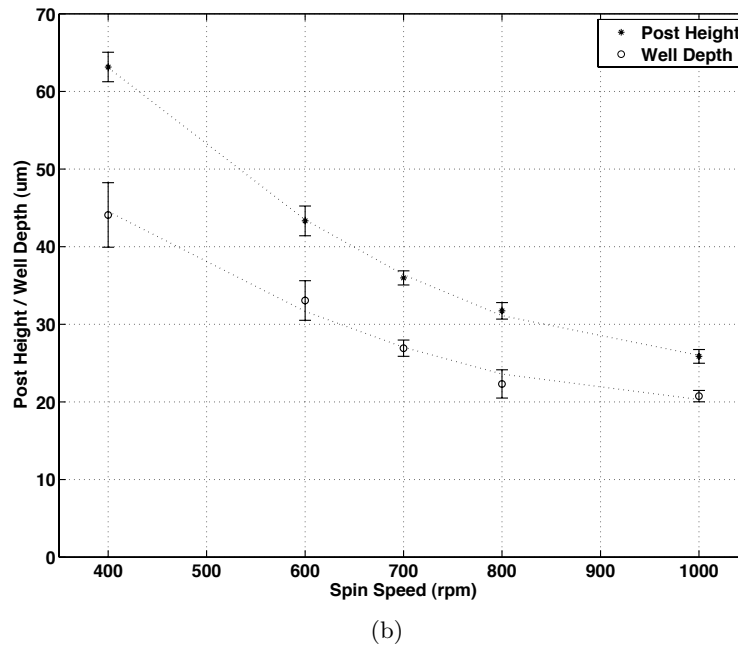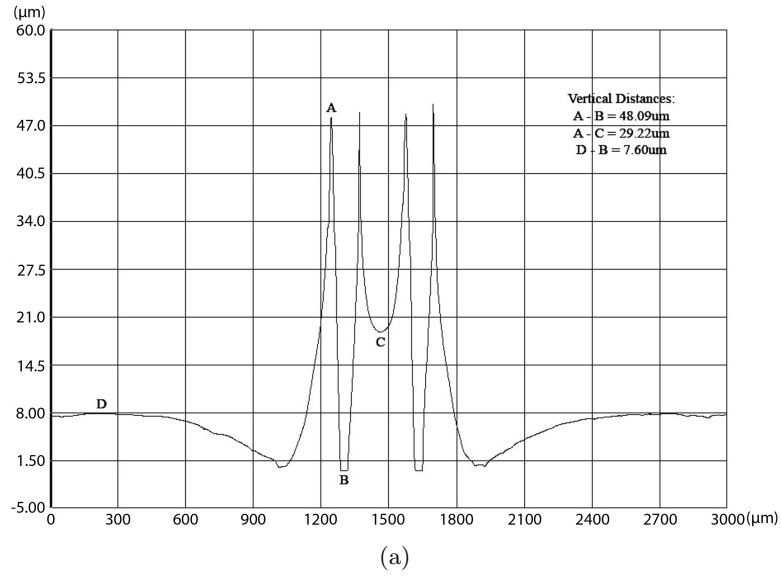
Figure 5: Characterization of the conical-well microelectrode profile. (a) A profilometer scan along the dark line in Figure 4b. The sacrificial layer of this sample was spin-coated at 400 rpm. Well depth was measured as the vertical distance between Points A and B. (b) Statistical dependence of the conical well depth on the sacrificial post height at different sacrificial layer spin speeds. Each point on the plot corresponds to measurements on 30 individual electrodes from three rounds of fabrication. Each group of data is fitted by a second-order polynomial curve (the dotted line).
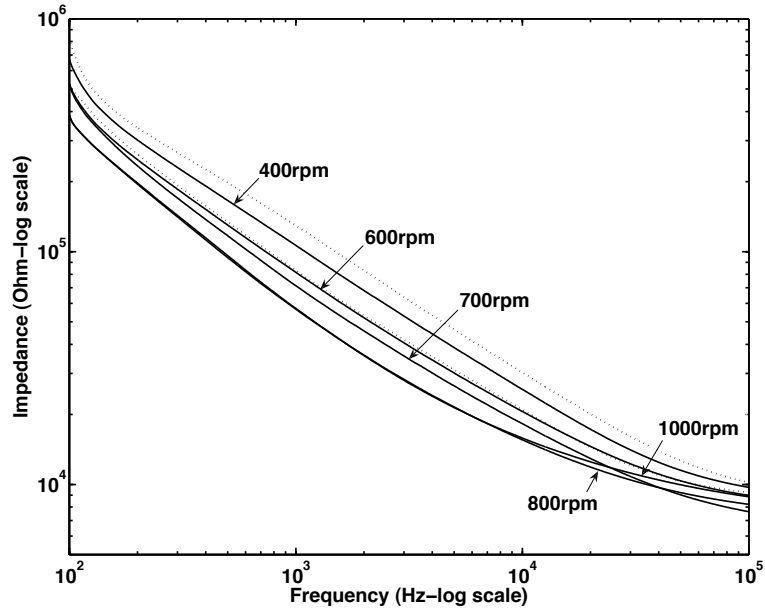
Figure 6: Electrode impedance measurement. Average electrode impedance spectra corresponding to each sacrificial layer spin speed are shown. Spectra with one standard deviation from the average electrode impedance spectrum corresponding to a sacrificial layer spin-coated at 400rpm are also shown as dotted lines.

when making contact to a surface (Figure 7b).

However, in Figure 5a, the profilometer measurement is inaccurate in reflecting both the actual slope of the inner wall and the actual electrode opening diameter, due to the relatively large size of the probe and a possible shift of the scanning track from moving along the electrode diameter. SEM measurements showed that the actual electrode diameters were $20\% \sim 40\%$ larger (depending on the depth of the well) than that was designed on the photomask, e.g., $\sim 100~\mu m$ instead of $80~\mu m$ for the sample in Figure 4. This expansion of electrode size was caused primarily by PDMS shrinking as a result of release of embedded strains after removal of the sacrificial post in acetone.

The statistical dependence of the conical well depth on the sacrificial post height at different sacrificial layer spin speeds is shown in Figure 5b. Although there appear to be large deviations at some spin speeds, it was found during data analysis that both the post height and the electrode well depth were uniform across the five electrodes of each sMEA, which is important for providing a consistent interfacial contact. Generally, a conical well depth at the value of about one electrode radius is found to have the best overall

19

performance [113, 121].

2.3.2 Conical-Well Microelectrode Impedance Measurement

Figure 6 shows the average electrode impedance spectra corresponding to each sacrificial layer spin speed, and Table 3 gives the average impedance values at 1 kHz. It is seen that, at most frequencies, the electrode impedance is higher when the spin speed is lower. Slower spin speed results in thicker sacrificial layer, which subsequently results in more significantly tapered sacrificial posts due to non-uniform UV exposure dose through the photoresist layer. Consequently, slower spin speed, which ultimately results in a smaller actual electrode opening area and a deeper electrode well, was shown to correspond to higher electrode impedances. This is because electrode impedance is inversely correlated to the actual electrode opening area and directly correlated to parasitic impedances potentially building up on the inner wall of the electrode well.

The results in Figure 6 and Table 3, on the whole, confirm the expected relationship between the sacrificial layer thickness and the electrode impedance. However, slight mismatches do exist; potential reasons for these deviations include variations in electrode surface roughness between certain electrodes, as well as the degree of presence of residues on certain electrode surfaces. Also, for sacrificial layers of close thicknesses, like those resulted from 800 rpm and 1000 rpm spins, the tapered effects were not strictly in a descending order due to potential UV over- or under-exposure. Therefore, some of the actual electrode opening areas deviated from the normal trend, causing mismatches in the statistical results.

Figure 6 together with Table 3 also indicates that the electrode impedances compare favorably to those of rigid-substrate MEA electrodes [2, 106, 53], and are relatively uniform across electrodes.

Table 3: Average electrode impedances at 1 kHz corresponding to each sacrificial layer spin speed (impedance unit: $k\Omega$)

	400 rpm	600 rpm	700 rpm	800 rpm	1000 rpm
1 kHz	106.44	81.538	71.405	56.632	57.072

20
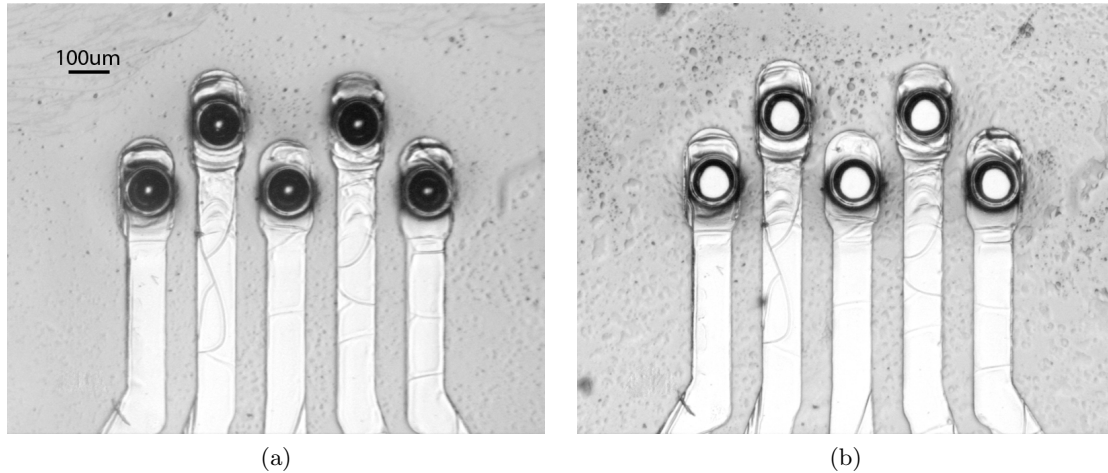
Figure 7: Surface contact performance of conical electrode wells. (a) An sMEA with its glass slide attached for ease of handling and observing was immersed in DI water in a Petri dish. An air bubble was trapped in each of the conical electrode wells due to hydrophobicity of the PDMS surface. These bubbles can be avoided by brief oxygen plasma activation of the PDMS surface in advance. (b) Interfacial contact between the conical electrode wells and a thin glass slide placed over. Air bubbles were avoided. Each electrode well formed a good seal (the light rings surrounding each electrode) on the glass surface, without any inward bending.

2.3.3 Surface Contact Performance of Conical Wells

Figure 7b shows the interfacial contact between the conical electrode wells and a thin glass slide. It can be seen that each electrode well forms a perfect seal (the light rings surrounding each electrode) on the glass surface, without any inward bending. Moreover, it was observed that when the thin glass slide was initiated a slight displacement with respect to the sMEA, the electrode wells still sealed to the original sites, despite being stretched to irregular shapes (image not shown). As a result of the conformability and elasticity of the PDMS material combined with the special structure of the electrode well, it is also expected that, in a similar manner, the conical-well electrode can potentially create a highly isolated micro-environment on the neural tissue surface, which could improve the efficacy of electrical current exchange during neural interfacing.

2.4 Discussion

2.4.1 Fabrication Considerations

Our fabrication method has demonstrated the achievement of PDMS-based sMEAs with four different microelectrode geometries, including conical-well microelectrodes. Moreover,

21

it is a clean process in that no metal wet-etching is involved, thus no etchant residue is potentially left in the device. Preliminary results showed that our fabrication method could achieve a single electrode with a minimum diameter of ∼10 μm, a 10 x 10 electrode array with a minimum electrode diameter of 20 μm (60 μm center-center electrode distance), and a single trace with a thinnest width of 10 μm. Some thoughts with regard to our fabrication method are discussed below:

2.4.1.1 Medical Grade Silicone Rubber

For clinical implantation applications, devices made with medical grade silicone are required. However, because of their high viscosity, most commercially-available medical grade silicones are difficult to spin-coat directly. Therefore, in our current fabrication, we still use a non-medical grade PDMS (Sylgard 184, Dow Corning). Schuettler *et al.* [116] reported the successful use of medical grade silicone rubber MED-1000 (NuSil, Carpinteria, CA, USA) diluted with n-heptane (Ajax Chemicals Ltd, Sydney, NSW, Australia) at a volume ratio of 1 : 1, suggesting a solution of diluting high viscosity medical grade silicone rubber by a proper liquid. In addition, in a pilot experiment, we successfully transferred our fabrication method to a low-viscosity medical grade silicone, MED-6215 (NuSil, Carpinteria, CA, USA).

2.4.1.2 Acetone Effects on PDMS

It was interesting that while we found acetone could not be used for stripping in our lift-off process (because it deformed the PDMS substrate and caused gold features to be stripped off), we could use it to remove sacrificial posts for opening electrodes and contact pads. Our encapsulated devices were found robust enough to withstand being soaked in acetone for an hour during sacrificial post removal! It was believed that the surface properties of PDMS in the encapsulated device changed following our processing, which made it harder for acetone to get into the polymer. Nevertheless, PDMS thin films are not suitable to be soaked in acetone for too long. About an hour would be the maximal limit, and longer immersion may cause PDMS to be 'dissolved' by acetone.

22

2.4.1.3 Sacrificial Posts for Opening Electrodes and Contact Pads

The selection of a suitable photoresist for making sacrificial posts depended on several key factors. The associated processing of the chosen photoresist needed to be compatible with the PDMS substrate and previous processes. Also, the chosen photoresist needed to be PDMS-philic (after oxygen plasma activation) for the formation of electrode wells and capable of producing features with superior resolution and aspect ratio. Finally, the photoresist needed to be removable with a compatible process in the end. After exploration, we finally found the negative photoresist NR5-8000 (Futurrex, Inc.) could meet all the above requirements.

2.4.2 Advantages of Conical-Well Electrodes

The major perceived advantage of the conical-well electrode is its potential to provide an optimal functional interface with soft tissue. Evidence of this potential is provided in detail below, and are described in relation to our investigations concerning the physical, electrical, and mechanical attributes of such sMEAs.

2.4.2.1 Providing Good Suction Interface for Surface Contact

As demonstrated in Figure 7b, when contacting to a flat glass surface, the conical electrode wells each formed a tight seal. In a similar manner, it is expected that conical-well microelectrodes, when interfaced with soft tissues, would provide an interface with a more isolated micro-environment for current exchange between the electrode and tissue surface. With this seal, little current leakage should occur, and stimulation would be more power-efficient with improved spatial selectivity. However, more sophisticated experiments need to be designed to further investigate such a potential.

2.4.2.2 Producing Uniform Current Density Profile

For near-field electrical stimulation, in which the targeted tissue is immediately adjacent to or in direct contact with the electrode surface, charge density (the product of current density and pulse duration), together with charge per phase, is considered responsible for stimulation induced neural damage [90]. Excess current density at the electrode surface

can also cause electrode damage by initiating irreversible electrochemical reactions. Safe stimulation levels are thus set by limiting the maximum average current density at the electrode surface and the maximum average charge injection into the tissue per phase.

For non-recessed disk electrodes, peak current density builds up at electrode-insulator edges [102]. Theoretical analyses [113] and experimental measurements [121] have demonstrated that excess current density at the electrode edges can be reduced or eliminated by recessing the electrode into the carrier, creating a welled electrode, and by radially varying the recess. Thus, recessed electrodes could significantly reduce tissue damage by preventing the electrode surface from irreversible electrochemical reactions and by protecting the targeted tissue from being exposed to high peak current densities.

Our conical-well electrode features a conical recess, which is molded by a tapered sacrificial post. The recess slope can be set by controlling sidewall slope of the sacrificial post, and the recess depth can be set by controlling height of the sacrificial post (Figure 5b). Uniform distributions of current density are expected at both the electrode surface and the conical-well aperture where an interface junction is to be made with the target tissue surface [121]. Not only will current be released uniformly across the electrode surface, thereby minimizing electrode damage, but also the maximum amount of current can be injected uniformly across the conical-well aperture into the targeted tissue, thus maximizing activation capability while minimizing direct tissue damage normally caused by edge-induced excess peak current densities.

2.4.2.3 Protecting Electrodeposited Material

Previous work has demonstrated that platinum-black [11, 36], iridium oxide [96], and conducting polymers [23, 24] can be electrodeposited onto the electrode surface. Such electrodeposition benefits electrode designs by reducing the electrode impedance and increasing the charge injection capability. The conical-well structure is expected to facilitate such electrodepositing efforts by protecting the deposited material from mechanical removal. However, the deposited rough material in the well could disturb the uniformity of current density

distributions. Therefore, a tradeoff between electrode impedance reduction, charge injection increase, and current density uniformity must be optimized. This can be accomplished by appropriate control of material deposition and by adjusting the conical well profile with respect to well depth and recess slope.

2.4.3 Potential Applications

Most electrical stimulation applications would benefit from the conical-well electrode feature, because its uniform current-density profile provides the advantage of minimal tissue damage and electrode corrosion; this advantage is particularly important for chronic implantation. For recording applications, the conical wells have the potential to facilitate better-isolated electrodes, thus reducing leakage and noise and increasing signal fidelity.

Although we have used the compliant PDMS (Sylgard 184, Dow Corning) as both the substrate and encapsulation materials and have used gold to make the interconnects, the fabrication technique also has the potential for implementing conical-well MEAs on other substrates, either rigid or flexible, and with other metals or conducting polymers used for the interconnects. The advantages of conical-well MEAs fabricated using other materials would open the technology to a broader range of applications. For example, silicon, glass, or polyimide can be used for the substrate, and SU-8, polyimide or PDMS can be used for encapsulation; the resulting planar devices would have applicability to *in vitro* applications—such as brain-slice studies—in which the uniform current density profile and potentially higher signal fidelity of the conical wells can be exploited.

2.5 Summary

In this chapter, we have described a basic flow for the fabrication of PDMS-based sMEAs. This flow serves as the foundation for the more advanced fabrication techniques presented in the next two chapters. Moreover, the fabrication technique presented in this chapter can achieve microelectrodes with four different geometries, including simply recessed, conically recessed, exponentially recessed, and conical-well microelectrodes, as small as 10 μm in diameter. Among these geometries, the conical-well microelectrode that features a conical PDMS well surrounding the electrode excels in many aspects. While potentially providing

25

a closer and sealed contact to the target tissue surface and thus achieving a more isolated microenvironment for electrical current exchange between the electrode and tissue surface, the conical-well microelectrodes can also be incorporated with an exponentially or conically recessed inner slope, making such electrodes promising in (chronic) neural surface stimulation applications that require high spatial selectivity and minimal stimulation-induced tissue damage (e.g., spinal-cord surface stimulation). In addition, the fabrication method is reliable and efficient with easy controllability over the conical well depth and recess slope. The example sMEA was characterized and evaluated with respect to microelectrode profile, electrode impedance, and surface contact performance of conical wells.

CHAPTER III

PATTERNING OF HIGH-DENSITY GOLD INTERCONNECTS

While in Chapter II I described the method for microelectrode formation on an sMEA, in this chapter I start to describe the other key process of PDMS-based sMEA fabrication—the patterning of high-density interconnects.

A real high-density interconnect technology should consist of two essential aspects: (1) the capability of producing high-density interconnects on an individual conducting layer, and (2) the capability of going to a multilayer implementation. In addition, a high-resolution, high-density packaging technology is always an essential complement to the high-density interconnect technology. In this and the next chapters, I describe our developments of a complete set of high-density interconnect technology on the PDMS substrate. An effective lift-off method for patterning high-density gold interconnects on an individual layer of PDMS is covered in this chapter, while methods for implementing multilayer interconnects and integrated packaging are described in the next chapter.

The work presented in this chapter has been published in Ref. [49].

3.1   Introduction

Many challenges hinder the implementation of electronics on an elastomeric substrate with integration density and capacity comparable to those achievable on a silicon substrate. As stated in the Chapter I, three major challenges under consideration in this thesis are: (1) patterning high-density interconnects on an individual conducting layer, (2) achieving multilayer interconnects within the elastomeric substrate, and (3) reliably and effectively packaging the soft electronics with standard rigid electronics. The first issue is covered in this chapter, and the second and third are addressed in the next chapter.

For the first issue, the patterning of single 10 μm wide gold traces on PDMS substrates has been achieved with both wet-etching [93, 1] and lift-off methods [52], but fidelity and

viability diminish as interconnect length and density increase. Although the wiring of high-density devices such as MEAs frequently requires interconnects with these characteristics, no (universally) effective solution for patterning on elastomeric substrates has been reported so far. Therefore, the focus of this chapter is to present an effective method for patterning high-density thin-film gold interconnects on the PDMS substrate. We have demonstrated 10 μm wide gold traces with a pitch as small as 20 μm for both parallel and serpentine arrangements of wires as long as 3 cm. This approach provides more than one order of magnitude improvement on the density of interconnects patterned previously on elastomeric substrates [85, 71, 93, 1, 52, 89].

3.2 Approaches

There are many methods for patterning interconnects on PDMS, including shadow masking [71], wet etching [93, 1], lift-off metallization [50, 52, 89], laser cutting [116], pattern transfer [43], and printing/stamping [124, 14, 64], among which we find the lift-off method to be the best for patterning high-density interconnects on PDMS. This is because shadow-masking, laser-cutting, pattern-transfer, and printing/stamping methods are ultimately limited in feature resolution and density, and the wet-etching method can cause problems with PDMS curing and biocompatibility [52]. In contrast, lift-off metallization has the following advantages: (1) fabrication compatibility for easy integration with other microfabrication processes to achieve devices with complex architectures, (2) capability of producing high-resolution, high-density features without limitations on pattern design (e.g. connected patterns as required by the shadow-masking method), and (3) no or limited exposure to contamination from etchant residuals, which is a mandatory requirement for neural implants. However, material considerations limit the application of traditional lift-off processing used with rigid substrates to PDMS-based fabrication.

The fabrication difficulties stem from the unique properties of the elastomeric substrate. First, the CTE of PDMS (310 ppm/℃ [68] *vs.* 3 ppm/℃ of silicon) is much higher than those of conventional photoresists used in microfabrication. As a result, when applied on

28

the PDMS substrate, these photoresists, which are optimized for application on rigid substrates (e.g. silicon and glass wafers), develop severe cracks in the film after softbake due to shrinking of the PDMS substrate. These cracks thus render the photoresist mask unusable. Second, PDMS has a loose polymeric structure that allows the absorption of chemicals and significant swelling when exposed to solvents during fabrication. The absorbed chemical residuals (e.g. etchant residuals) in the PDMS substrate can cause severe problems with regard to toxicity as well as the curing of subsequently applied negative photoresists and layers of PDMS [52]. While conventionally used as a stripper in lift-off metallization, acetone is readily absorbed by PDMS, which causes severe swelling and consequently prevents its use in lift-off processing with PDMS. This makes it hard to remove the photoresist mask after metallization. Third, PDMS surfaces have poor adhesion to conventional photoresists and thin-film metals. This limitation makes it particularly difficult to lithographically pattern high-resolution, high-density photoresist features on the PDMS substrate, as the fine photoresist features would easily peel off or delaminate from the substrate during development. Moreover, because of the poor adhesion of thin-film gold to the PDMS substrate (even with an adhesion layer of Ti), fine gold features are likely to also delaminate from the PDMS substrate when immersed in liquids like solvents, solutions, and etchants.

In order to use the lift-off method to pattern thin-film gold interconnects on the PDMS substrate, the following requirements need to be met to address the above issues associated with PDMS-based fabrication: (1) To avoid or dramatically reduce cracking, the photoresist used as the lift-off mask needs to have a CTE close to that of PDMS and to be strong enough to tolerate the strain developed from shrinking of the PDMS substrate during cooling down as a result of the CTE difference. (2) The patterned photoresist needs to have good adhesion to the PDMS substrate when immersed in its developer during development, especially for patterned photoresist stripes with dimensions that are very thin and long. (3) And, the photoresist needs to be easily removed during the lift-off process without interacting with or damaging the PDMS substrate and the desired gold features.

With these requirements in mind, we have used the negative photoresist SU-8 (CTE = 52 ppm/°C [126]), which is a common microfabrication material but has rarely been used for

SU-8 Lift-Off Method
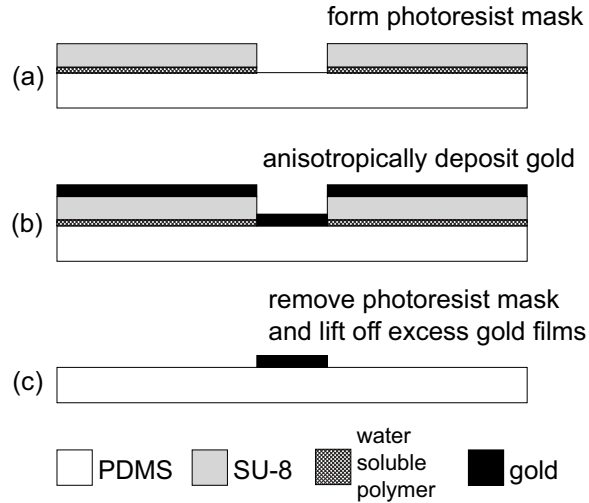
Figure 8: Lift-off method using SU-8 as the photoresist, water soluble polymer (PAA) as an intermediate sacrificial layer, and DI water as the terminal stripper. Thin-film gold is anisotropically deposited using an electron beam evaporator.

lift-off processing before. SU-8 is well-known for its capability to produce high-resolution, high-density and high-aspect-ratio features, and it adheres to PDMS strongly [137]. However, exposed and polymerized SU-8 is hard to remove; without an intermediate (sacrificial) layer, the separation of SU-8 from PDMS is difficult. Fortunately, the water soluble polymer, poly(acrylic acid) (PAA, whose dry form is used as the superabsorber in baby diapers), is reported to have good properties as a sacrificial layer for lifting off SU-8 patterns [82]. PAA dissolves rapidly in water but is insoluble in γ-butyrolactone and 1-methoxy-2-propanol-acetate (PGMEA), which are the solvents for the prepolymer resin and the developer, respectively, for bis-phenol-A-formaldehyde epoxy-based SU-8 (MicroChem Corp). Therefore, we propose a lift-off method (Figure 8) involving the use of SU-8 as the photoresist, PAA as an intermediate sacrificial layer, and DI water as the terminal stripper for patterning high-resolution, high-density thin-film gold interconnects on the PDMS substrate.

PAA adheres well to oxygen plasma treated PDMS surface, and SU-8 also adheres strongly to PAA. However, cured PAA films are brittle and vulnerable to cracking when subject to strains. By spin-coating PAA into a thin film ($\sim$400 nm) on PDMS, we have

mitigated any cracking from baking. This thin PAA film is unaffected by the photolithographic processes (spin-coating, baking, UV exposure, and development) of SU-8, and the presence of this PAA intermediate layer helps to limit the solvents (γ-butyrolactone and PGMEA) from accessing to the bulk PDMS substrate. Furthermore, PAA in the exposed areas can be easily removed by brief oxygen plasma. These properties of PAA as a sacrificial layer allow the use of SU-8 for patterning a lift-off mask with high-resolution, high-density features on the PDMS substrate, as illustrated in Figure 8a.

Following thin-film coating of PAA, patterning of SU-8, plasma etching of exposed PAA, and gold evaporation (Figure 8b), the lift-off process is finally accomplished in DI water. Extensive/extended soaking of the sample in DI water to allow for complete dissolution of the PAA layer does not induce delamination of the desired fine gold features from the PDMS substrate. This observation implies that interactions of water molecules alone with the PDMS–Ti–gold interface have minimum effect on delaminating the gold thin film, whereas interactions from solvent molecules or ions, which potentially enter the spaces between PDMS, Ti and gold as a result of the loose structure of PDMS, have an apparent effect on delaminating the gold film [52]. Additionally, SU-8 photoresist undercuts formed from hard or soft mask contact modalities during lithography significantly speed up the development process, allowing the SU-8 film to be gently peeled off the sample using a pair of tweezers after soaking for 30 minutes in DI water, leaving the patterned gold features (Figure 8c).

Conventional SU-8 softbake and postbake protocols (e.g. softbake and postbake on a 90 °C hotplate without temperature ramping [10]) were adopted from recipes used for rigid substrates. While no cracks appeared in the SU-8 film prior to development, a variety of problems from the PDMS–PAA–SU-8 interface emerged during development, prohibiting the yield of a successful SU-8 mask. Figures 9a – 9c shows the three typical problems observed after development: micro cracks in the bulk film, a major micro crack in the right-angled corner, and distortions in the SU-8 stripes, respectively. These three problems were all found to be caused by the large amount of strains embedded in the SU-8 film. During development, unexposed SU-8 was removed, and this led to imbalanced localized strains in the SU-8 film where feature edges appeared. As a result of the low mechanical modulus of

31
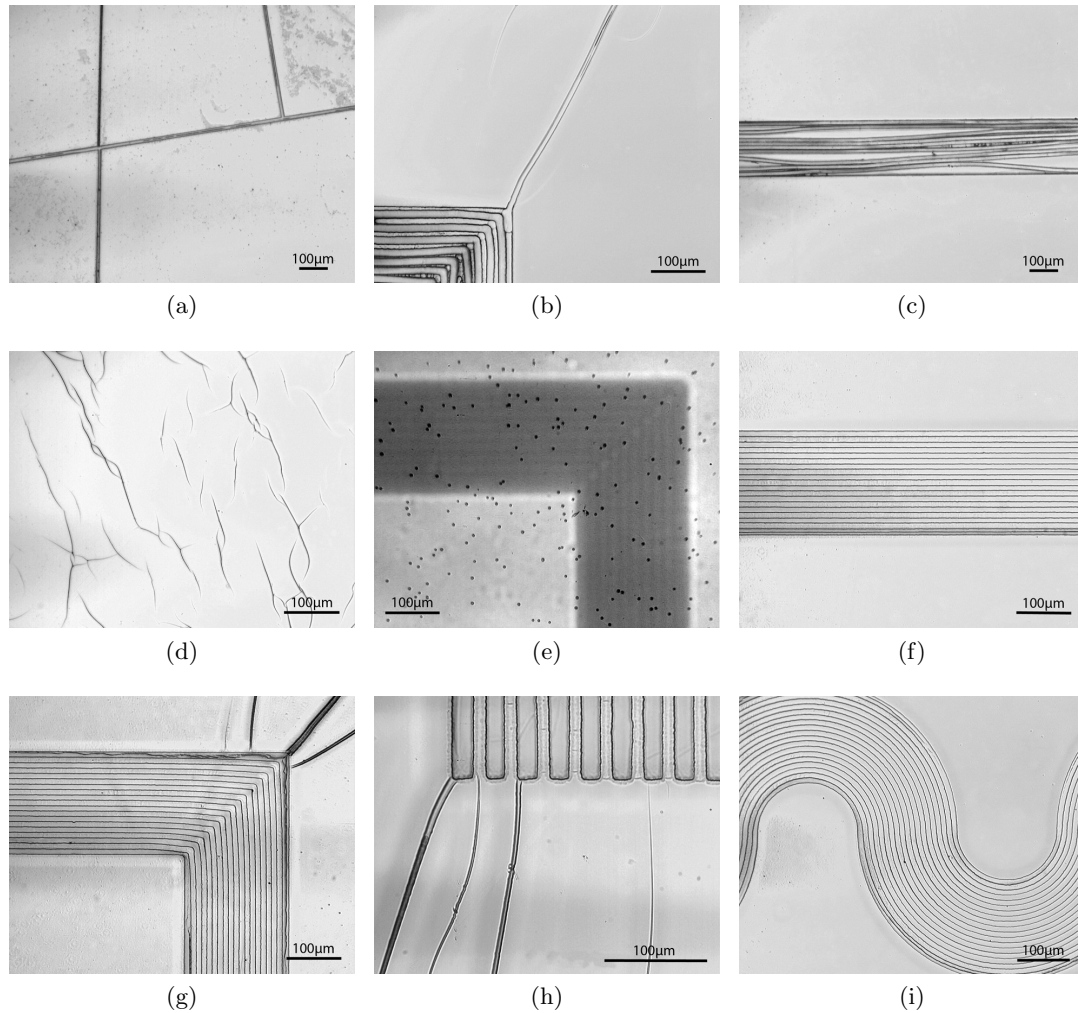
Figure 9: Patterning SU-8 lift-off mask on the PDMS substrate. (a) – (d) Problems after development. The softbake (10 minutes) and postbake (5 minutes) were done on a 90 ℃ hotplate without temperature ramping up and down. (a) Micro cracks in the bulk SU-8 film. The residuals were a result of insufficient development and IPA rinse. (b) A major micro crack in the right-angled corner. (c) Pattern distortions. (d) "Nano" cracks in the bulk SU-8 film. (e) Nano air bubbles in the polyester film, imaged from the opposite side of the emulsion ink. The other side is the pattern of traces with 10 μm width and 20 μm pitch. (f) – (i) Improved SU-8 lift-off mask. The processing recipe is detailed in the *SU-8 Lift-Off Method* section below. A polyester film photomask was used in lithography with vacuum contact mode on the mask aligner. (f), (g) and (i) Snapshots of parallel traces, corners, and serpentine traces of 10 μm width and 20 μm pitch, respectively. The darker traces in the exposed areas of the peripheral lines were imprints of PAA cracks on PDMS. The PAA cracks were caused by intensive imbalanced strains in the adjacent SU-8 bulk film after development. PAA in the exposed areas were already removed by brief plasma etching. (g) Imbalanced strains aggregated at the corner tore the film slightly apart. (h) Terminals of traces of 20 μm width and 30 μm pitch. The vertically nonuniform cracks starting from the bottom surface of the SU-8 film didn't go through the top surface of the film.

the PDMS substrate, mechanical deformations of the exposed and polymerized SU-8 were allowed to partially release the embedded strains, which subsequently caused cracks and distortions in the pattern. We hypothesized that reducing the embedded strains in the SU-8 film would mitigate the above problems.

Because the glass transition temperature T_g of unexposed SU-8 is approximately 50 °C [10], a softbake and postbake temperature of 60 °C was selected to reduce the thermal strain. Further experiments revealed that temperature ramping up and down during baking further reduced thermal stressing (see the *SU-8 Lift-Off Method* section for details). Figures 9f – 9i shows parallel traces, right-angled corners, trace terminals, and serpentine traces respectively in the improved SU-8 lift-off mask. While the remaining aggregated strains at right-angled corners were still large enough to tear the SU-8 film (Figures 9g and 9h), the cracks were more prominent at the lower level of the SU-8 film. Most of these cracks did not travel through the whole film (Figure 9h) and thus would minimally affect the patterning of features. The vertically non-uniform cracking was a consequence of the non-uniformly embedded strain through the SU-8 film, with the upper level having lower strain than the lower due to less constraint on reflow during slow baking. Nonetheless, the selective use of rounded corners over hard corners could be designed, as the serpentine patterns showed little cracking (Figure 9i).

Another concern in the fabrication of photoresist lift-off masks is the tradeoff between high-resolution, high-density features and undercuts on photoresist feature sidewalls for an effective lift-off. Reproducibly good undercuts is one of the critical reasons for the widespread use of negative photoresists in lift-off processes. The undercut can be easily achieved during photolithography by using a non-intimate contact between the photoresist and photomask (e.g. hard contact mode on a mask aligner) combined with slight underexposure. However, with a non-intimate contact (i.e., an air gap ranging from tens of microns to more than one hundred microns will exist between the photoresist and photomask), the diffraction phenomenon of UV light starts to play an important role during lithography. Instead of a sharp boundary, the light intensity profile extends a tail from the dark-clear edge into the shadow area [19]. For negative photoresists, diffraction reduces dimensions

of the unexposed features, which becomes more problematic when the unexposed features are small (as is the case for patterning the 10 μm wide traces in Figure 12b). Diffraction could also cause aliasing of the UV light intensity at the photoresist surface in the case of fine features that are densely arranged with small gaps. To faithfully pattern interconnects at a very high resolution and density (e.g. 10 μm lines spaced by 10 μm gaps), intimate contact (vacuum contact mode on a mask aligner) was used during UV lithography, but a thinner 50 nm gold film (with an adhesion layer of 5 nm Ti) was deposited to ease the lift-off. For widths of traces and gaps no smaller than 20 μm, non-intimate contact (hard contact mode on a mask aligner) was used, and thicker gold films ($\geq$ 100 nm, Ti : Au = 1 : 10) were deposited.

We used a 10 μm thick SU-8 film as the lift-off mask, which we found to be more robust than thinner ones when peeling it off using a pair of tweezers. To take advantage of underexposure for creating better undercuts and for avoiding exposure aliasing for high-density features, for a 10 μm SU-8 film, we found that the UV exposure threshold was approximately 40 mJ/cm^2. Excessive underexposure was found to be one of the causes of "nano" cracks in the bulk SU-8 film during development [97] (Figure 9d). Other causes included nano air bubbles in the polyester film photomask (Figure 9e), grains embedded in the SU-8 film (Figure 9d), and large embedded strains in the SU-8 film. Underexposure caused insufficient polymerization of SU-8 during postbake and resulted in a weak SU-8 film. Both nano air bubbles in the polyester film photomask and grains in the SU-8 film scattered the UV light during exposure, which led to non-uniform and more attenuated exposure in the local areas. Grains also caused inconsistency in the SU-8 structure and thus induced additional irregular localized strains. Subsequently during development, the creation of imbalanced embedded strains in the patterned SU-8 film (as discussed above) generated the "nano" cracks. This problem was mitigated when we increased the UV exposure dose to 60 mJ/cm^2 and used chrome-plate photomasks (Soda Lime, 0.06" thick, Nanofilm, CA and Photo Sciences, Inc., CA). We initially ordered polyester film photomasks (JD Photo-Tools, UK) and transferred the patterns onto raw chrome-plate masks (Soda Lime, 0.06" thick, Nanofilm, CA) in-house. To avoid the additional dimension errors introduced by the

34

transfer, we used the polyester film photomask during our calibration and evaluation of the fabrication processes. We found that most of the "nano" cracks did not go through the SU-8 film, as little gold was left on the PDMS substrate at the crack patterns after lift-off. Nonetheless, for high-resolution, high-density patterns, direct-write chrome-plate photomasks are more effective.

One last point worthy of mention for successfully patterning high-resolution, high-density SU-8 features on PDMS is gentle handling of the sample during the SU-8 development process. To avoid introducing any potential mechanical distortions to the fine features, no agitation was applied during development, and sample rinsing was done by a gentle isopropanol (IPA) stream, followed by air drying the sample. Insufficient development and IPA rinse would leave residuals on the sample (upper right corner, Figure 9a). Without an IPA rinse, clots of dried SU-8 developer (MicroChem Corp) would contaminate the mask and cause failure regions in the lift-off. Moreover, as is sometimes recommended with SU-8 patterning, a DI water rinse should be avoided; especially considering that the rapid dissolution of the water-soluble PAA causes delamination of the fine SU-8 features.

3.3   Materials and Methods

3.3.1   Materials

PDMS (Sylgard 184) was purchased from a distributor of Dow Corning Corp. SU-8 2007 and SU-8 Developer were purchased from MicroChem Corp. PAA (50 kDa) was purchased from Polysciences, Inc. (Warrington, PA) as a 25% (w/v) solution in water, and diluted with DI water to 10% (w/v) [82].

Polyester film photomasks were self-designed using AutoCAD 2007 (Autodesk, Inc.) and ordered from JD Photo-Tools, UK. The patterns were also transfered onto raw chrome-plate masks (Soda Lime, 0.06" thick, Nanofilm, CA) in-house using a Karl Suss MA-6 Mask Aligner with vacuum contact mode. High-resolution chrome-plate masks (Soda Lime, 0.06" thick) were self-designed and directly ordered from Photo Sciences, Inc., CA.

3.3.2   SU-8 Lift-Off Method

PDMS was prepared by mixing the base and curing agent at 10 : 1 weight ratio. The prepolymer was left at room temperature for 40 minutes for the dissipation of air bubbles. The de-aired prepolymer was spin-coated onto a cleaned glass slide (pre-coated with 1 nm Ti/ 5 nm Au) for the desired thickness [87] (70 μm in the current experiments) and cured on a hotplate. Following brief oxygen plasma treatment of the PDMS surface, PAA 10% (w/v) solution was spin-coated at 4000 rpm for 15 s and baked on a hotplate at 60 ℃ for 5 minutes to yield a film of ∼400 nm [82]. The sample was cooled down for 2 minutes, and SU-8 2007 was immediately spin-coated at 1500 rpm for 30 s. Then the sample was placed on a hotplate slowly ramping from room temperature to 60 ℃ at a rate of 5 ℃/hour, held for 1 hour, and then cooled down to room temperature by automatically turning off the hotplate. The resulting SU-8 thickness was ∼10 μm. In the photolithography process, the sample was patterned with a UV exposure dose of 60 mJ/cm^2, post-baked on a hotplate at 60 ℃ for 30 minutes with a ramp up rate of 5 ℃/hour from room temperature, cooled down to room temperature by automatically turning off the hotplate, developed in SU-8 Developer for ∼150 s, gently rinsed with an IPA stream, and dried in air. It was necessary to leave the sample in air for at least 12 hours to allow the solvent residues to fully evaporate. PAA in the exposed areas was then removed using brief plasma etching ($O_2/SF_6 = 20/1$, 150 mTorr, 200 mW, 1 minute) (Figure 8a). 50 ∼ 500 nm gold was deposited in an e-beam evaporator at 1 Å/s with a Ti adhesion layer of 1/10 gold thickness (Figure 8b). The lift-off was done in DI water. After soaking for a few hours, the SU-8 film was gently peeled off in DI water using a pair of tweezers, leaving the patterned gold features (Figure 8c).

3.3.3   Impedance Spectroscopy

To test electrical properties of the 10 μm wide, 20 μm pitch parallel traces, which is the currently achievable fabrication limit, a new chrome-plate mask was ordered commercially (Photo Sciences, Inc., CA). Two classes of patterns were designed on this mask: (1) ten 3 cm parallel traces with 10 μm width and 20 μm pitch, and (2) isolated single 3 cm traces with 10 μm width. The parallel traces each were joined by 10 μm wide traces at the two

36
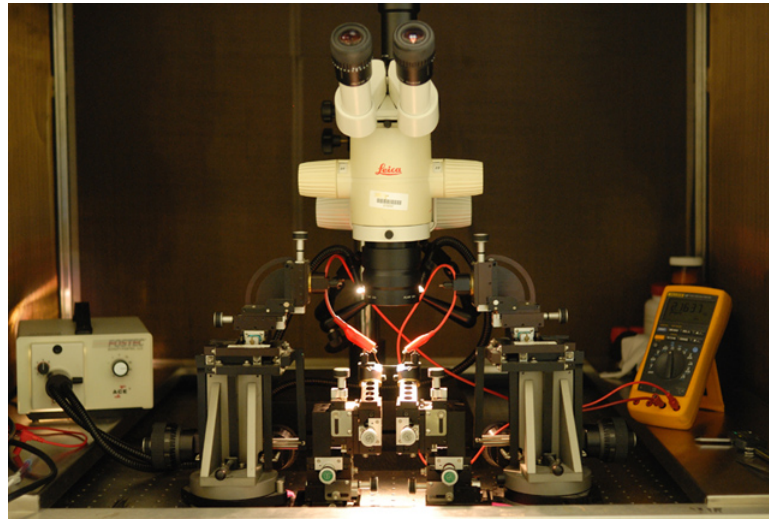
(a)
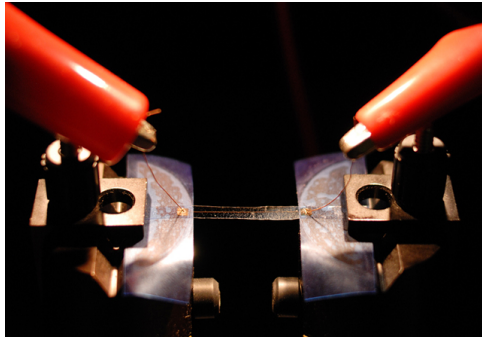
(b)
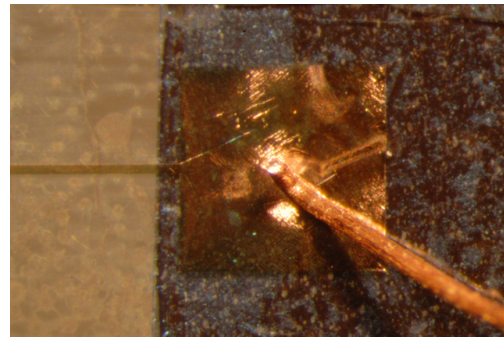
(c)

Figure 10: Setup for interconnect stretching experiment. (a) The stretching platform: micromanipulators (Siskiyou, Inc., OR) were used to mount and clamp the PDMS-based gold interconnects and contacting probes; the microscope was used to visually check the contact between probing wires and gold contact pads, as well as the status of the interconnect under investigation; the multimeter was used to record the resistances; and the interconnect was stretched longitudinally by one micromanipulator. (b) Close view of the mounting stage. Two pieces of blue tape (Semiconductor Equipment Corp., CA) were placed on the metal surface to enhance adhesion of the interconnect. An interconnect (20 nm thick, 100 μm wide, and 2cm long with a 4 mm^2 contact pad at each end) was mounted and clamped on the stage with two copper wires (200 μm in diameter) connected to the probes touching each contact pad. (c) Contact between one of the copper wires and a thin-film gold contact pad. The tip of the copper wire was bent to a hook shape to avoid damaging the contact pad.

terminals which then fanned out to contact pads. The fanning-out routes at either end had a length in the range of $0.5 \sim 1.25$ cm, which were taken into account during impedance normalization. For the single traces, one contact pad was directly attached to either end. Samples, with their glass slide attached for the ease of handling, were probed on the contact pads, while impedance spectra measured using a spectrum analyzer (SRS Dynamic Signal Analyzer, SR785).

3.3.4 Stretching Experiments

To test electrical properties of the patterned gold interconnects under longitudinal tensile strain, a chrome-plate mask was designed with a set of 2 cm wires of different widths (10 μm, 20 μm, 40 μm, 60 μm, and 100 μm). One 4 mm^2 square contact pad was attached to either terminal of every wire (see Figure 10c). Samples were fabricated with gold film thickness of 50 nm, 100 nm, 150 nm, 300 nm, and 500 nm (the Ti adhesion layer was of 1/10 gold thickness), respectively. First, interconnect resistances were measured with a multimeter before cutting out and detaching the interconnects from their glass slides (assuming 0% strain applied). Then, the detached interconnects were used in stretching experiment. Figure 10 shows the stretching experiment setup. Micromanipulators (Siskiyou, Inc., OR) were used to mount and stretch PDMS-based gold interconnects, while the resistances were monitored by a multimeter (Figure 10a). A microscope was used to visually check the contact between probing wires and gold contact pads, as well as the status of the interconnect under stretching. Two copper wires (200 μm in diameter) each connected to one multimeter probe touched on the two contact pads (Figures 10b and 10c) to form a closed circuit. The tip of each copper wire was bent to a hook shape to avoid damaging the contact pad (Figure 10c). The contact resistances together with the resistances of probe wires were measured for each gold film thickness by touching the two copper wires on the same contact pad, and subtracted from the interconnect resistances during data analysis. For each data point in Figures 13b, 13c, 14a and 14b, four individual samples each with a flat interconnect were tested.

(a)　(b)　(c)

(d)　(e)
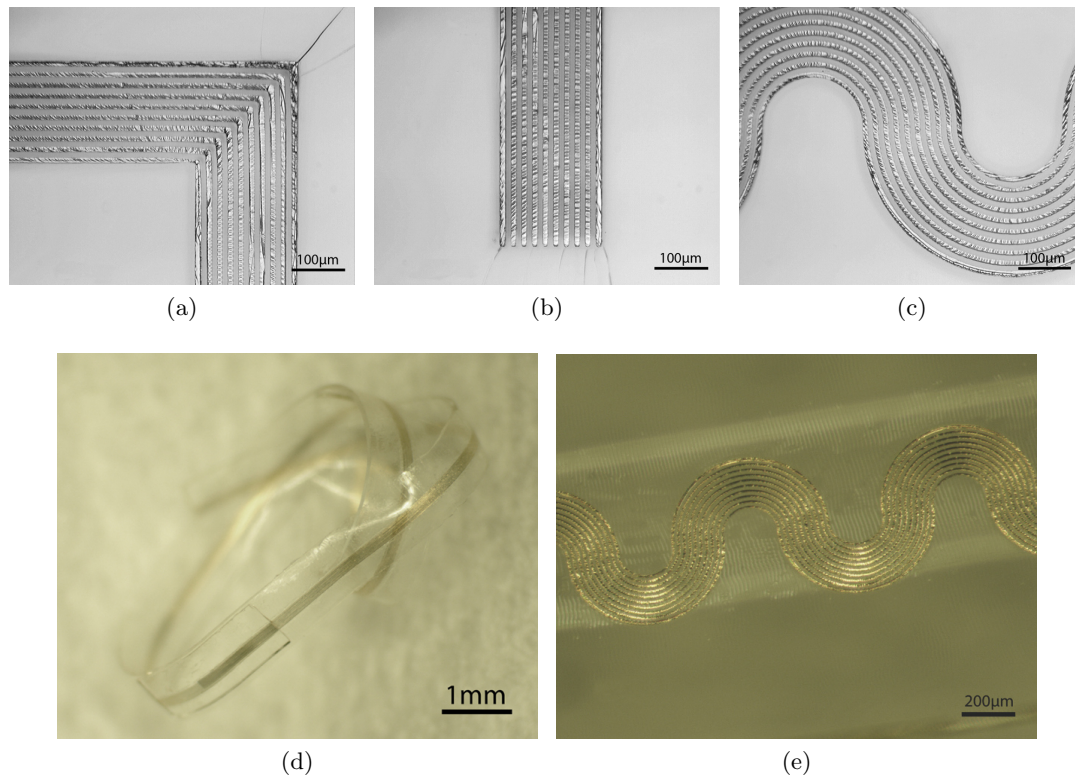
Figure 11: Lift-off results. The same sample as shown in Figures 9f – 9i was used to produce these results. 50 nm gold was deposited. Different testing patterns were designed on the same polyester film photomask to evaluate the fabrication resolution and density. The details of traces with the highest resolution and density (10 μm width and 20 μm pitch) are shown here. The complete set of results from a sample patterned using a chrome-plate mask is shown in Figure 12. (a), (b) and (c) Low-amplitude wrinkles displayed in the gold traces. Close inspections on (a) and (b) revealed that the traces at the corner and terminals, except the major one in (a), were imprints of PAA cracks on PDMS, not deposited gold residuals. (d) and (e) The 3cm and 2.4cm stripes each containing ten 10 μm wide traces with 20 μm pitch in parallel and serpentine arrangement respectively, were cut out with a razor blade and peeled off the glass. (d) The parallel stripe was curled using a pair of tweezers to get an overview of the whole stripe. (e) The serpentine stripe was slightly stretched (~2%).

3.4 Results

3.4.1 SU-8 Lift-Off Results

We used a polyester film photomask (vacuum contact mode) to fabricate the testing patterns in Figure 11, and a chrome-plate mask (hard contact mode) transferred from the polyester film mask to fabricate the patterns shown in Figure 12. The feature resolution on a polyester film is limited to 8 μm (manufacturer's specification, JD Photo-Tools, UK), and $2 \sim 3$ μm on a chrome-plate mask (Photo Sciences, Inc., CA). Although we demonstrated gold traces as long as 3 cm with 10 μm width and 20 μm pitch, higher resolution and density are possible when using a high-resolution chrome-plate photomask combined with electron beam lithography and an SU-8 lift-off mask thinner than 10 μm [98].

We fabricated numerous testing patterns with both parallel and serpentine traces. Figure 11 demonstrates the subsequently patterned gold traces from the same SU-8 lift-off mask shown in Figures 9f – 9i. The thickness of the gold deposition was 50 nm (primed by 5 nm Ti). Ten 3 cm parallel gold traces each with 10 μm width and 20 μm pitch were demonstrated (Figures 11a, 11b and 11d, see Figure 12a for the whole pattern as a reference). Ten serpentine traces spanning 2.4 cm each with 10 μm width and 20 μm pitch were demonstrated (Figures 11c and 11e). Such a serpentine design is shown to increase the stretchability of the interconnects [93, 43]. Traces are clearly defined and free of both electrical short and open circuits (Figures 11a – 11c, and 13a). Non-through cracks at right-angled corners (Figures 9g and 9h) left imprints on the PDMS substrate (Figures 11a and 11b). Closer inspections revealed minimal gold residuals on these imprints, with some exceptions (corner of Figure 11a).

3.4.2 Impedance and Resistance Measurements

To systematically evaluate electrical properties of the patterned interconnects, three sets of experiments were conducted: (1) impedance spectroscopy on high-density parallel traces (10 μm wide with 20 μm pitch) *vs.* isolated single traces to reveal any potential problems with the high-density parallel traces, (2) resistance measurements to reveal the relationships between trace resistance and geometries (width and thickness), and (3) uniaxial stretching

40

41
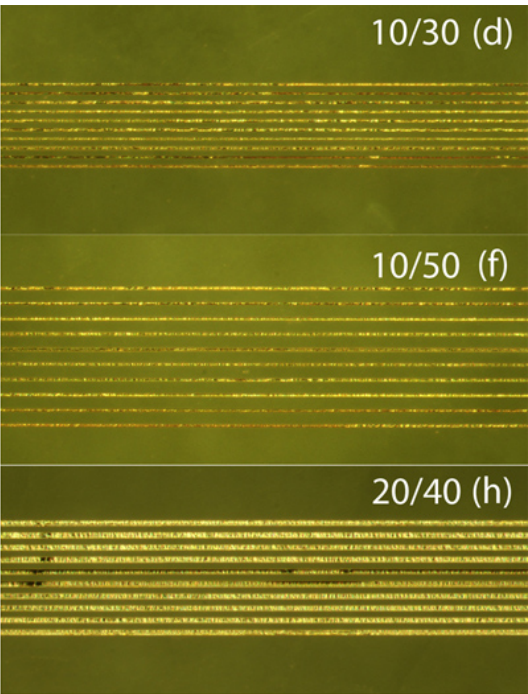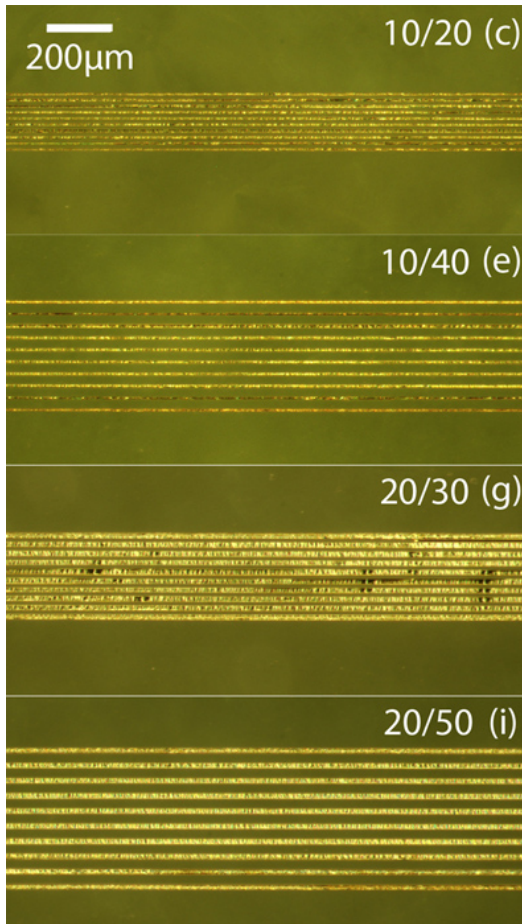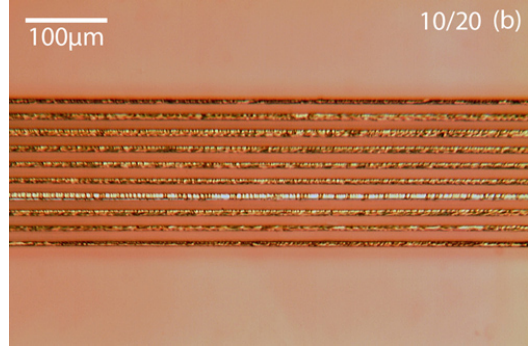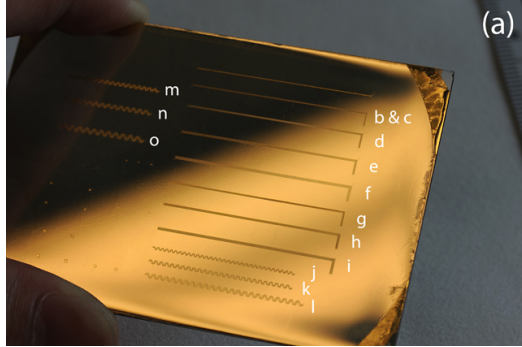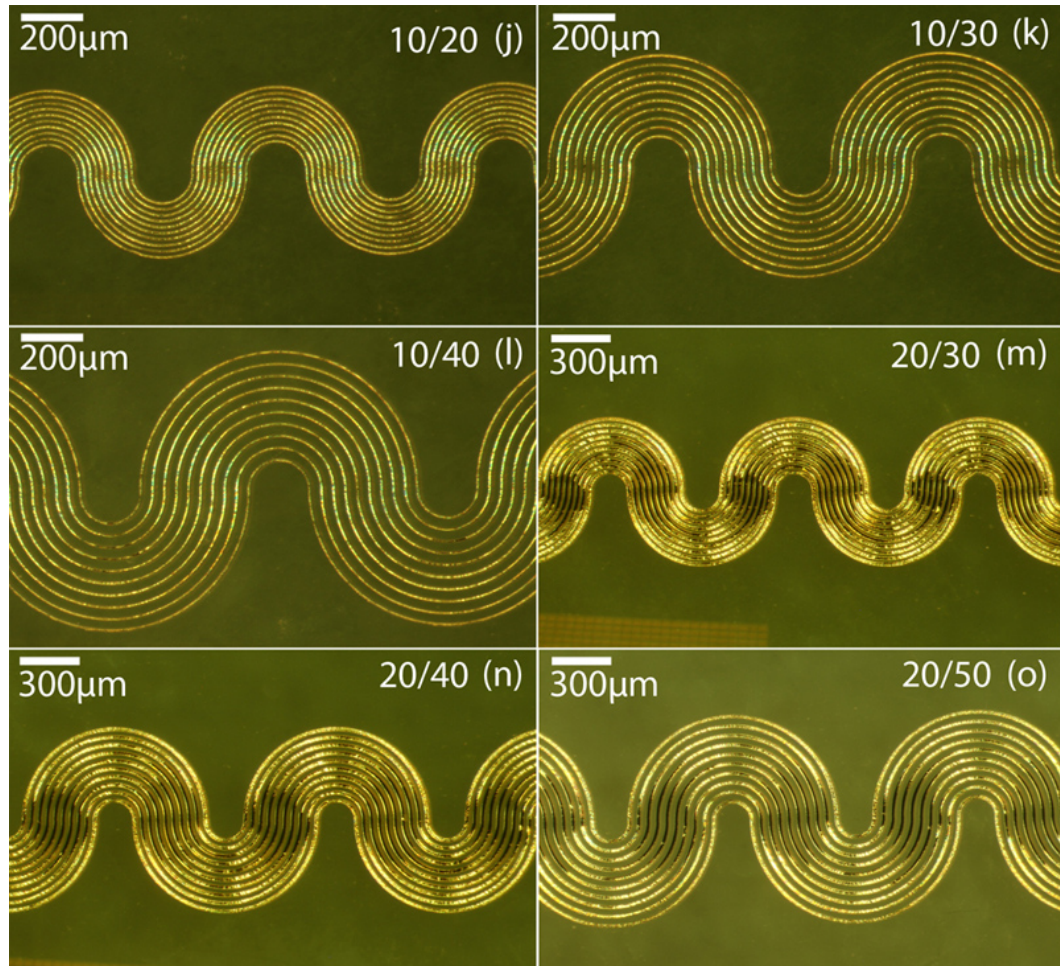
Figure 12: A complete set of lift-off results on different testing patterns. A chrome-plate photomask, transferred from the polyester film mask, was used with hard contact between the sample and mask during UV lithography. 15 nm Ti/150 nm gold were deposited in an electron beam evaporator. In each microscopic image, the numerator indicates the designed trace width on the mask, while the denominator the pitch on the mask. The images were taken with the PDMS film attached on its glass substrate. (a) The stripes each are labelled corresponding to their microscopic images. (b) Instead of 10 μm wide, the gold traces measure $\sim$8 μm in the majority parts. Slight distortions in the SU-8 lift-off mask caused inconsistency of the trace width at some points. (c) though (i) share the same scale bar.
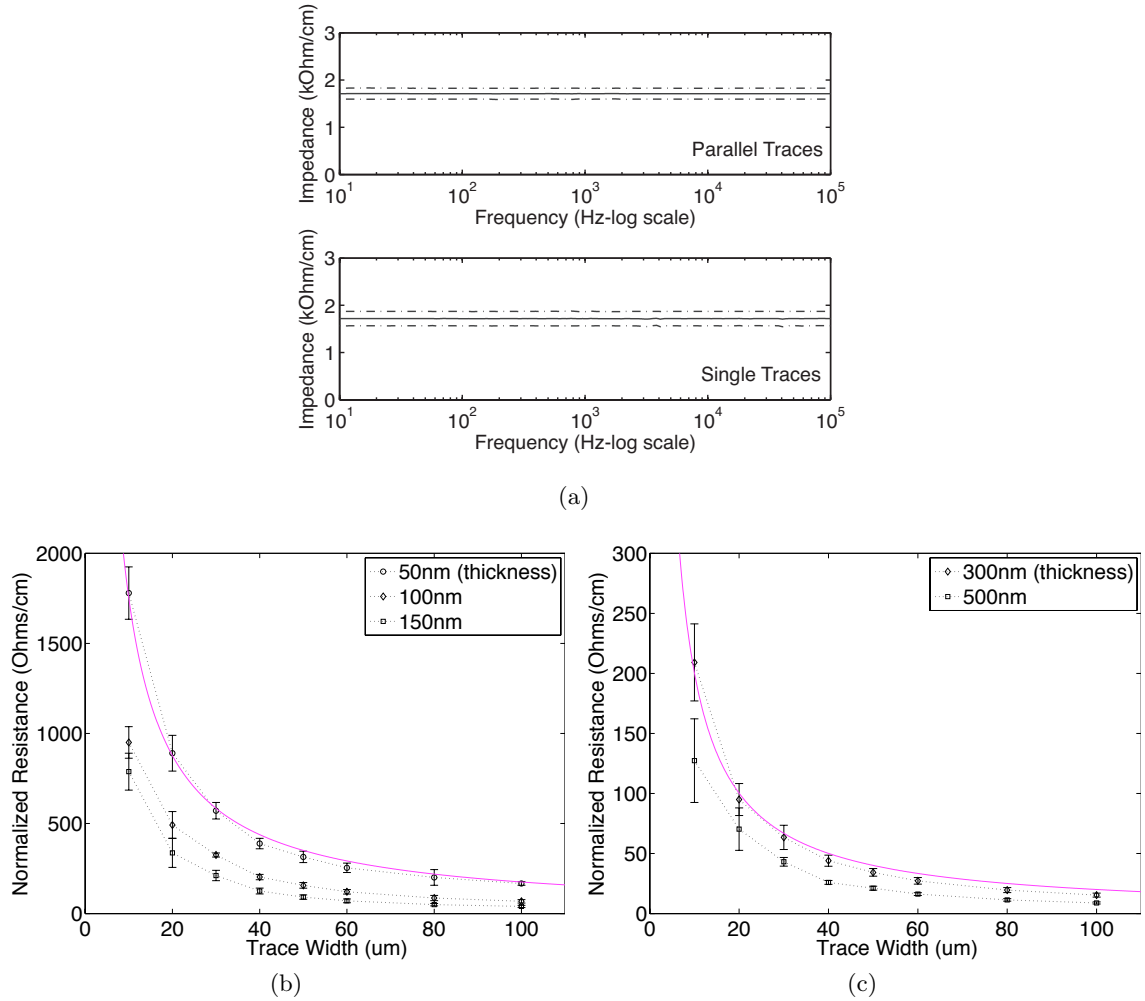
Figure 13: Electrical properties of patterned interconnects. (a) Normalized average impedance spectra (solid line) of ten 50 nm thick, 10 μm wide parallel traces with 20 μm pitch (top plot) and ten 50 nm thick, 10 μm wide isolated single traces (bottom plot). One standard deviations from the average were shown as the dash-dotted lines. (b) and (c) Normalized resistances of traces with different widths and thicknesses (0% strain). The first group of data in each figure [50 nm thickness in (a) and 300 nm thickness in (b)] was fitted to a $y = ax^{-1}$ curve (magenta) as a demonstration of the inverse proportion relationship.

experiments to characterize the evolution of electrical resistance under tensile strain.

Figure 13a shows the normalized average impedance spectra with boundaries of one standard deviation for the ten parallel traces and ten single traces. The two spectra overlaps with each other when plotted in the same plot. This overlap verified that there existed no multiple-site (≥ 2) short circuits or cross-talk between the adjacent parallel traces. Further impedance measurements between any two adjacent traces each resulted in an open circuit, thus eliminating the possibility of single-site short circuits. Therefore, the high-density parallel traces are electrically equivalent to the isolated single traces with the

43

same dimensions.

Since the impedance spectroscopy experiment revealed statistically constant impedance of the interconnect across the frequency spectrum (Figure 13a), simple resistance measurement was employed in further experiments. Figures 13b and 13c show the dependences of trace resistance on trace width and thickness when no strain was applied. As expected, for data points along each dotted curve, i.e. the gold film thickness is fixed, the trace resistance is inversely proportional to the trace width. The same relationship applies to the trace resistance and thickness when the trace width is fixed (plots not shown).

3.4.3 Stretching Experiments

Figure 14a shows the resistance variations under longitudinal strains for 2 cm long, 100 μm wide, flat straight traces with difference thicknesses. Flat straight traces with a thickness no smaller than 100 nm failed at a longitudinal tensile strain slightly greater than 1%, while those with a thickness of 50 nm could withstand a tensile strain up to 2%. These results agree with the properties of free-standing thin metal films [130] and are consistent with our previous study on gold interconnects patterned with a wet-etching method [93], but this stretchability is considerably low compared to results of flat straight traces reported by other groups [70, 130]. This discrepancy may be a result of different micro/nano-scale morphologies of the gold films deposited with different equipment under different conditions [42]. For example, we deposited the gold film in an e-beam evaporator at 1 Å/s, which was found to result in a denser film than higher rates and to promote gold adhesion to PDMS [52], while 2 Å/s was used in Refs. [70] and [130]. Many other factors, including the thickness of the PDMS substrate (70 μm was used in our experiments), may also play a role. Another possibility lies in the limitation of our geometry design of the testing interconnects (Figure 10c). It is possible that the junction between the trace and the contact pad is the site where excess strains would generate and where the interconnect would break first under a stain loading. This would consequently obscure our experimental quantification of the real interconnect stretchability.

Figure 14b shows the resistance variations under longitudinal strains for 2 cm long,
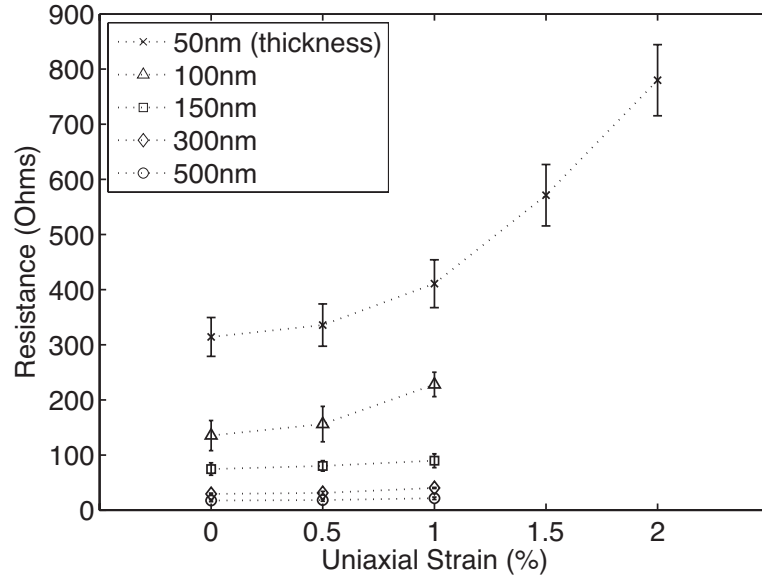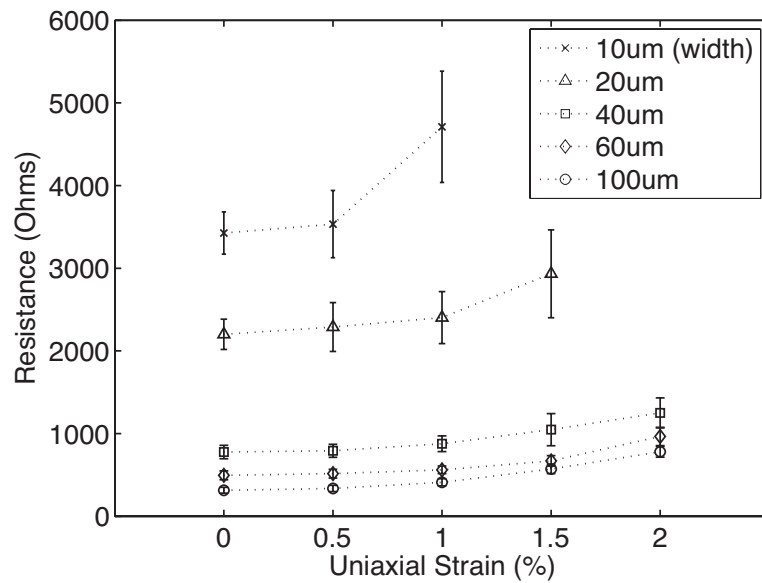
Figure 14: Interconnect resistance during stretching. (a) Resistance variations under uniaxial (longitudinal) strain for 2 cm long, 100 μm wide, flat straight traces with difference thicknesses. (b) Resistance variations under uniaxial (longitudinal) strain for 2 cm long, 50 nm thick, flat straight traces with different widths.

45

50 nm thick, flat straight traces with different widths. Traces with width of 40 μm and above could withstand a tensile strain up to 2%, while narrower traces broke at a slightly lower strain (1% strain for 10 μm wide traces, and 1.5% for 20 μm traces, respectively). This was probably because the microcracks that were induced by the tensile strain and responsible for the electrical failure [69] were easier to develop across the full width of narrower traces.

For all samples tested, when relaxed below the failure strain, the traces re-conducted, albeit that the resistance became slightly higher than before at same strain. This recovery phenomenon is consistent with previous observations [70, 130, 93, 89, 43, 69].

3.5 Summary

In summary, this chapter described an effective lift-off method for patterning high-resolution, high-density, thin-film gold interconnects on a PDMS substrate. Both parallel and serpentine gold traces with 10 μm width and 20 μm pitch were fabricated, successfully demonstrating density increases of more than one order of magnitude from previously established work. Higher resolution and density are likely possible with the use of high-resolution chrome-plate photomasks combined with electron beam lithography. Electrical test verified that the high-density interconnects were electrically equivalent to isolated single interconnects with the same dimensions and that the inversely proportional relationship between trace resistance and width/thickness was conserved. Uniaxial stretching experiments revealed that the patterned flat thin-film gold interconnects could withstand longitudinal tensile strains in the range of $1 \sim 2\%$. To further boost the stretchability, structures that facilitate large mechanical deformations [110] can potentially be incorporated into the interconnect design to create, e.g., serpentine traces [93, 43] (as already demonstrated), wavy traces [70, 130], or ion-implanted traces [111].

46

CHAPTER IV

IMPLEMENTATION OF MULTILAYER ARCHITECTURE AND INTEGRATED PACKAGING

In this chapter, I continue with the discussion in Chapter III on our high-density inter-connect technology, with focuses on addressing the other two major challenges associated with PDMS-based fabrication, namely achieving multilayer interconnects within the elas-tomeric substrate, and packaging the soft electronics with standard rigid electronics. These advanced fabrication techniques are compatible with and easy to be integrated into the fabrication flows described in Chapters II and III.

Taken together, the technological advances described in Chapters II, III and IV facilitate an integrated technology platform for PDMS-based sMEAs. By combining and tailoring these technical elements, customized sMEA designs can be produced for numerous neural interfacing applications. The next chapter will summarize and exemplify this *PDMS-based sMEA technology platform*.

The work presented in this chapter has been published primarily in Ref. [50].

4.1   Introduction

When only a single layer of interconnects is used, the integration density of electronics is limited. To address this limitation of PDMS-based electronics, numerous efforts have been made toward multilayer implementations [120, 6], however, a truly multilayer technology that is reliable and that has high-resolution and high-densitiy capability does not yet exist. As a result, sMEAs in practical use are implemented with only a single conducting layer. The difficulty in achieving multilayer implementations on compliant substrates has significantly limited the integration capacity and density of such sMEAs due to the difficulty in wiring a large number of microelectrode channels. In this chapter, I describe our approach to fabricating multilayer interconnects within the PDMS substrate through the combination of a lift-off method and an inclined-via technique.

Packaging of electronics is a critical aspect that can significantly affect the performance. While always neglected during the initial development of most MEAs, this packaging problem must be addressed with a good solution before the device can be widely adopted in practice. Without an associated robust packaging technology, the practical utility of PDMS-based sMEAs is dramatically diminished.

The PDMS material cannot be soldered on, neither can the thin metal film on the contact pads withstand the high soldering temperature. The traditionally used methods for connecting the PDMS-based devices to external circuitry are (1) clamping on contact pads [71, 93], (2) gluing wires on contact pads using conductive epoxy/polymer, and (3) welding wires or riveting on contact pads [116] (metal foil was used in this case, so this method is not applicable for devices with deposited thin metal film). The first two methods are not satisfying, because (1) the resulting electrical connections are unreliable and unsustainable; (2) the bonding process is labor intensive; and (3) the contact pads require large size, thus expanding the device size significantly.

To address this packaging issue, in this chapter, I also describe a *via-bonding* technology, which is a derivation of the multilayer interconnect technology, to facilitate high-resolution, high-density integrated packaging of PDMS-based electronics.

4.2   Approaches

The key to our multilayer interconnect technology is the combination of a lift-off method, which requires an anisotropic metal-deposition process, with an innovative inclined-via technique. Figure 15 illustrates the method for fabricating multilayer interconnects within PDMS or between PDMS and another substrate. Lift-off methods—because of their cleanness and process compatibility—are conventionally used in the patterning of thin-film metal features on PDMS substrates (see Chapter III). In order to implement multilayer interconnects both within PDMS and between PDMS and another substrate, we have created a process for fabricating vias with inclined sidewalls through the PDMS. The inclined sidewalls are essential to provide electrical connections between the conductors on different
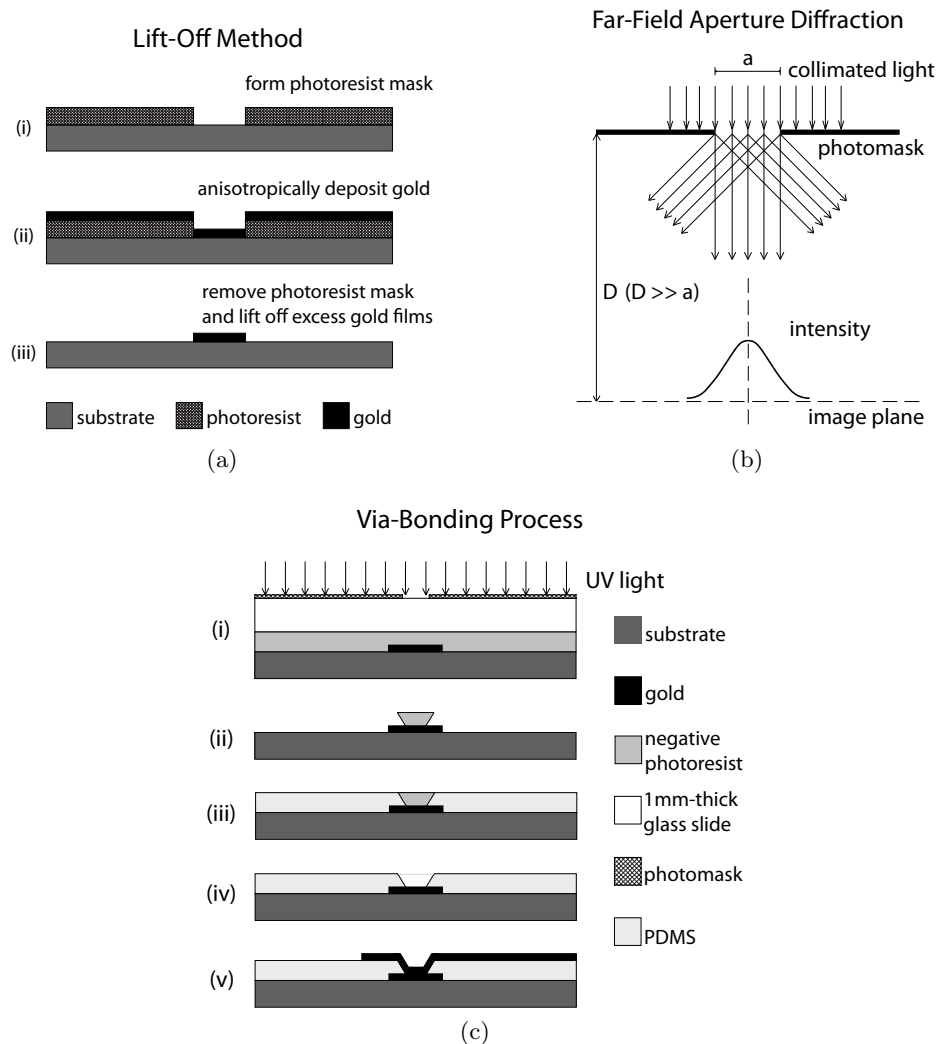
Figure 15: Method for fabricating multilayer interconnects within PDMS or between PDMS and another substrate. (a) Lift-off method for patterning thin-film metal features. When the lift-off process is done in solvent or solution, the photoresist mask starts to dissolve or peel off from the feature sidewalls where no metal exists, and subsequently excess metal films are lifted off. (b) Far-field aperture diffraction phenomenon. When collimated light passes through a micro-hole, the light beam diffracts at the edges and casts a bell-shaped intensity profile on an image plane placed with a distance D (large compared to the diameter a of the hole) away from the photomask. The via-bonding process makes use of this phenomenon to create tapered sacrificial posts. (c) Fabrication process steps. (i) A thick negative photoresist layer on a sample is placed at the image plane 1 mm away from the photomask. (ii) The resulting exposure creates a tapered sacrificial post. (iii) The post is subsequently used to mold the PDMS insulation. (iv) Removal of the sacrificial post results in an inclined via in the PDMS. (v) When patterning the second conducting layer using the lift-off method illustrated in (a), the two conducting layers are electrically interconnected by the metal film deposited on the recessed slope of the inclined via.

49

layers. Because we use a lift-off method (Figure 15a), we must use anisotropic metal deposition to create the gold conductors on the PDMS. Vias with vertical sidewalls would fail to make electrical connections between conducting layers because the anisotropic deposition would not result in metal on the sidewalls. The thin gold film deposited on the recessed slope of inclined vias, however, functions to electrically bridge the two conducting layers.

To fabricate the inclined vias, we use projection exposure in photolithography, which involves far-field aperture diffraction [30] (Figure 15b). In this method, collimated light passing through a micro-hole (100 μm diameter) diffracts and casts a bell-shaped intensity profile on an image plane placed at a distance (>1 mm) away from the photomask. When a thick negative photoresist layer is placed at this image plane, the exposure results in a tapered post. A similar approach has been used previously in backside exposure of thick negative photoresist to create tapered SU-8 pillars [65]. We use this configuration to modulate the UV light intensity distribution in the exposure process of thick negative photoresist to make sacrificial posts with a tapered shape. This is the same technique as was used in Chapter II to create the conically recessed microelectrode. In Figure 15c(i), when the thick negative photoresist layer is positioned at the image plane in (Figure 15b), the exposure results in such a tapered profile [Figure 15c(ii)].

The tapered sacrificial post is used as a mold during the formation of the encapsulation PDMS layer [Figure 15c(iii)], resulting in a complementary inclined via in the PDMS after the post is sacrificed [Figure 15c(iv)]. Well-defined spinning and curing recipes ensure that the PDMS prepolymer disperses to a layer thickness smaller than the height of sacrificial posts and that the prepolymer clears off the top of sacrificial posts [28]. The second conducting layer is fabricated using the same lift-off method (Figure 15a) as used for the first conducting layer; the two layers are electrically interconnected where an inclined via exists as result of the gold film deposited on the recessed slope of the inclined via [Figure 15c(v)].

By iterating the steps in Figure 15c, additional interconnected conducting layers can be fabricated subsequently. The "substrate" denoted in Figure 15c can be either PDMS or other rigid materials, such as silicon, glass, printed circuit board (PCB), etc. For a PDMS substrate, the multilayer interconnects are made within the PDMS. For rigid materials,

50

via bonds are fabricated on the rigid substrate and subsequent multilayer interconnects are fabricated using PDMS layers to facilitate increased integration density.

4.3   Methods

4.3.1   Lift-off Method

While the two lift-off methods mentioned in Chapters II and III both can be used, the fabrication results in this chapter were done with the old SPR 220 lift-off method, because the SU-8 method was developed at a later time. But the SU-8 lift-off method has an additional advantage when combined in the via-bonding process, i.e., as a negative photoresist (unexposed area will be developed away), no extra effort is needed to remove the thicker photoresist accumulated in the inclined via for opening a connecting pad on the via in the lift-off mask (Figure 17c), whereas in the SPR 220 lift-off method, an extra UV exposure dose or step is needed to photo-decompose the thicker photoresist in the inclined via, which will enlarge the patterned gold feature dimensions.

The sample is first briefly treated in oxygen plasma to activate the substrate [either cured PDMS (Sylgard 184, Dow Corning) or a rigid material] surface. Immediately following this treatment, positive photoresist [Megaposit SPR 220 (0.7 - 7.0), Shipley] is spin-coated at 1500 rpm for 30 s with a ramp rate of 300 rpm/s. The sample is baked on a hotplate at 90 ℃ for 10 minutes. The resulting photoresist layer is approximately 12 μm thick. The sample is then patterned by photolithography with a UV exposure dose of 700 mJ/cm^2 at 365 nm i-Line, developed in developer (Microposit MF-319, Shipley) for about 160 s, rinsed with DI water, and blown dry gently. Finally, the resulting photoresist mask is flood-exposed with the same dose to enable the subsequent lift-off in its developer [Figure 17a(i)]. A hold time of at least 120 minutes is required before starting depositing gold to allow water, which is necessary to complete the photo-reaction, to diffuse back into the photoresist mask. The sample is then placed in an electron beam evaporator for a priming layer of 20 $\sim$ 300 Å Ti deposited at 1 Å/s. This step is followed by a 200 $\sim$ 5000 Å gold film deposition at 1 Å/s [Figure 15a(ii)]. After deposition, the sample is soaked in the corresponding photoresist developer (Microposit MF-319, Shipley) to dissolve the photoresist mask and lift off excess

gold films, leaving only the desired gold features [Figure 15a(iii) or 15c(v)]. The gold patterned sample is then rinsed and dried.

4.3.2 Via-Bonding Process

Following brief treatment of the sample in oxygen plasma, a thick layer of negative photoresist (NR5-8000, Futurrex) is formed on the sample. The thickness of the layer depends on the lowest aspect ratio of the inclined via (defined as the via base diameter *vs.* the via depth) to be made. The sample is then patterned to leave a tapered sacrificial post right on top of each gold feature where an inclined via is to be made [Figures 15c(i) and c(ii)]. Next, following oxygen plasma treatment of the sample, a PDMS (Sylgard 184, Dow Corning) insulation layer is spin-coated to encapsulate the device at 5000 rpm for 150 s with a ramp rate of 1000 rpm/s. Sequentially, the uncured sample is left at room temperature for one hour, baked on a 60 ℃ hotplate for one hour, and then baked in a 90 ℃ oven for two hours. The resulting encapsulation thickness is approximately 10 μm, except for the areas closely surrounding the sacrificial posts [Figure 15c(iii)]. To effectively remove the sacrificial posts, a brief RIE descum process is first applied to remove any potential thin PDMS residues on top of sacrificial posts [37]. The sample is then immersed in acetone for approximately 10 minutes to remove the scrificial posts [Figure 15c(iv)]. Finally, a lift-off process is used to pattern a new conducting layer to complete the via bonding [Figure 15c(v)]. Two key points for creating the inclined via are worthy of emphasizing: (1) A 1 mm glass slide is placed between the photomask and NR5-8000 layer [Figure 15c(i)], and approximately 2/3 of standard exposure dose (i.e. 14 mJ/cm^2 for 1 μm thick film) is used during UV exposure to create sacrificial posts with tapered sidewalls. Increasing or decreasing the exposure dose by 5/3 mJ/cm^2 for 1 μm thick film each step within a certain range may result in tapered sacrificial posts with different sidewall slopes (Table 1 and Figure 17a). (2) The PDMS insulation layer is spin-coated immediately after oxygen plasma treatment of the sample. The recess depth of a via is determined by the height of the sacrificial post, and this height needs to be made slightly higher than the desired thickness of the PDMS insulation layer.

52

| (a) | (b) |
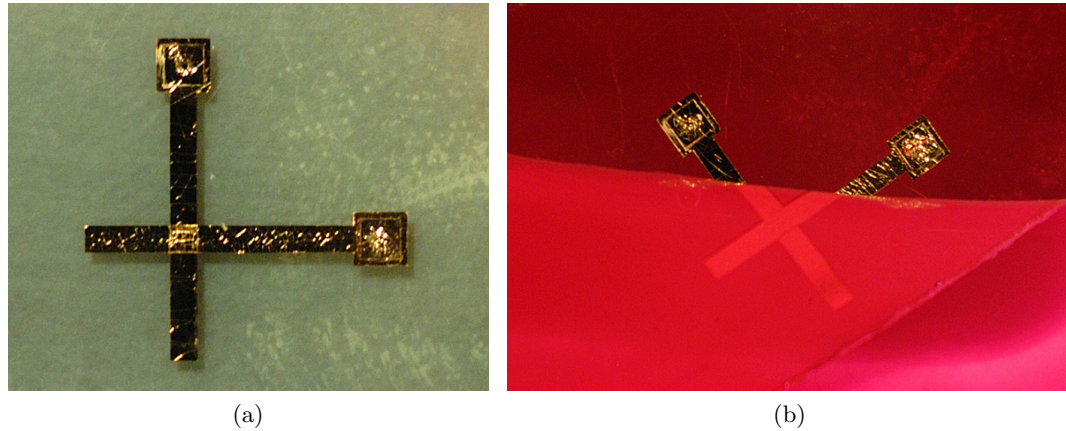
Figure 16: Interlayer capacitance measurement. (a) The device was tested in the air. (b) The device was immersed in HBSS and tested.

4.3.3   Interlayer Capacitance Measurement

Figure 16 shows the two-layer device investigated. Each interconnect measures 1 mm wide and 1 cm long with a 4 mm^2 square contact pad at one end. The overlapped area of the two interconnects is 1 mm^2. The resistance and capacitance from four samples were measured with a multimeter in the air (Figure 16a) and in Hanks Balanced Salt Solution (HBSS 1X, Gibco, Figure 16b) [(in mM): KCl 5.33, KH_2PO_4 0.441, $NaCl$ 137.93, $NaHCO_3$ 4.17, Na_2HPO_4, D-glucose 5.56, Phenol Red 0.0266]. The saline solution is to mimic the biological environment in which the sMEAs will be used. The thickness of the insulation PDMS was measured on the contact pad edges from four samples using a profilometer (KLA-Tencor P15 Profilometer, see Chapter II for settings).

4.4   Results

4.4.1   Implementation of Multilayer Interconnects

4.4.1.1   Proof of Concept

We fabricated the inclined vias as shown in Figure 17. We demonstrated that the sidewall slope of the sacrificial posts could be controlled by adjusting UV light exposure dose (Figure 17a), as a result of the low contrast profile of the light intensity on the image plane (Figure 15b). The achievable resolution of the resulting devices is 10 μm width for gold lines and 10 μm base diameter for inclined vias (given a 10 μm thick PDMS encapsulation layer).

53
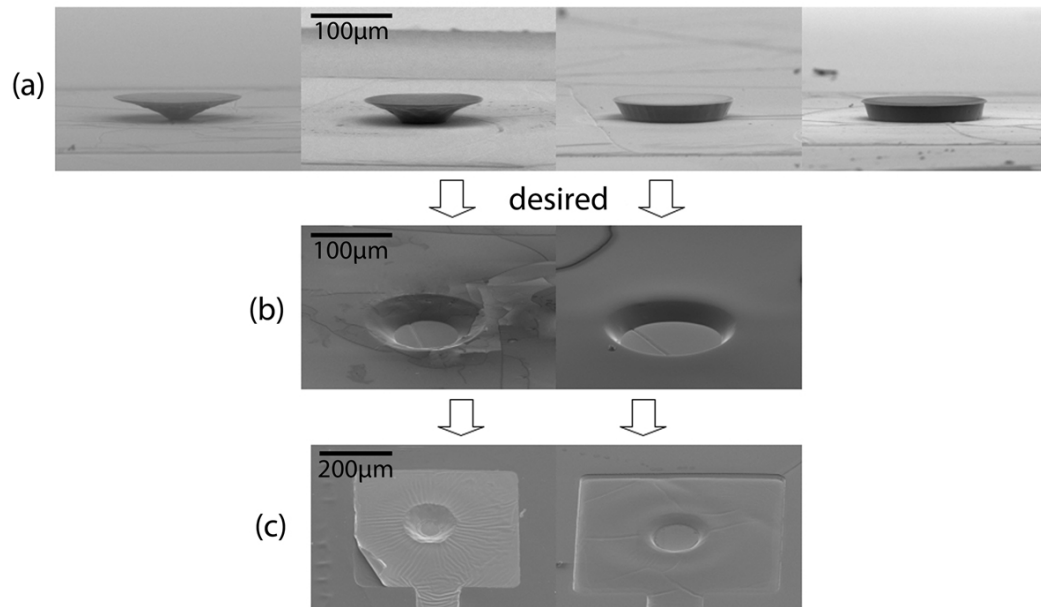
Figure 17: Fabrication results demonstrating the achievement of a multilayer interconnect by an inclined via. (a) Tapered sacrificial posts with different sidewall slopes were produced by using different UV light exposure doses. From left to right, the dose was increased. (b) Inclined vias with desired profiles were created in the PDMS insulation layer using the molding process. (c) The second gold layer was patterned using the lift-off process, and an interlayer interconnection (i.e. a *via bond*) was formed at the inclined via. After lift-off, a corner of the square gold film was lifted up intentionally to give a better visualization of the thin gold film (image on left). After gold deposition but before lift-off, the sidewalls of the photoresist mask can be seen clearly (image on right).
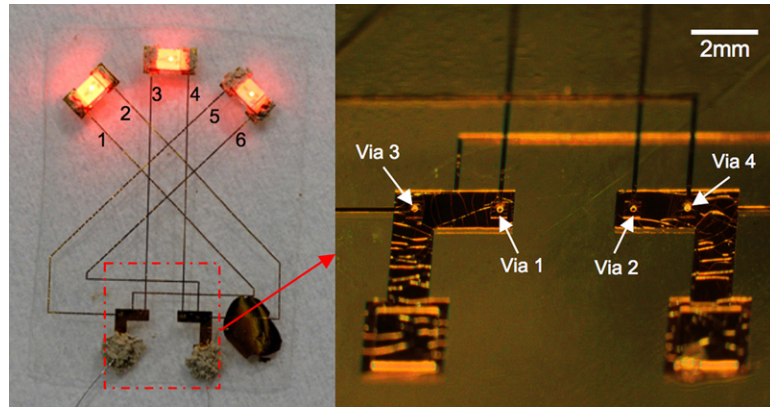
(a)
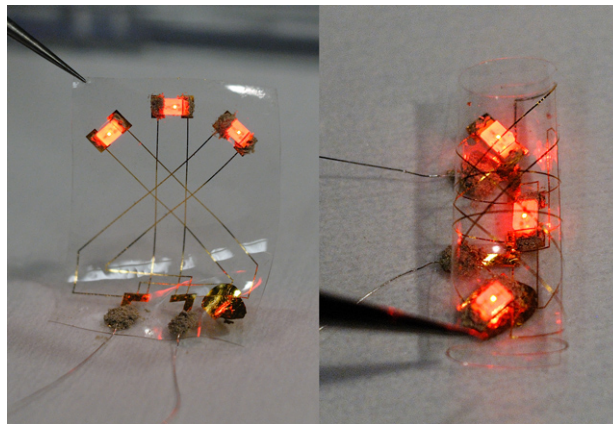
(b)

Figure 18: Demonstration of multilayer interconnects within PDMS. (a) A prototype device with three interconnected conducting layers. The total thickness of this device is 100 μm, which includes a 70 μm PDMS base layer and three 10 μm PDMS insulation layers. The thin gold lines on different conducting layers are all 100 μm wide. Three LEDs were glued using conductive polymer (Silicone Solutions; Twinsburg, OH) to their exposed contact pads on separate conducting layers. Power was supplied to the device through two silver wires glued to the contact pads on the bottom conducting layer. Traces 1 and 2 and power lines are on the bottom conducting layer; Traces 3 and 4 are on the middle conducting layer, and interconnected to the power lines through Vias 1 and 2, respectively; Traces 5 and 6 are on the top conducting layer, and interconnected to the power lines through Vias 3 and 4, respectively. Vias 3 and 4, both formed by two stacked inclined vias during two cycles of processes, go through two PDMS insulation layers, and thus are deeper than Vias 1 and 2. (b) Deformation of the device in (a). The device was scrolled into a roll while still maintaining its electrical functionality (right).

55

The aspect ratio of the inclined via (defined as the via base diameter *vs.* the via depth) must be between 5 : 1 and 1 : 5 to ensure successful fabrication and electrical performance.

4.4.1.2 Demo Device

As shown in Figures 18a and 18b, we fabricated devices that include interconnections between three layers of wiring within the PDMS. Gold traces embedded in the PDMS were interconnected to each other. The total thickness of the device in Figures 18a and 18b is 100 μm, which includes a 70 μm PDMS base layer and three 10 μm PDMS insulation layers. The thin gold lines on different conducting layers are all 100 μm wide. To verify the viability of the wiring and of the multilayer interconnect, we implemented circuits to power three LEDs, one connected to each wiring layer, and demonstrated the device's ability to illuminate each LED and to withstand large deformation while maintaining its electrical functionality.

4.4.1.3 Interlayer Capacitance

While the electrical properties of single-layer gold interconnects have been characterized in Chapter III, it is also interesting to know those of the multilayer interconnects. So, we performed a resistance and capacitance testing experiment (Figure 16) to determine the potential cross-talk between two conducting layers.

The PDMS insulation layer thickness measured using a profilometer is 7.35 ± 0.45 μm. Profilometer measurement on PDMS samples is considered ~40% less than the real value [140], so the corrected thickness is 12.25 ± 0.75 μm. The measured interlayer capacitance in the air is 95.5 ± 0.6 pF/mm^2. This is 48 times the calculated value for a capacitor with the

Table 4: Interlayer electrical properties

In the Air		In Solution (immediately)		In Solution (after 3 hours)		Taken Out of Solution (immediately)	
Cap.	Res.	Cap.	Res.	Cap.	Res.	Cap.	Res.
95 pF	open circuit	111 pF	open circuit	108 pF	open circuit	95 pF	open circuit

same materials and dimensions. This discrepancy is caused primarily by surface roughness of the gold interconnects, as can been seen from Figure 16a.

As shown in Table 4, when the sample was immersed in HBSS (Figure 16b), the capacitance increased slightly. This is because the solution helped to couple more interconnect areas. The slight drop in capacitance after 3 hours was a consequence of HBSS evaporation, which reduced the solution-coupled interconnect area. When the device was taken out of the solution after 3 hours, the capacitance measurement showed the same value as before the immersion. Measurements in both air and HBSS showed gold electrical insulation between the two interconnects.

4.4.2 Multilayer Via-Bonding Technology

Initially, we had used two methods for connecting the sMEA to external circuits. Figure 19a shows a clamping method. However, the thin gold film on the contact pads could easily be rubbed off by rigid contacts on the clamp (inset), limiting the re-usability of the sMEA. Moreover, the electrical connections were not reliable at the contact pads. In Figure 19b, thin wires were glued to the contact pads using conductive epoxy (Loctite 3880), followed by PDMS encapsulation (inset). The bonding process was labor intensive, and when the number of electrode channels becomes large, it is simply impossible to wire the sMEA manually. Furthermore, the electrical connections were not reliable, either, because the conductive epoxy was cured at 90 ℃ rather than at the recommended 125 ℃ to prevent the thin-film gold conductors from cracking and the connections could be lost at the joints when the wires were subject to strain.

In spite of the attractiveness of PDMS-based sMEAs, the lack of a good packaging solution for the sMEA had limited its applications to a small number of electrode channels with unreliable electrical connections to external circuits.

Excitingly, by applying the inclined-via technique between PDMS and a rigid substrate (Figure 15c), we have successfully demonstrated the formation of reliable electrical connections on the rigid substrate. As shown in Figure 17c, we fabricated an sMEA that included interconnections between the electrode wiring layer and a rigid glass substrate. Gold traces

57

(a)

(b)

(c)
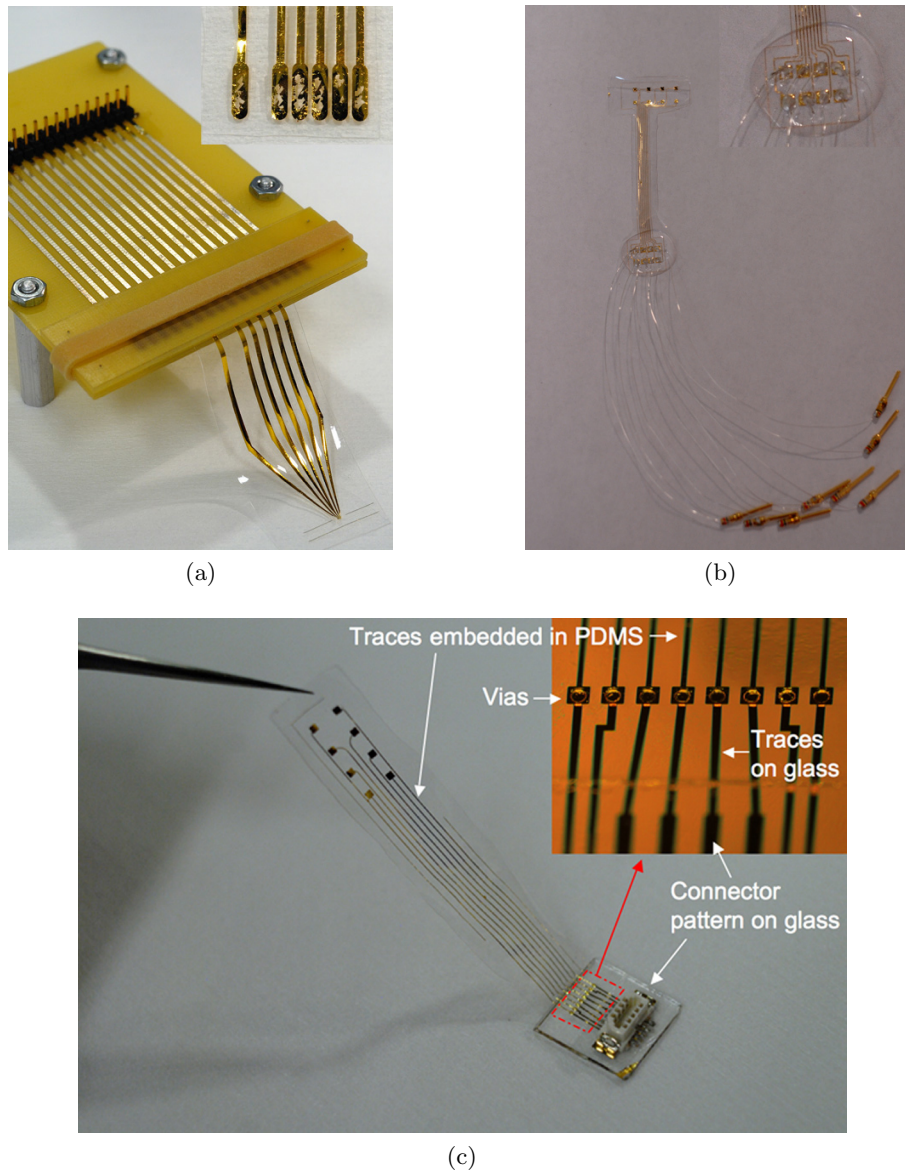
Figure 19: Different packaging solutions for PDMS-based sMEAs. (a) A clamping method. (b) Thin wires were glued to the contact pads using conductive epoxy/polymer, followed by PDMS encapsulation. (c) Integrated packaging solution using our via-bonding technology. Gold traces embedded in PDMS are interconnected to gold traces on glass through inclined vias. An anti-adhesion gold layer had been coated on the glass substrate to facilitate peeling off the sMEA body. But, no anti-adhesion gold had been coated in the area surrounding the vias, so that PDMS could adhere to the bare glass substrate strongly. A connector was glued onto the connector pattern using conductive epoxy. Excess glass substrate was cut off. Inset, via-bonds on a rigid substrate (glass). In this bonding area, PDMS was cured on bare glass. This formed a strong bonding between PDMS and the glass substrate.

embedded in the PDMS were interconnected to gold traces on the glass through inclined vias. Because PDMS cured on glass, silicon, or PCB bonds strongly to that substrate, the inclined-via–based interconnects (i.e. *via-bonds*) between PDMS and the rigid substrate can form reliable multilayer electrical connections on the rigid substrate. The achievable resolution of the via-bond is 10 μm given a 10 μm PDMS encapsulation layer, which is a very high resolution for a bonding technology when compared to the industry standard wire-bonding and flip-chip technologies. Moreover, the *multilayer via-bonding technology* is a parallel process in which all the via-bonds on one wiring layer are implemented in a single cycle of processes, while repetition of this cycle of processes can produce multiple interconnected wiring layers subsequently to facilitate increased integration density through area-array bonding pads and 3-D wiring.

This multilayer via-bonding technology offers us an integrated packaging solution that makes the sMEA easy to be connected to supporting circuits. This is a fascinating advance for sMEA applications that require high channel-count devices with a compact form factor and enhanced electrical performances. Many different materials will be eligible for the connecting substrate, provided that: (a) the material is compatible with the sMEA fabrication process; (b) PDMS adheres to it strongly enough; and (c) it provides better properties for connecting to external circuits. PCB, silicon, glass, and polyimide, for example, are candidates among this category. In Chapter V, I will give example sMEA designs that are packaged with glass, PCB, and silicon substrates, respectively.

4.5 Extended Applications

While application of the multilayer interconnect and via-bonding technology to high-density PDMS-based sMEA fabrication will be given in detail in the next chapter, here I describe some example applications of the technology to (stretchable) electronics in general.

The performance of a whole circuit system not only depends on the performances of its components and subcircuits, but also depends on how these components and subcircuits are interconnected and packaged to achieve the system functionalities. Therefore, one approach is to implement the whole circuit on a single chip, i.e. system on chip (SoC). But this

approach requires custom IC design and fabrication for each system, which often requires high-level expertise and is expensive, thus sacrificing the flexibility and generality for the adoption of modular subcircuits for various board-level designs. Alternatively, extensive efforts have been made to enhance the performances of interconnection and packaging to meet the ever stringent packaging requirements created by the dramatic advances in ICs.

In today's IC technology, I/O number of a single chip can easily go beyond hundreds, and the system clock frequency is usually in the range of MHz to GHz. Systems with increasing performance require low delay and low power consumption on the interconnections, and these requirements have pushed the traditional circuit form of mounting individually packaged chips on a PCB beyond its performance limit. Consequently, the trends of advanced packaging start to improve and even bypass the packaging of individual chips and go with chip scale packaging (CSP) or direct chip attach (DCA) to form more compact systems, such as chip on board (COB) [76], chip on glass (COG) [61, 136, 139], chip on flex (COF) [32, 18, 136, 138], wafer level chip scale packaging (WL-CSP) [38], etc. The architectures of such 2-D multichip modules (MCMs) allow significant reduction in circuit area and increase in performance by mounting and interconnecting bare dies directly on a wiring substrate using wire bonding, flip-chip bonding, tape automated bonding (TAB), anisotropic conductive adhesive (ACA) bonding, etc. Representing a higher level of integration and performance, such 2-D MCMs start to play a major role in fields where compactness and performance are of great desire, e.g., aerospace, military, and more recently, consumer portable electronics. Furthermore, 3-D IC integration of various types [5, 83, 12] has advanced the IC packaging to a new level. A number of bare die and MCM 3-D stacking technologies are emerging to meet the ever increasing demands for even higher level integration and performance of ICs.

In such a context, our multilayer via-bonding technology has the capability of providing a novel high-resolution, high-density interconnecting and packaging solution for direct bare die interconnection and packaging with the potential of forming advanced 3-D MCMs. More importantly, our technology has the inherent characteristics to facilitate such efforts—the via-bonding process is a CMOS-compatible, etch-free, and low-temperature process.
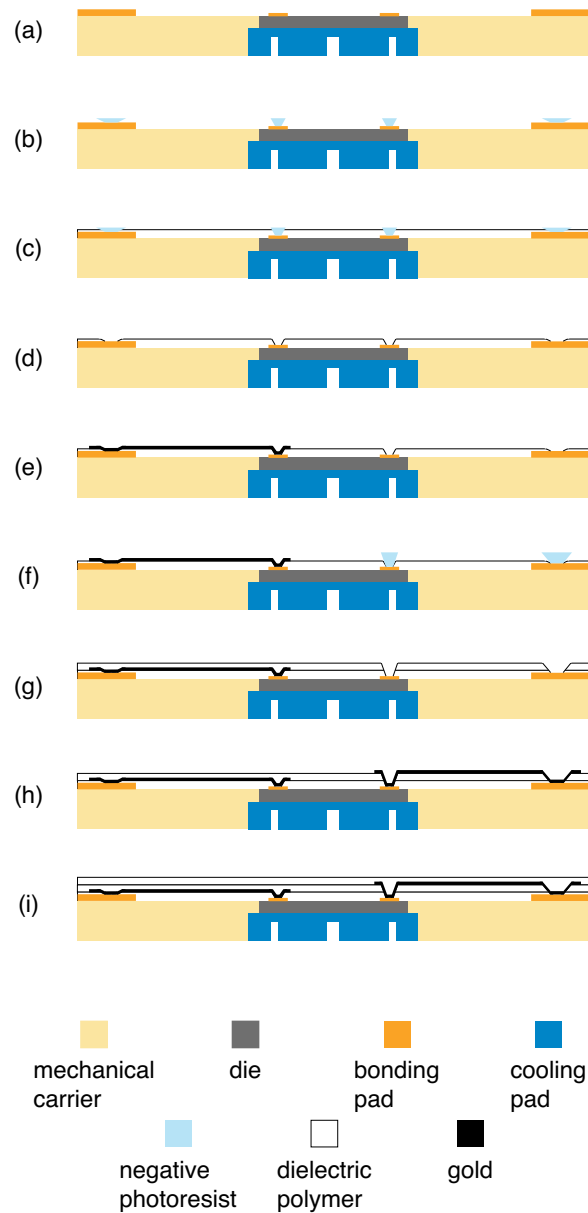
Figure 20: Cross sectional illustration of multilayer via-bonding process for CSP (not to scale).

4.5.1 Chip Scale Packaging

First, we demonstrate the application of our multilayer via-bonding technology to CSP by interconnecting and packaging a testing bare die on a PCB using two-layer interconnects. The PCB serves as the mechanical carrier of the chip and for electrical connection to external circuitry. The PDMS coating functions both to facilitate interconnections among bonding pads and to encapsulate the embedded chip and interconnects at the same time. The whole

61
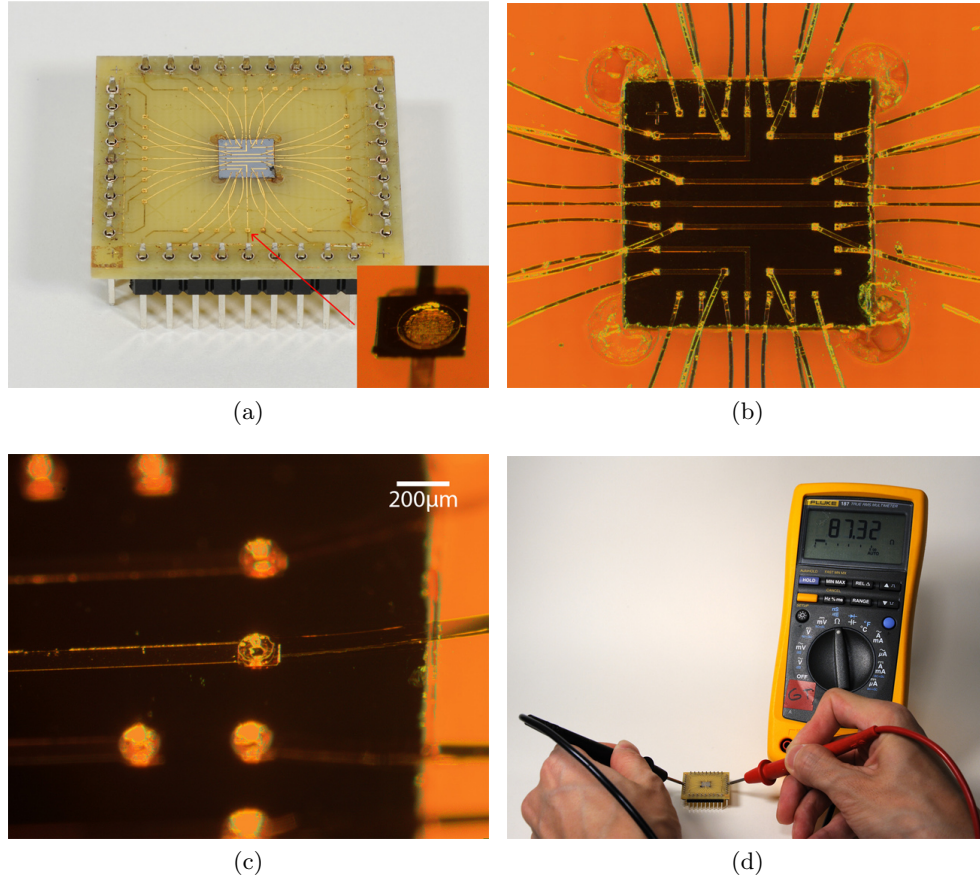
Figure 21: A testing chip packaged using two-layer via-bonding. (a) Photo of the device. The inset shows a via-bond on one contact pad of the PCB. (b) Microscopic image of the bonded chip. (c) Microscopic image of one via-bond on the die. (d) Electrical testing confirmed good electrical connection to the chip. In the testing route, there are four via-bonds, two on the die and the other two on the PCB.

device adopts an embedded overlay structure [25, 13].

The packaging steps are shown in Figure 20. The standard multilayer via-bonding process was used. The rigid PCB substrate was designed to have a metal cooling pad embedded in the center, and a shallow recess was milled in the PCB to house the bare die. The die was glued to the cooling pad using thermally conductive adhesive prior to the packaging process. Efforts were made to ensure that the die surface was in the same plane as the PCB surface. This is important for yielding a uniform film in a spin-coating process and for proper alignment and exposure in a photolithography process. The testing chip was design to have a few connected patterns (Figure 21b) to facilitate electrical testing of the multilayer interconnects. Figure 21 shows such a fabricated device. The inset in Figure 21a
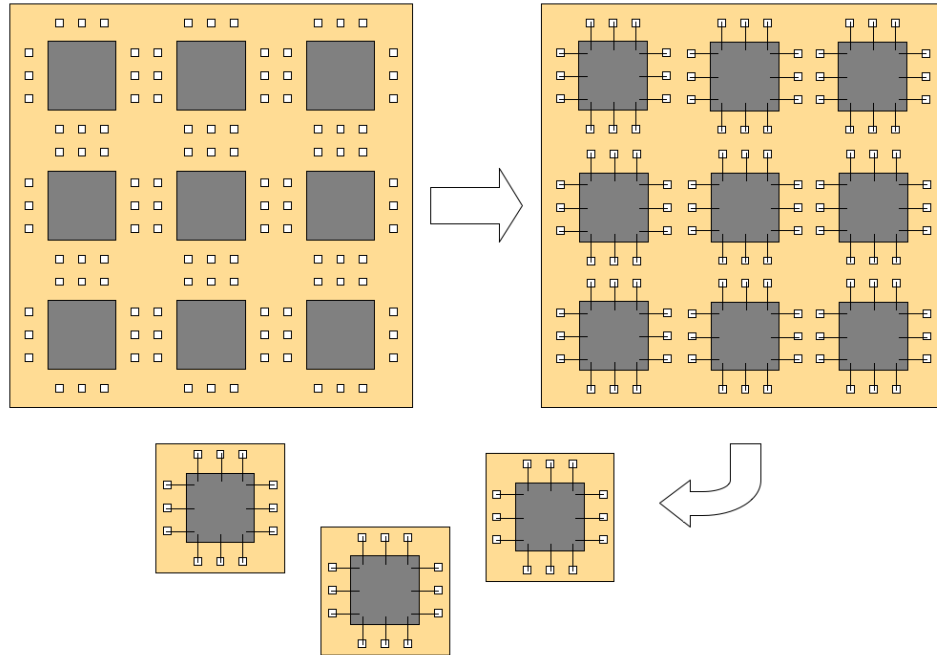
Figure 22: Illustration of batch-wise processing for via-bonding.

shows one via-bond on the PCB. The inclined via which bridges the interconnects on two different layers is clearly seen, so is that for the via-bond on the die in Figure 21c. Electrical testing using a multimeter (Figure 21d) confirmed successful electrical wirings to the die and good electrical isolation between interconnects on different layers.

For single chip packaging, although the demo device was designed to have a large package for the ease of handling in fabrication, the package can be designed small enough to meet the CSP criteria and can be easily adopted for a batch-wise fabrication process (Figure 22). For a CSP package, the interconnects between the die and the package would be very short, thus significantly reducing the parasitics and enhancing the performance.

Finally, it is attractive that no matter which packaging level (single chip, 2-D MCM, or 3-D MCM) an application requires, the fabrication can be conducted in a batch-wise manner, as illustrated in Figure 22. Units can be arranged in a larger mechanical carrier, packaged as a whole, and then diced into individual ones.

www.manaraa.com
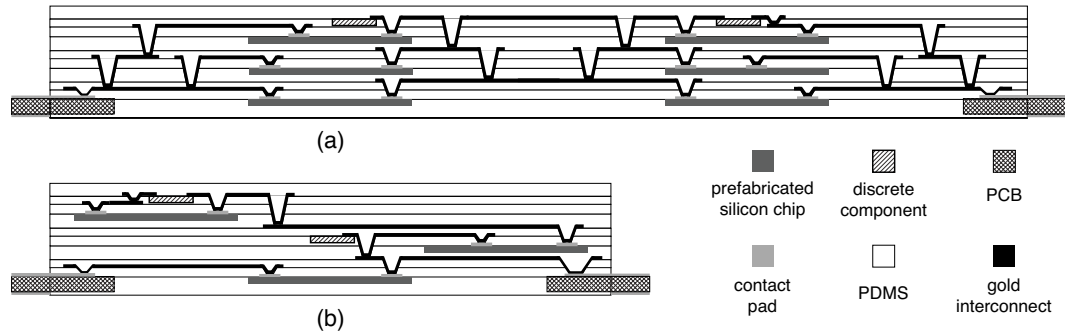
Figure 23: Architectures for elastic, multichip modules (not to scale). PCBs, prefabricated silicon ICs, and thin-film discrete components of various types can all be integrated into such a composite and interconnected using multilayer via-bonding technology to form a module-level circuit. (a) Components aggregate in stacked 3-D islands. This architecture can maximize the system-level stretchability. (b) Components are not stacked. This architecture gives more design flexibility.

4.5.2 Elastic Multi-Chip Module

Probably, one of the most prominent advantages that our multilayer via-bonding technology implies is the novel 3-D elastic MCM architectures as illustrated by the two example systems in Figure 23. Not only can the interconnects be embedded in multiple layers of the dielectric polymer, as is what other MCM technologies do [25, 103, 9], more importantly, thin components of various types (including, but not limited to, bare chips) can also be embedded in multiple component layers and connected electrically through multilayer via-bondings to achieve a module-level circuit, thus facilitating the integration of a heterogeneous system with an even higher capacity. For a component layer, after spin-coating the PDMS prepolymer but before fully curing, thin components can be stamped or printed on, and then followed by completion of the curing process. It is preferred that the components are thin, however, variances in component thickness can be accommodated by embedding thick components in a thick dielectric layer or even spanning them through multiple dielectric layers. In the bottom component layer, components do not have to be recessed into the mechanical carrier, as long as the bonding pads of different components are in the same plane. Multilayer via-bondings are then used to form the interconnections among the components at different layers.

In the first example system (Figure 23a), components are embedded and interconnected in PDMS to form stacked 3-D islands. This architecture can maximize the system-level

64

stretchability similar to the electronic-skin architecture [130, 70]. In the second example (Figure 23b), embedded components are not stacked, resulting in decreased stretchability but increased design flexibility as a result of easier wire routing. The resulting elastic, MCMs can interface with external circuits through exposed connections on the embedded PCBs. Such elastic MCMs may be rolled into a scroll or folded and thus forming more compact 3-D circuits. Alternatively, the two example systems can also sit on or adhere to a rigid substrate surface to form a circuit block. Similar to the electronic skin architecture [130, 70], these elastic MCMs can withstand mechanical deformations because the deformations are taken up largely by the exposed polymer substrate between the islands [70]. Because cured PDMS bonds to most rigid materials strongly (the bonding can be improved or strengthened by brief oxygen plasma treatment of the rigid substrate before applying PDMS coating), via-bonds on the rigid components are expected to be strong enough to withstand a significantly large amount of strains, and thus should not be the locations for causing mechanical failure during deformations, as had previously been revealed by the study from Lacour *et al.* on "glued" components [70].

4.6 Summary

In summary, we have addressed two major challenges associated with the fabrication of PDMS-based stretchable electronics—(1) increasing the integration density and (2) improving the electrical bonding by developing fabrication techniques that enable reliable multilayer interconnects both within the PDMS substrate and between the PDMS and a rigid substrate. This interconnect technology boosts the integration density by providing multiple layers of wiring in the flexible PDMS device. The PDMS–to–rigid-substrate interconnect facilitates robust, high-density electrical connections between the two materials. Taken together, these two integral parts facilitate a new high-density *multilayer via-bonding technology*. Applications of this technology to electronics packaging in general are exemplified by CSP and 3-D elastic MCMs.

CHAPTER V

THE PDMS-BASED SMEA TECHNOLOGY PLATFORM AND ITS BIOLOGICAL EVALUATIONS

In Chapters II, III and IV, I described a set of technological advances for the fabrication of PDMS-based sMEAs. In this chapter, I summarize these technological efforts and define an *integrated technology platform* for PDMS-based sMEAs. This technology platform is exemplified with sMEA designs for a few applications, including epimysial recording and stimulation, spinal cord surface stimulation, and peripheral nerve interfacing.

In the first part of this chapter, I summarize the technical strengths of our PDMS-based sMEA technology and include a gallery of sMEAs designed so far for different neural interfacing applications; in the second part, I provide *in vitro* and *in vivo* evaluations of these example sMEAs. In the next chapter, I will apply this PDMS-based sMEA technology to a prosthesis to address a clinical problem—unilateral vocal cord paralysis (UVCP).

5.1 Summary of PDMS-Based sMEA Technology

The complete set of technological advances described in previous chapters, ranging from microelectrode profile control to high-density interconnects to integrated packaging, constitutes an *integrated technology platform* for PDMS-based sMEAs. By tailoring these technical elements, sMEA designs can be customized for numerous neural interfacing applications. The technological strengths are summarized as following:

5.1.1 Technological Strengths

1. Uniform current density microelectrode profile designs at 10 μm resolution with easy controllability over the electrode recess depth, recess slope, and protrusion height (Figure 4c, Chapter II);

2. High resolution and high density interconnects:

   (1) High-density interconnects on each individual conducting layer with trace width

and spacing as small as 10 μm (Figure 11, Chapter III),

(2) a truly multilayer implementation that is simple in fabrication and reliable in application (Figure 18, Chapter IV);

3. Integrated packaging:

   High-resolution, high-density multilayer via-bonding technology featuring parallel-processed area-array bonding pads and multilayer wiring at 10 μm resolution with batch processing capability (Figures 21c, 22 and 23, Chapter IV);

4. In addition, there are a few other processing and application advantages:

   (1) Etch-free and low temperature processing ($\leq$ 90 ℃), CMOS compatible,

   (2) microfluidics integratable,

   (3) additional application modes: penetrating and microchannel PDMS-based MEAs [33, 34, 72].

5.1.2   Device Gallery

Figure 24 lists the example sMEA designs we have fabricated so far for applications including spinal cord surface stimulation (Figure 24a), epimysial recording and stimulation (Figures 24b, 24c and 24d), and peripheral nerve interfacing (Figures 24e and 24f).

5.2   In Vitro and In Vivo Evaluations

In this section, we performed *in vitro* and *in vivo* experimentations to evaluate the biocompatibility, surface conformability, and surface recording/stimulation capabilities of the example sMEAs, with a focus on epimysial applications.

5.2.1   Short-Term Biocompatibility—Dissociated Neural Culturing

5.2.1.1   Methods

Cortical neurons were derived from embryonic day 17–18 rat fetuses by isolating the cerebral cortices, and dissociating them with trypsin (0.25%) + 1 mM EDTA (10 minutes at 37 ℃) followed by DNase (0.15 mg/mL). These neurons were plated on the sample sMEAs at densities of approximately 1 x 10^5 and 5 x 10^3 cells/μL, to form high and low concentration

67
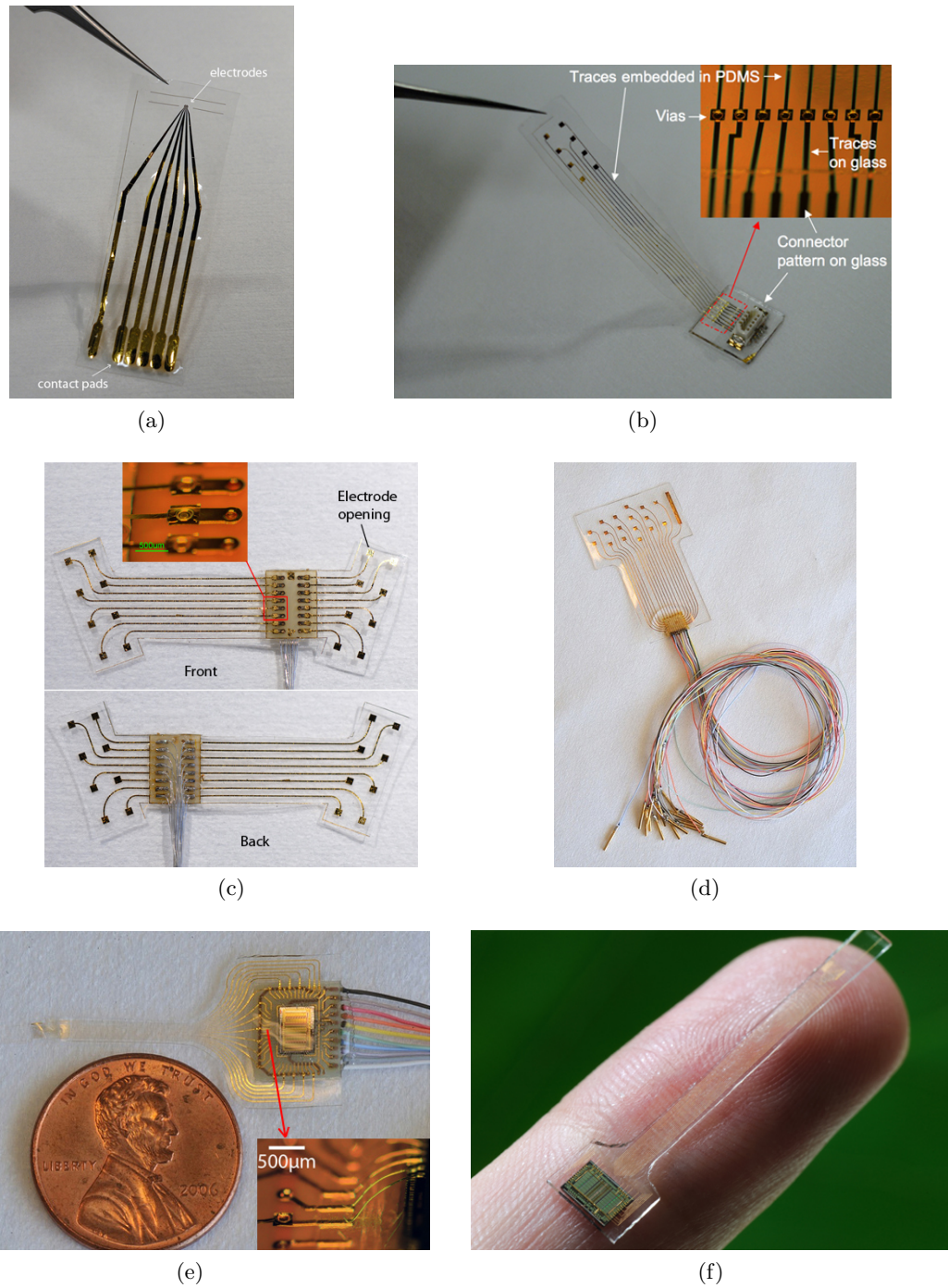
Figure 24: PDMS-based sMEA gallery. (a) An early version for spinal cord surface stimulation [48]. (b) A glass-integrated version for epimysial recording and stimulation [47]. (c) A PCB-integrated version for vocal cord prosthesis [45]. (d) A PCB-integrated 16-channel version for multichannel epimysial recording on a cat muscle. (e) An IC-integrated 16-channel version for peripheral nerve interfacing [46]. A chip-on-board architecture is used to incorporate a 16-channel amplifier die (RHA1016, Intan Technologies, UT) into the device. (f) A direct IC-integration strategy. A 16-channel amplifier die is directly integrated using via-bonding technology.

68
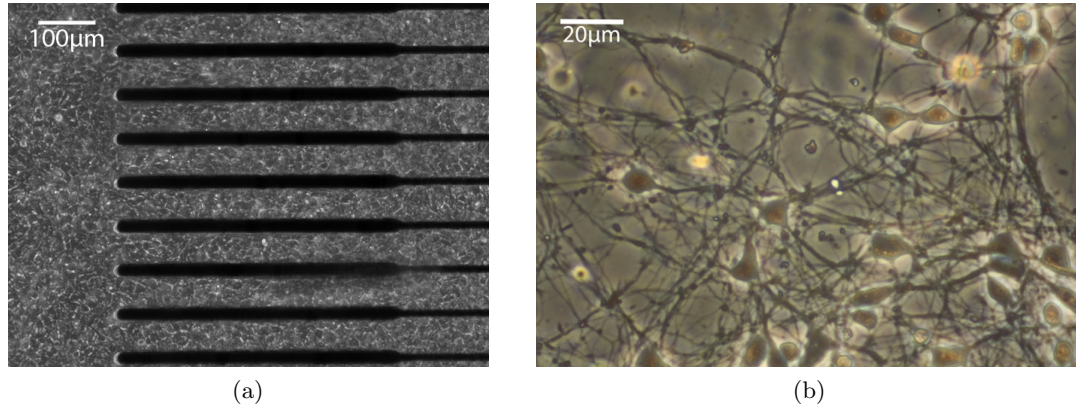
Figure 25: Dissociated neural culturing on the sMEA surface. (a) High-density culture. (b) Low-density culture.

cultures respectively. Before neuronal plating the surfaces of the sample sMEAs were treated with polyethyleneimine (PEI), thoroughly washed, fixed to the bottom of a culture well, and coated with laminin. The cultures were fed neuronal medium (Neurobasal medium + 2% B-27 + 500 μM L-glutamine) and maintained in a tissue culture incubator (35℃, 5% CO_2, 9% O_2) for $2-3$ weeks.

5.2.1.2 Results

We evaluated the short-term biocompatibility of the fabricated devices by testing if there were any cytotoxic chemicals from the fabrication processes left in the final devices. The neural culturing experiment was encouraging. As shown in Figure 25, the cortical neurons grew happily on the sMEA surface for a period of $2-3$ weeks, with extensive neurite growth (Figure 25b). This experiment verified that no cytotoxic chemicals were adsorbed on the device surface after fabrication. However, further experiments need to be conducted to test whether any toxic chemicals, potentially embedded in the device body, migrate to the surface after a prolonged period of time. In addition, the degradation rate of device materials and the toxicity of the material derivatives need to be assessed.

5.2.2 Surface Conformability

One of the major mechanical advantages of PDMS derived from its low Young's Modulus is that PDMS thin films (e.g., $\leq 100 \ \mu m$) are highly conformable—a property highly valued

69
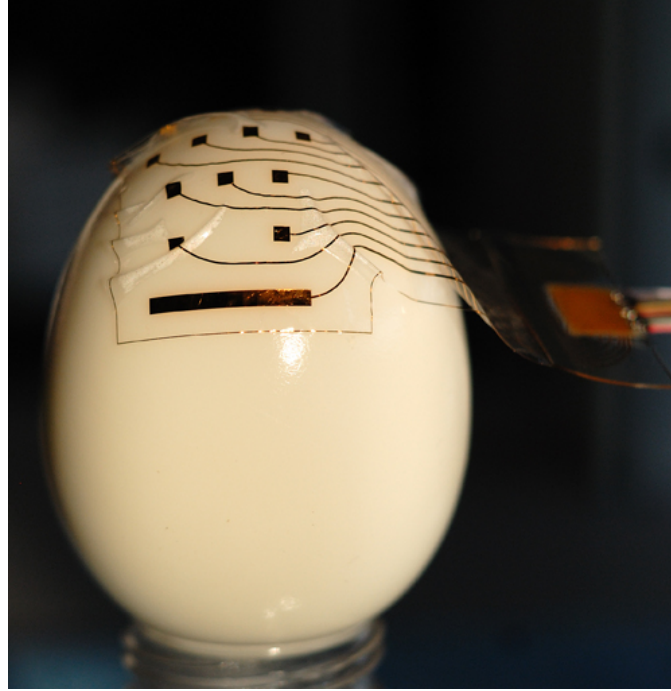
Figure 26: Demonstration of the surface conformability of an sMEA. The sMEA was placed on a boiled egg (shell removed). The thickness of the sMEA head is 60 μm.

in neural surface interfaces. To demonstrate the surface conformability of the PDMS-based sMEA, a sample sMEA (similar to the one in Figure 24d, but with a thickness of 60 μm in the head area) was placed over a boiled egg surface (Figure 26). The device conformed well to the curved egg surface. When this sMEA was placed on the medial gastrocnemius (MG) muscle of a cat, the device also conformed closely to the curvatures of the muscle (Figure 31). From a mechanics calculation [63], the minimum conformal wrapping radius for such a 60 μm thick PDMS-based sMEA is 1.4 mm. This conformability of PDMS, combined with its elastomeric nature, highlights the unique advantages held by PDMS-based sMEAs for epimysial interfacing applications.

5.2.3   Epimysial Interfacing

Electrical recordings of skeletal muscle activity provide information that can assist in the diagnosis of neuromuscular diseases and serve as command sources for prosthetic control. There are three modalities for muscle interfacing: transcutaneous, epimysial, and intramuscular (Figure 27), among which the epimysial method falls as a trade-off between the other
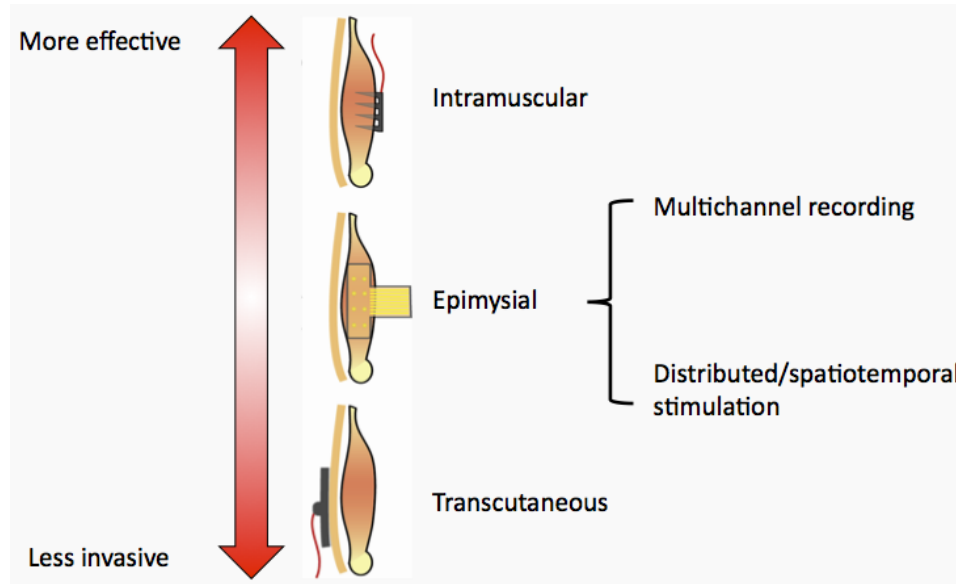
Figure 27: Three modalities for muscle interfacing in FES: transcutaneous, epimysial, and intramuscular.

two with respect to efficacy and invasiveness. Although the intramuscular method is the classical technology for investigating the properties of individual motor units, recent emerging high-density flexible MEA technologies have also enabled its analysis by non-invasive, high-density electromyogram (EMG) recorded over the skin surface (i.e. using the transcutaneous method) [95]. The analysis of motor units from surface EMG is useful when the insertion of needles is neither desirable nor possible. Moreover, surface electromyography allows for the measurement of motor unit properties which are difficult to assess with invasive technology (e.g. muscle fiber conduction velocity or location of innervation zones) and may increase the number of detectable motor units with respect to selective intramuscular recordings [95]. However, most of the work on multichannel muscle surface recordings employs flexible MEAs transcutaneously [95, 74, 127, 84], in which the efficacy is low. High-density flexible/conformable MEA applications in epimysial recordings have been rare. Meanwhile, only a few studies involving stimulation with discrete epimysial electrodes have been reported [41, 3, 115, 55, 44].

The dearth of high-density epimysial recording and stimulation applications is primarily due to the lack of appropriate high-density flexible/conformable MEA technologies. Excitingly, enabled by our high-density PDMS-based sMEA technology, there is great potential

for novel high-density epimysial recording and stimulation research. Two exciting opportunities are under consideration: (1) multichannel epimysial recording that helps to reveal the underlying mechanisms of muscle electrophysiology during behavior related activities; and (2) distributed/spatiotemporal epimysial stimulation that can activate the muscle in a manner more similar to the natural order of recruitment, i.e. to improve muscle performance while reducing fatigue. In the following three epimysial interfacing experiments, I present our preliminary efforts toward these directions, with the long-term goal of developing a prosthesis for unilateral vocal cord praralysis (UVCP) through simultaneous epimysial recording and stimulation (see Chapter VI).

5.2.4 Finite Element Modeling of the sMEA as an Epimysial Interface

Although PDMS films can withstand uniaxial strains greater than 200% [88], metallic interconnects usually break at strains substantially lower in magnitude [130]. To better understand the mechanical properties of our sMEAs, we created a finite element model of the device to simulate its response to epimysial interfacing conditions. This work was helped by Mr. Xi Liu from the Mechanical Engineering Department of Georgia Tech.

5.2.4.1 Methods

To simulate the epimysial mechanical performance of the sMEA as in Figure 31, we constructed a three-dimensional finite element model using Abaqus FEA (ABAQUS Inc.) running on a 32GB memory server. As shown in Figure 28, the sMEA head was laid with electrodes facing down on a PDMS stretching substrate (210 x 124 x 10 mm) to mimic the epimysial interfacing application. All dimensions of the sMEA head were the same as the real device in Figure 31, except that 300 nm thick gold interconnects were used in the model instead of 500 nm in the real device. Specifically, the sMEA head model consisted of a 50 μm thick PDMS base layer, 300 nm thick gold interconnects, and a 10 μm thick PDMS insulation layer. The electrode openings were 1 mm in diameter. The PDMS stretching substrate was designed to serve as a simple model of a muscle surface, to which a 5% uniaxial strain, either longitudinal or transversal, was applied to simulate muscle contraction.

A viscoelastic model [81] was used for the PDMS material; and an elastoplastic model [125]
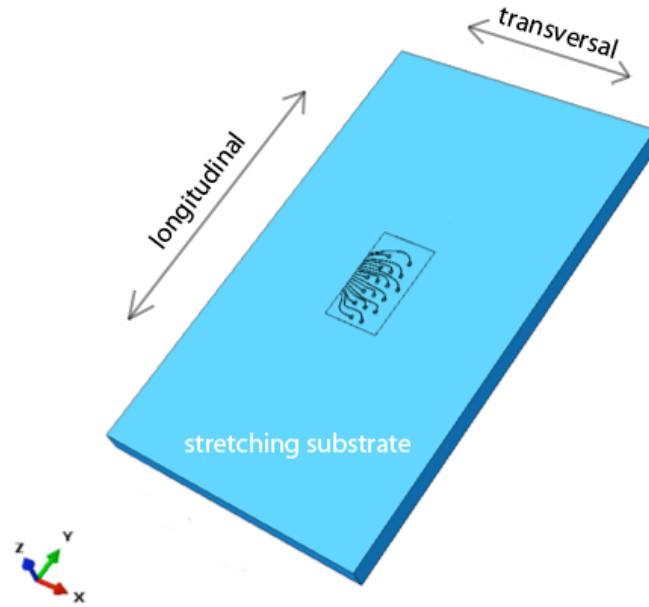
Figure 28: Finite element model for simulation of the sMEA's mechanical performance as an epimysial interface. The sMEA head was laid with electrodes facing down on a 1 cm thick PDMS stretching substrate to mimic the epimysial interfacing application as in Figure 31. Five percent uniaxial strain was applied to the PDMS substrate either longitudinally or transversally.

was used for the thin-film gold. The ultra-thin Ti adhesion layer (30 nm thick) between the gold film and the PDMS substrate in the actual sMEA was neglected to reduce the difficulty and computational complexity of the simulation. It was assumed that all materials were isotropic and that the interfacial bonding between the sMEA and the PDMS stretching substrate was perfect.

Two different sets of boundary conditions, longitudinal (Y direction) and transversal (X direction), were applied to this model to study the sMEA's mechanical performance under uniaxial loading conditions. When applying a 5% strain, either longitudinally or transversally, the PDMS stretching substrate was fixed on one side, and a displacement was uniformly applied on the surface of the opposite side. The resulting strain in the gold interconnects was then analyzed.

5.2.4.2   Results

Figures 29a and 29b show that when a 5% uniaxial strain was applied to the stretching substrate, a strain of ~3.5% was induced in the majority parts of the gold interconnects.

73
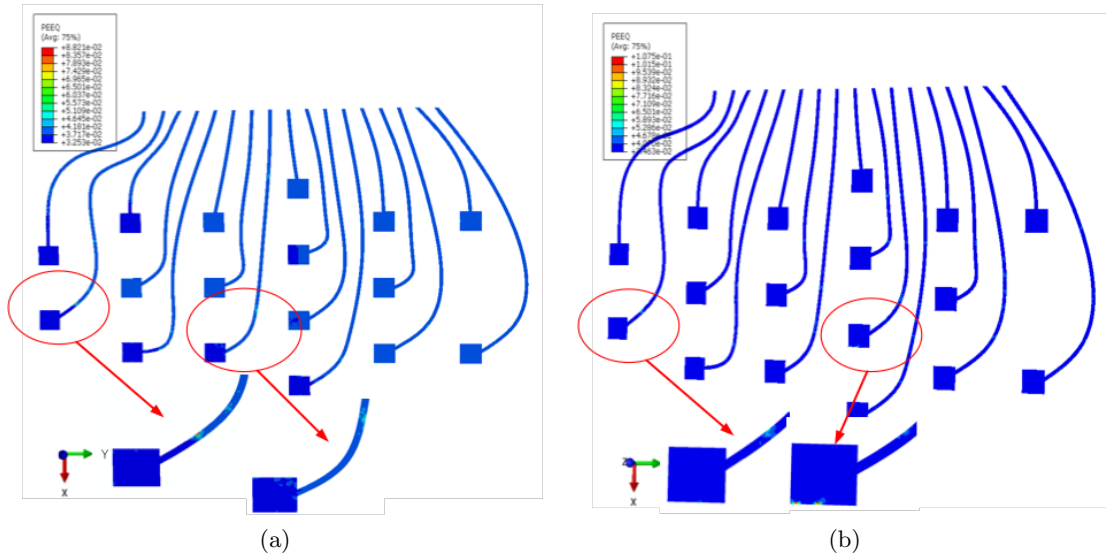
Figure 29: Finite element modeling of the sMEA's mechanical performance under epimysial interfacing conditions. (a) Equivalent strains in the gold interconnects under longitudinal (Y direction) loading (5% average strain on the stretching substrate). (b) Equivalent strains in the gold interconnects under transversal (X direction) loading (5% average strain on the stretching substrate). Close-up views are provided in each figure to reveal the sites where excess strains were generated.

However, regions of large curvature or geometric transition experienced strains greater than 8%. It was also found that transversal loading (loading in the X direction) resulted in slightly higher strains in the gold interconnects than that induced by longitudinal loading.

The finite element modeling revealed intuitively how the strain generated in the interfaced substrate was transferred into the gold interconnects and provided insights into layout of the interconnects during sMEA designing. However, it is worth noting that there are two major limitations of this model. First, perfect bonding was assumed between the sMEA and the stretching substrate, whereas in an epimysial interface, a physiological solution layer exists between the sMEA and the muscle surface. This solution layer acts to reduce the degree of strain that can be effectively transferred to the sMEA, so the actual strains induced in the gold interconnects should be smaller than the simulation results. Second, loading conditions below the fracture limit cause micro cracks to develop in the gold film in response to the elongation of the elastomeric substrate. These micro cracks release the induced stress and allow the traces to maintain electrical conductivity in the form of a percolating network [69]. This mechanism was not implemented in our finite element model. In actual gold interconnects under a strain loading, when excess strains develop at the characteristic sites

74

(Figures 29a and 29b), micro cracks are probably generated to release the embedded stress in the gold film, and the interconnects would still maintain their electrical conductivity as a whole, albeit that the interconnect resistance will increase. Encouragingly, it was reported that an sMEA could maintain relative stable electrode impedances even with the increase of interconnect resistance under uniaxial strain loadings [99]. Therefore, the actual strain induced on the gold interconnects of an sMEA under epimysial interfacing conditions can be substantially lower than the fracture limit that completely breaks the interconnects, and may have little effect over the electrode impedance and EMG signal fidelity. These analyses thus help to validate the sMEA's capability as an epimysial interface, and, indeed, the sMEAs functioned properly in both of our epimysial recording and stimulation experiments as described below.

5.2.5 Multichannel Epimysial Recording—Frog Muscle

The work presented here was published in Ref. [47].

5.2.5.1 Experiment Setup

The experiment setup for multichannel epimysial recording is shown in Figure 30a. The gastrocnemius muscle from one frog hind leg was dissected with the sciatic nerve attached, fixed at the ankle end, and attached by suture to a force transducer at the knee end. An eight-electrode connector-integrated sMEA (Figure 24b) was wrapped around the muscle surface radially with the four electrodes used labeled corresponding to the respective recording channels. The sMEA connector was plugged into a PCB pre-amplifier. The recording reference electrode was placed on another piece of muscle that was in a resting state throughout the experiment. The sciatic nerve was stimulated using a hook bipolar electrode with 100 μs/1 mA monophasic current pulses. Four-channel EMG signals and the contraction force were recorded. The amplifier settings for EMG recording were: gain = 1000, lowpass = 2 kHz, and highpass = 1.0 Hz.
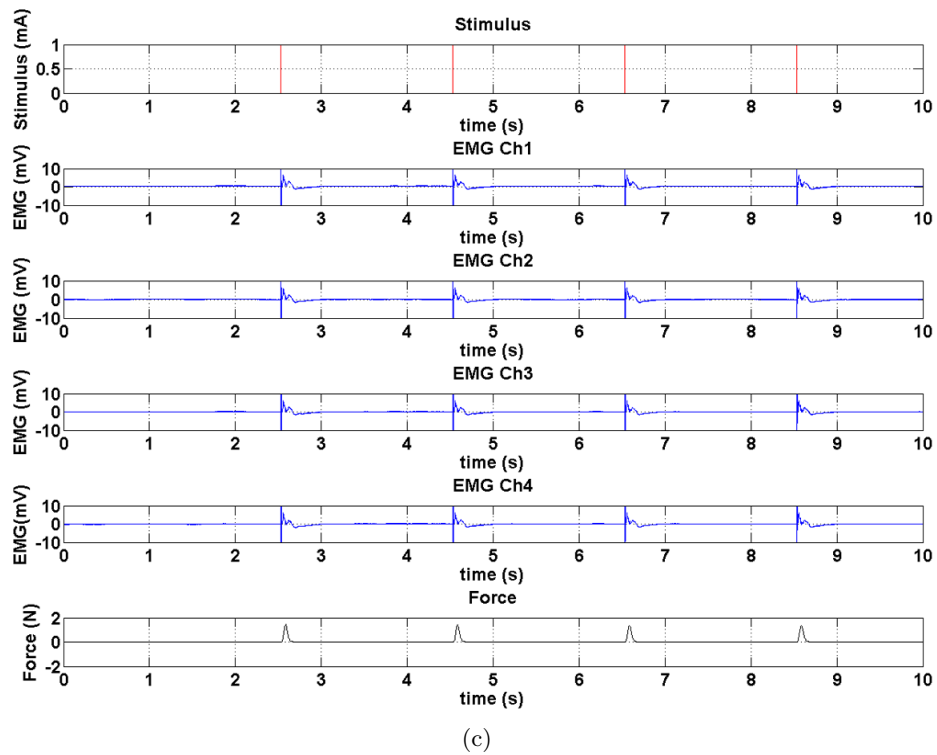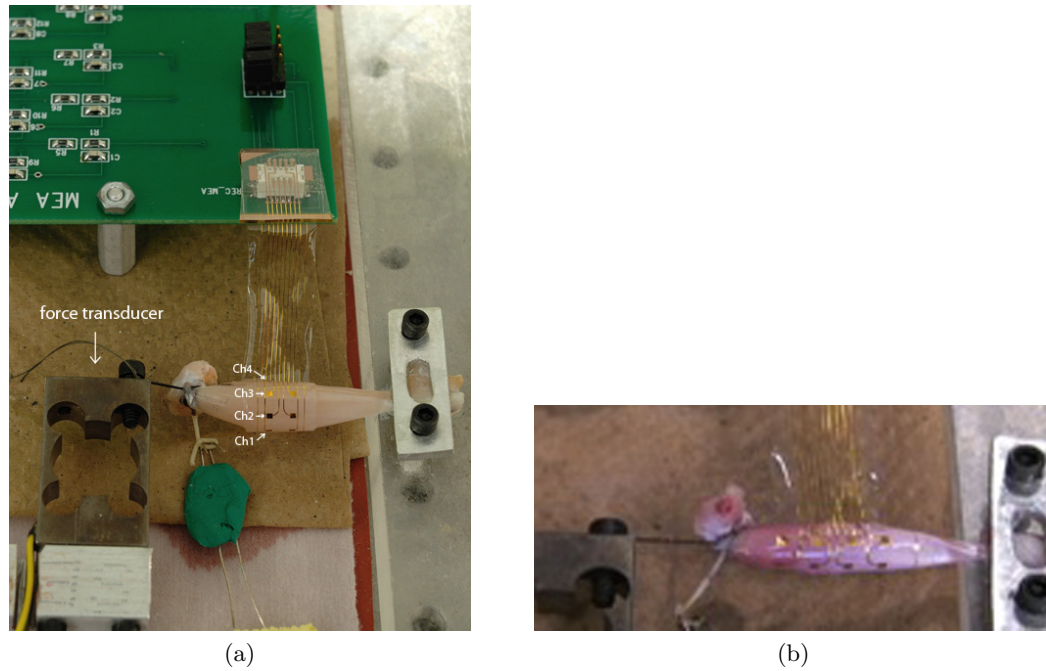
Figure 30: Multichannel epimysial recording—frog muscle. (a) Experiment setup. The thickness of the sMEA is 50 μm. (b) Snapshot of a maximal muscle contraction during a similar setup. (c) Recording data: stimulus (top), four-channel EMG signals (middle), and contraction force (bottom).

In this experiment, we have successfully demonstrated the multichannel epimysial recording capability of the sMEA. The sMEA showed good surface conformability with reliable signal recording even at maximal muscle contractions (Figure 30b).

Because the whole sciatic nerve was stimulated synchronously and, as a result, all the motor units were activated at the same time, the commonly known high-frequency interference pattern of the compound action potential (CAP) caused by asynchronous activation of the many motor units was not seen, instead, low-frequency EMG signals (Figure 30c) were recorded, which were CAPs under synchronous activations. In addition, because the four recording electrodes were placed on the muscle surface along a circumference perpendicular to the fiber direction, the monopolar recording data in Figure 30c indicates identically distributed and synchronized electrical potentials under such a whole-nerve stimulation condition.

5.2.6 Multichannel Epimysial Recording—Cat Muscle

In this study, we further investigated the epimysial recording capability of the sMEA on a cat medial gastrocnemius (MG) muscle. These efforts lay the foundation for future multichannel epimysial recording using this type of sMEA.

5.2.6.1 Experimental Methods

All experimental procedures within this study were conducted in accordance with the guidelines of the National Institutes of Health and the Georgia Tech Institutional Animal Care and Use Committee. In the experiment, the cat was tracheostomized to control for its isoflurane anesthetic levels. The brainstem was transected at a 45° angle, rostral to the mammillary bodies, with the subthalamic nucleus preserved, and all rostral brain tissue removed. The tendon of the right limb MG muscle was detached from the insertion and clamped while the right knee was fixed. This muscle preparation was performed to reduce the introduction of movement artifacts during the recording of EMG activity. A bipolar
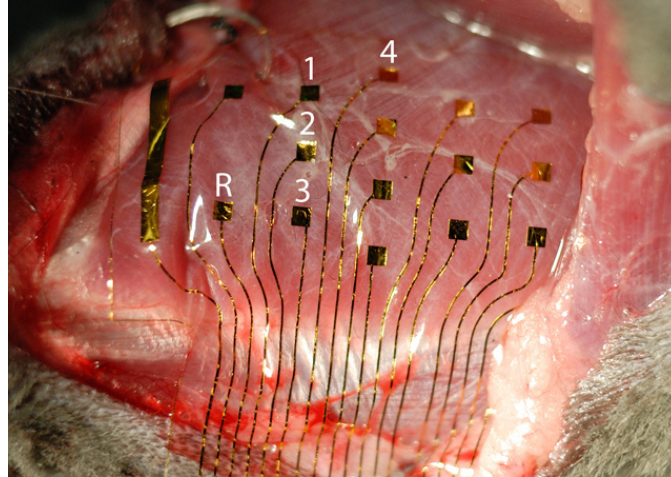
Figure 31: Multichannel epimysial recording—cat muscle. The sMEA was placed on the right cat MG muscle. Bipolar configurations were used with the common reference electrode marked as "R".

electrode was implanted adjacent to the left tibial nerve for the purpose of electrically inducing a crossed extensor reflex, and a ground electrode was implanted in the fascia of the right hind limb. Following completion of the surgery, the cat was taken off anesthetic. Recordings performed on the preparation were utilized for other purposes as well. The animal was euthanized at the completion of the experiment with concentrated pentobarbital.

The sMEA was placed upon the surface of the right MG muscle (see Figure 31) which was activated through a crossed extensor reflex by electrically stimulating the left tibial nerve with 100 μs/0.8 V square pulses at 40 Hz. Twelve electrodes on the sMEA were configured for bipolar recording with an electrode at the periphery used as the common reference (denoted by "R" in Figure 31), and the sMEA cable was connected to the input terminals of a custom-built 12-channel amplifier. Recorded signals were amplified by a gain of 1000 and then digitized at a sampling rate of 3.6 kHz/channel before being sent to the computer. No real-time filtering, neither through hardware nor through software, was applied to the raw data.

Post data processing was performed using Matlab 7.0 (MathWorks, Inc.). Digital filters were designed and applied to the raw data to remove noise. Specifically, a 60 Hz comb filter was used to remove the 60 Hz electromagnetic noise; a 40 Hz comb filter was used to remove the stimulation artifacts; and a fourth-order Butterworth bandpass filter (0.15 Hz $\sim$ 1 kHz)

www.manaraa.com
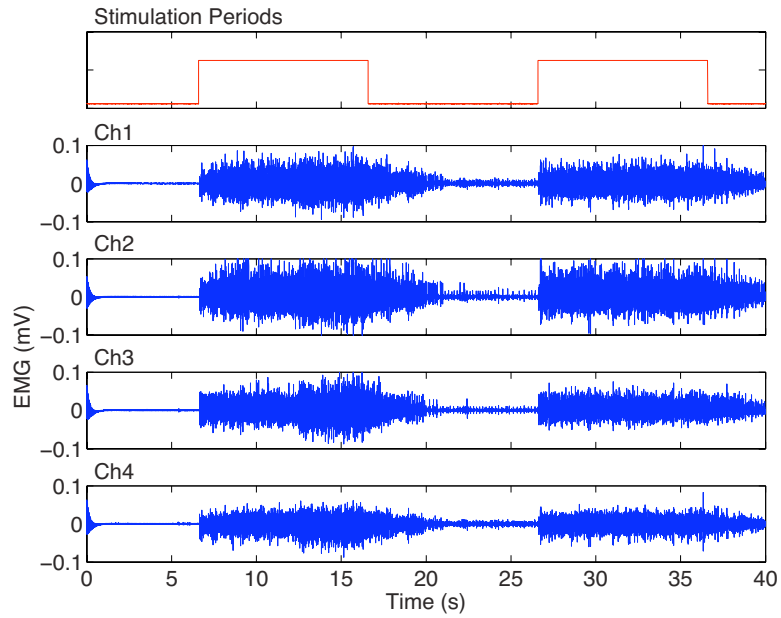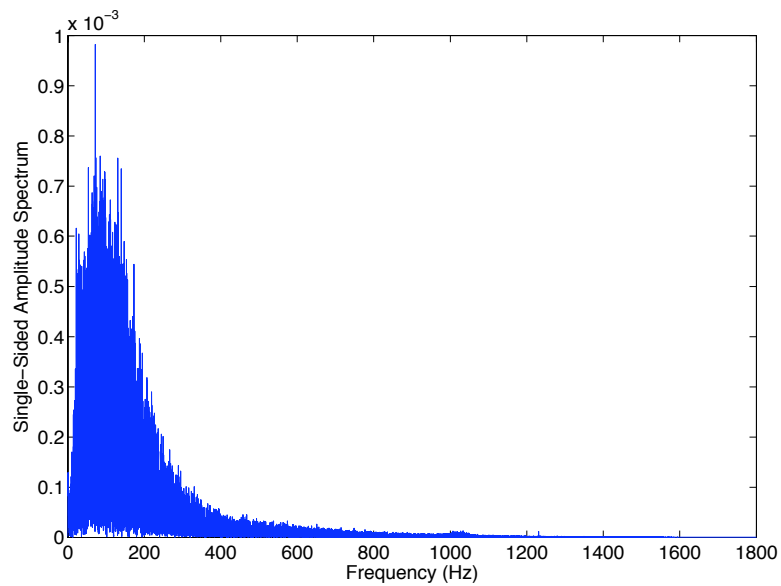
Figure 32: (a) Sample bipolar EMG recordings from the right MG during a crossed extensor reflex (blue). The first four channels as marked in (a) are shown. The red square waves mark the stimulation periods. (a) Frequency spectrum of the recording of Channel 1.

was used to eliminate noise of lower and higher frequencies.

5.2.6.2 Results

Figure 32a shows sample recordings from the first four bipolar channels, which are marked in Figure 31 with the common reference electrode denoted by "R". The frequency spectrum
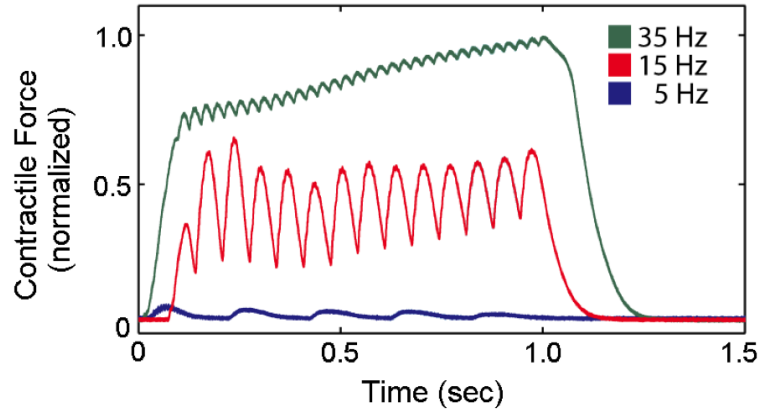
Figure 33: Muscle force responses to different stimulation frequencies.

of the first recording is shown in Figure 32b. The recordings have the typical appearance of EMG signals, with the signal power accumulated primarily under 400 Hz. Preliminary analyses of both the time and frequency domains showed that the signals from each channel had different characteristics, suggesting that the electrical potential across the muscle surface was not uniform. Experiments are ongoing to further investigate such a spatiotemporal pattern and its relationship to the underlying physiology.

5.2.7 Multichannel Epimysial Stimulation—Frog Muscle

In FES, low frequency stimulation results in ripple (Figure 33). To achieve a fused tetanus, high frequency stimulation is required. However, higher frequency stimulation causes muscle to fatigue more quickly. We have shown preliminarily that spatiotemperal epimysial stimulation protocols (i.e. interleaved stimulation [92]) could improve muscle performance while reducing fatigue. The work presented here was published in Ref. [56].

5.2.7.1 Stimulation Protocols

An eight-electrode sMEA (similar to the one in Figure 24b but with electrodes arranged transversely, see Figure 34b) was configured with each vertical electrode pair as a bipolar electrode. We compared the force responses to an interleaved 60 Hz stimulation (Int60) to those to simultaneous 15 Hz (Sim50) and 60 Hz (Sim60) stimulations. Figure 34a illustrates the three stimulation protocols. For the Sim60 and Sim15 protocols, stimulation pulses were

80
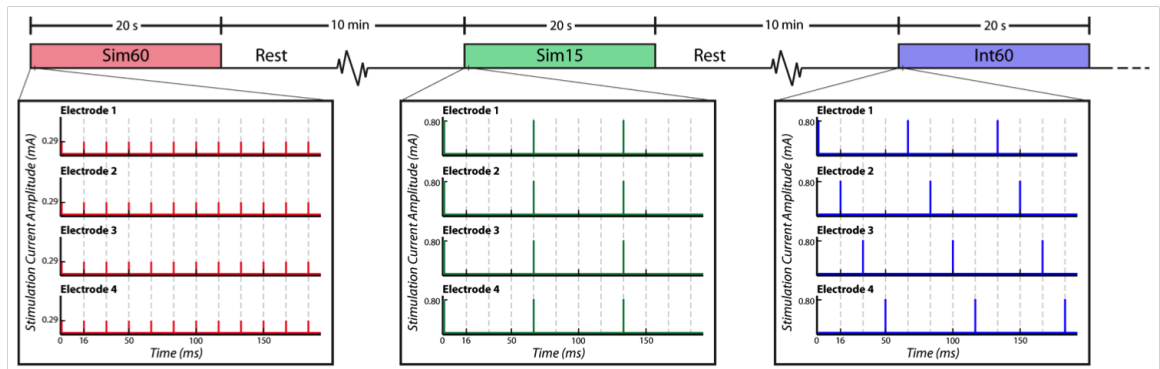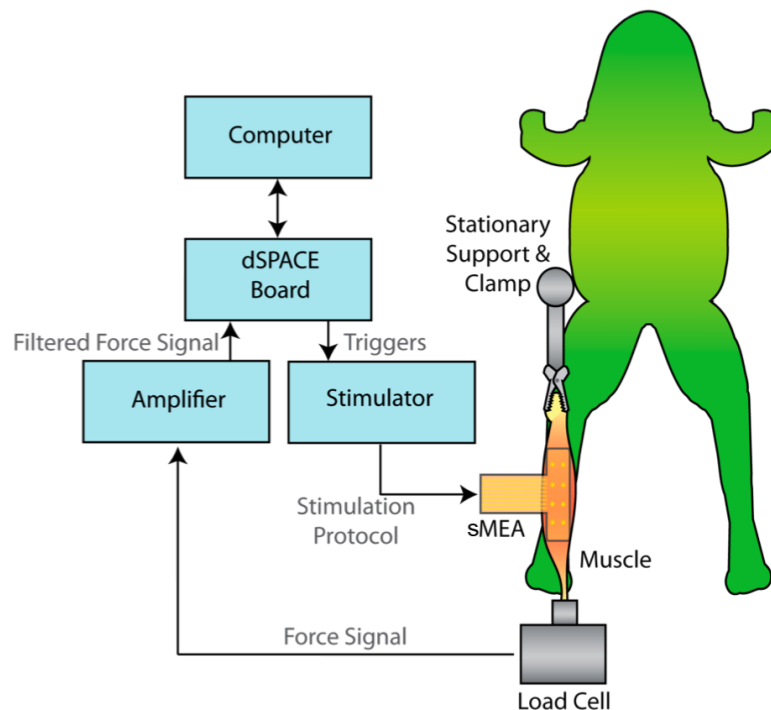
Figure 34: Multichannel epimysial stimulation—frog muscle. (a) Stimulation protocols. (b) Experiment setup.

delivered simultaneously to each electrode pair at 60 Hz and 15 Hz, respectively. For the Int60 protocol, stimulation pulses were delivered asynchronously to each electrode pair at 15 Hz. Each successive pair of electrodes was out of phase with the previous electrode pair by 16.66 ms such that the composite frequency of all four electrode pairs was 60 Hz. Current amplitudes were chosen, based on a calibration experiment, such that the peak values of the normalized average force responses to each stimulation protocol were approximately the

same. The amplitude of the current delivered to each electrode pair for the Sim60 protocol was 0.290 mA, while the Sim15 and Int60 protocols were both delivered at 0.800 mA to each pair. The stimulation pulse width was 200 μs for all three protocols. During a fatigue trial, the Sim60, Sim15, or Int60 stimulation protocol was randomly selected and delivered for a 20 s duration. The muscle was then given 10 minutes to rest before the next trial began. Totally, 17 trials were conducted: 6 for Sim60, 5 for Sim15, and 6 for Int60.

5.2.7.2 Experiment Setup

Figure 34b illustrates the experiment setup. The frog plantaris longus muscle, composed mostly of fast-fatiguable muscle fibers, was dissected and fixed to a clamp at one end and to a force transducer at the other. The muscle length was held fixed through the experiment. The sMEA, connected to a multichannel stimulator (STG-2008, Multi Channel Systems), was wrapped longitudinally on the muscle surface.

5.2.7.3 Results

We quantified the fatigue and ripple performances of different stimulation protocols. As shown in Figure 35a, the normalized average force response to Int60 stimulation has temporal characteristics falling between those to Sim15 and Sim60 stimulations, implicating a compromised fatigue performance. In Figure 35b, fourier transforms of the average force responses were plotted to reveal the frequency components that contribute to the ripple noise. Again, the performance of Int60 stimulation is a trade-off between those to Sim15 and Sim60 stimulations.

To summarize, the interleaved stimulation delivered epimysially through an sMEA results in less ripple and less fatigue compared to responses to low and high frequency simultaneous stimulation, respectively. But, the results are still just a trade-off. Ideally, we would like to more closely mimic the natural order of recruitent. And this goal could possibly be achieved through more complex spatiotemporal stimulation protocols.
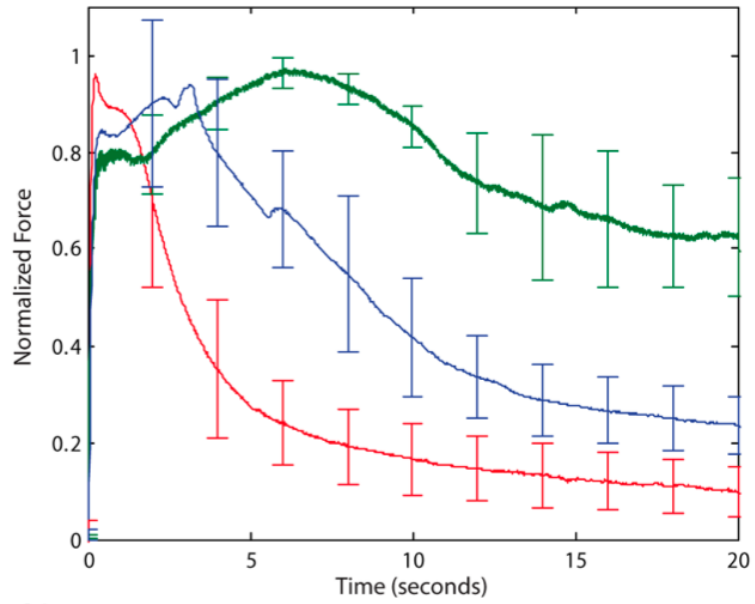
(a)
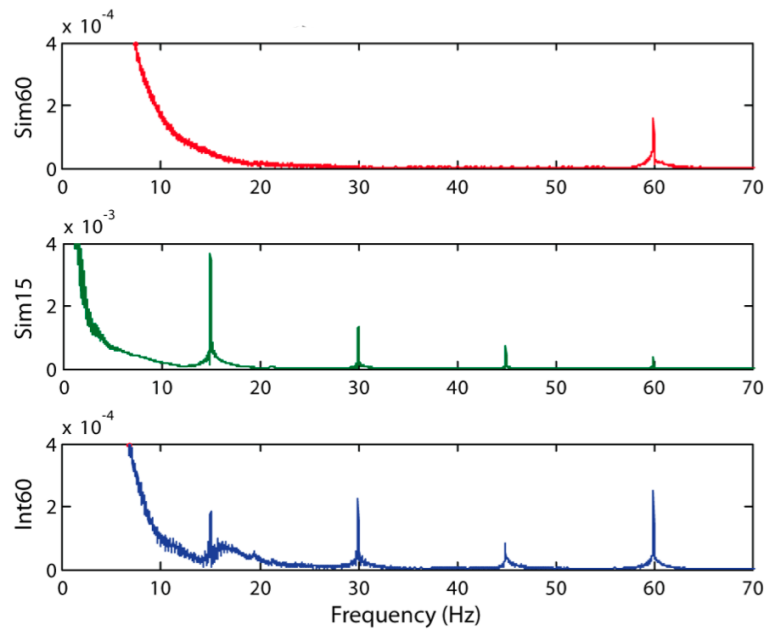
(b)

Figure 35: Multichannel epimysial stimulation results. (a) Normalized force responses to stimulation protocols. (b) Fourier transform of average force responses. The two plots share the same color code: red for Sim60, green for Sim15, and blue for Int60.
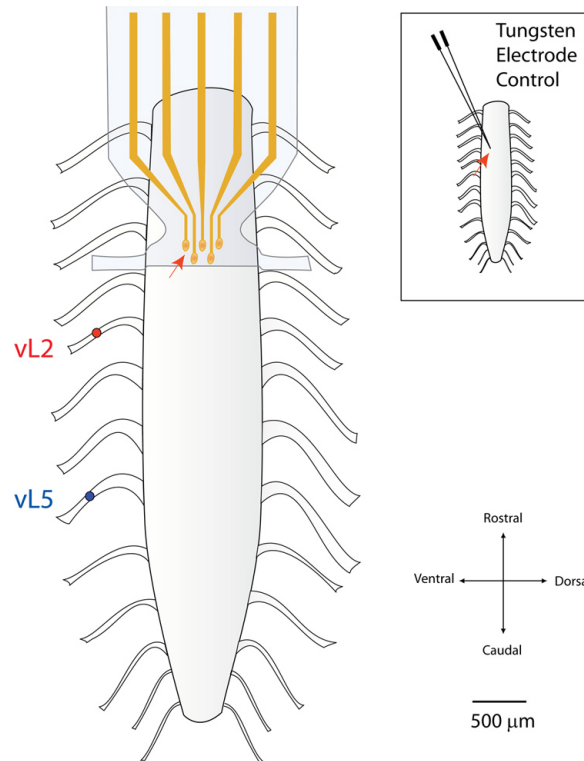
Figure 36: Experimental setup for comparing spinal cord responses to surface stimulation with the conical-well sMEA *vs.* rigid tungsten electrode. Studies were performed to determine the capability of the conical-well sMEA to access motor circuitry in the *in vitro* rat isolated spinal cord, as compared to a rigid tungsten microelectrode (inset, placed on location immediately between the two left-most sMEA electrodes, location indicated by arrows). Single-pulse stimuli were delivered to the surface of the cord and motor output responses were recorded at ventral roots L2 (vL2, red) and L5 (vL5, blue).

5.2.8 Stimulation of the *In Vitro* Spinal Cord

Originally, our PDMS-based sMEA was developed for spinal cord surface stimulation. Here, we give preliminary experimental results on surface stimulation of spinal white matter tracts implicated in activating locomotor behavior [52], demonstrating that the sMEA is similar to rigid tungsten microelectrodes in its ability to evoke ventral root outputs via spinal cord surface stimulation. For extensive evaluation of the sMEA's capability in selective surface activation of motor circuitry in the injured spinal cord, please refer to Dr. K. W. Meacham's Ph.D. thesis [94].

5.2.8.1 *Experiment Setup*

To evaluate the surface stimulation capability of the conical-well sMEA (Figure 4), an *in vitro* preparation of isolated rat spinal cord was used [54]. Preparation of spinal cords was

www.manaraa.com

accomplished as detailed previously [117]. Viability of the spinal cord was confirmed prior to and throughout experimentation by observing evoked reflexes in the L2 ventral root following dorsal root L2 stimulation (using bipolar, glass suction stimulating and recording electrodes). The degree of hindlimb-associated motor outputs elicited via sMEA surface stimulation was compared to that evoked by a conventional rigid tungsten microelectrode. The conical-well sMEA was wrapped around the spinal cord such that its electrodes made continuous contact with the cord surface (Figure 36). Two-dimensional position of the stimulating electrode pair was mapped relative to pinned roots at T10 and T12 using a microscope grid eyepiece (resolution < 50 μm; Leica). The comparison rigid tungsten microelectrode pair (5 μm tip diameter, $20 \sim 50$ μm inter-electrode distance, Harvard Apparatus, Inc.) was pressed onto the cord surface at the same stimulus location either before or after sMEA stimulation trials, using grid measurements for accurate placement. The sMEA (through a custom-made electrode clamp, Figure 21a) and the tungsten electrode pair were both connected to a multichannel stimulator (STG-2008, Multi Channel Systems). Single, rectangular current pulses (500 μA/50 μs) were applied to compare responses using the two different electrode types. A total of three isolated spinal cords were studied. For two of the spinal cords, an adjacent pair of sMEA electrodes stimulated the dorsolateral funiculus (DLF) at thoracic levels 10 to 13. For the third spinal cord, an sMEA electrode pair stimulated the ventrolateral funiculus (VLF) at thoracic level 12. Eight stimulus trials were conducted for each electrode type at a given site on the spinal cord surface. Evoked responses to spinal cord stimulation were recorded at vL2 and vL5 [62] (Figure 37) and analyzed using Clampfit (Molecular Systems) and customized Matlab programs (Mathworks). The strengths of evoked responses (Figures 37b and 37d) were quantified by integrating the rectified response signal for 60 ms post-stimulus artifact (Figures 37a and 37c, yellow boxes) and subtracting from that value a rectified, pre-stimulus baseline value of equal duration.

5.2.8.2   Results

Our preliminary comparisons of the sMEA vs. rigid tungsten microelectrode demonstrate that the sMEA is similar to rigid tungsten microelectrodes in its ability to evoke ventral

85

Dorsolateral funiculus stimulation: Rigid Electrode vs. MEA (n=2)

(a) Time-distributed response traces

(b) Area under rectified responses, baseline-subtracted

Ventrolateral funiculus stimulation: Rigid Electrode vs. MEA (n=1)

(c) Time-distributed response traces

(d) Area under rectified responses, baseline-subtracted
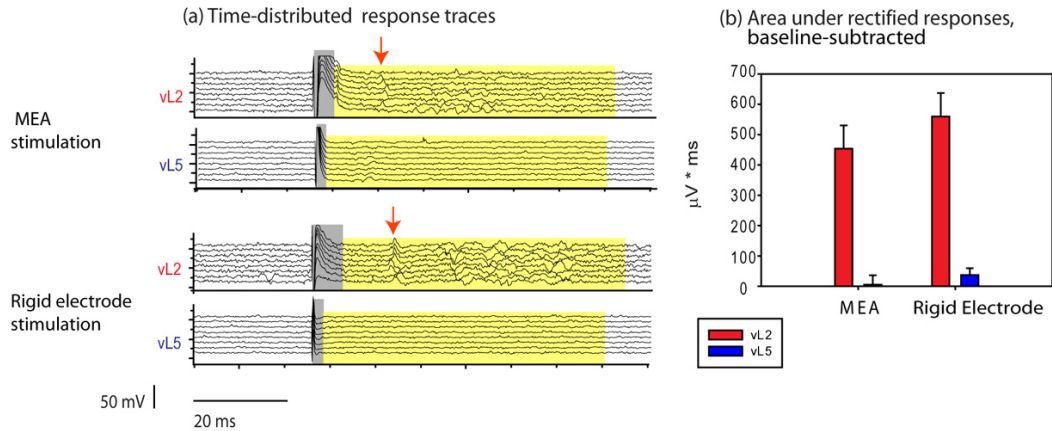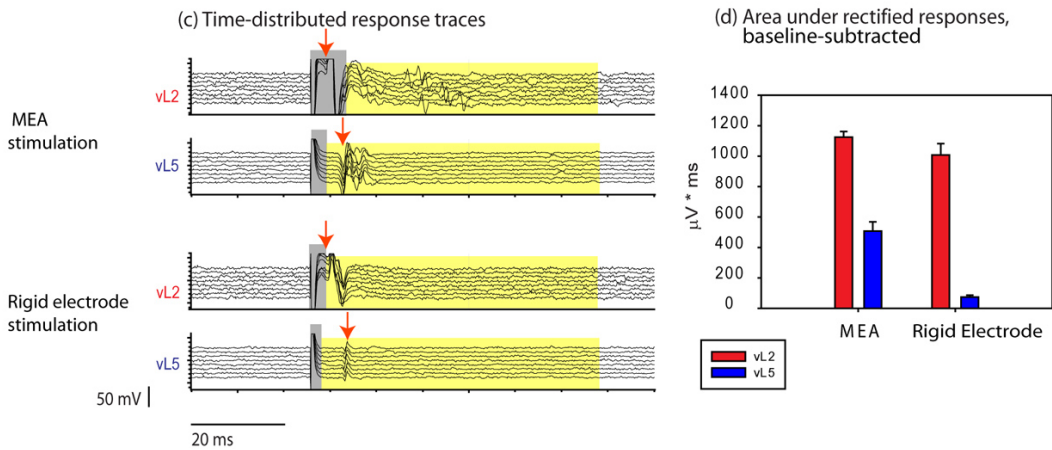
Figure 37: Ventral root responses to surface stimulation of the spinal cord, rigid electrode *vs.* sMEA. A pair of sMEA electrodes (bipolar configuration) and a rigid bipolar tungsten electrode were used to stimulate the spinal cord at surface sites on thoracic level 12 (T12) dorsolateral funiculus (DLF) and ventrolateral funiculus (VLF) (n = 3 cords). A microscope grid eyepiece was used to measure and replicate surface positional coordinates across electrode types. Shown are ventral root L2 (vL2) and ventral root L5 (vL5) responses to sMEA and rigid electrode stimulation at T12 DLF (Figure 37a, data from 1 of 2 cords shown) and T12 VLF (Figure 37c). Eight stimulus trials were conducted per electrode type; these response traces are shown time-distributed. The strength of evoked responses was quantified by integrating the rectified response signal (post stimulus artifact) and subtracting from that value a rectified, pre-stimulus baseline of equal duration (60 ms; Figures 37b and 37d). Standard error bars are shown. Time windows during which stimulus artifact was observed (indicated by gray boxes) were not included in the time range over which strengths of response were measured (yellow boxes). Initial ventral root responses to stimuli can be observed within and after the stimulus artifact (as indicated by arrows), which indicates that stimulus artifact presents a limitation to the accuracy of the strength-of-response calculations. Ventral root L2 (vL2) responses to DLF stimulation were similar in strength for both electrodes, and vL5 responses were similarly small or undetectable using both electrode types (Figure 37b). For VLF stimulation, the pattern of vL2 and vL5 responses was similar across electrode types, with larger responses evoked at L2 (Figure 37d). At the T12 VLF, stronger responses were evoked on both vL2 and vL5 for sMEA stimulation *vs.* rigid electrode stimulation.

root outputs via spinal cord surface stimulation. When placed on T12 DLF (n = 2), the sMEA and rigid tungsten microelectrode evoked vL2 responses with similar strengths (data for one of two spinal cords shown in Figures 37a and 37b). Also similarly, both electrode types evoked little to no response at vL5. The sMEA, when placed at T12 VLF (n = 1), evoked ventral root vL2 and vL5 responses with similar shape and timing characteristics as responses evoked by the rigid tungsten microelectrode (Figure 37c, indicated by arrows). However, the strength of evoked vL2 and vL5 responses was greater for the sMEA than for the rigid tungsten microelectrode (Figure 37d). Together, these results from stimulating with the sMEA and rigid tungsten microelectrode at these two physiologically-relevant spinal cord sites [58, 86, 26, 39, 57, 8] demonstrate that the sMEA is capable of eliciting motor outputs in a similar manner to traditional rigid electrodes, and confirm the suitability of the sMEA for use in future surface stimulation.

5.3   Summary

In this chapter, I summarized the technological strengths of our integrated technology platform for PDMS-based sMEAs. *In vitro* and *in vivo* experimentations were performed to evaluate the biocompatibility, surface conformability, and surface recording/stimulation capabilities of example sMEAs, with a focus on epimysial applications. These results, though not exclusive and thorough, enlighten the promises of this PDMS-based sMEA technology platform for numerous neural interfacing applications.

CHAPTER VI

APPLICATION TO A VOCAL CORD PROSTHESIS

In this chapter, we endeavor to apply our PDMS-based sMEA technology to the development of a vocal cord prosthesis that utilizes simultaneous epimysial recording and stimulation.

6.1 The Problem—Unilateral Vocal Cord Paralysis

The vocal cords (or folds) are two elastic bands of muscle tissue located in the larynx (voice box) directly above the trachea (windpipe). The vocal cords produce voice when air held in the lungs is released and passed through the closed vocal cords, causing them to vibrate. When a person is not speaking, the vocal cords remain apart to allow the person to breathe. Vocal cord paralysis is a common voice disorder found in the practice of Otularyngology when one or both of the vocal cords do not open or close properly. Consisting of unilateral and bilateral vocal cord paralysis, vocal cord paralyses can affect speaking, breathing, and swallowing, and symptoms can range from mild to life threatening. Unilateral vocal cord paralysis (UVCP) (Figure 38) is more common than bilateral vocal cord paralysis (BVCP) due to anatomical configurations (Figure 39, *the left vocal cord is affected twice as often as the right*), and it is the immobility of one vocal cord because of a dysfunction of the recurrent laryngeal or vagus nerve innervating the larynx. It causes a characteristic breathy voice often accompanied by swallowing disabilty, a weak cough, and the sensation of shortness of breath. Because the paralyzed cord or cords remain open, leaving the airway passage and the lungs unprotected, food or liquids can slip into the trachea and lungs. Various techniques have been proposed for managing vocal cord paralysis, including voice therapy, laryngeal framework surgery, reinnervation surgery, and injection laryngoplasty [133, 27, 22, 100]. (The texts in this paragraph are primarily based on internet resources.)
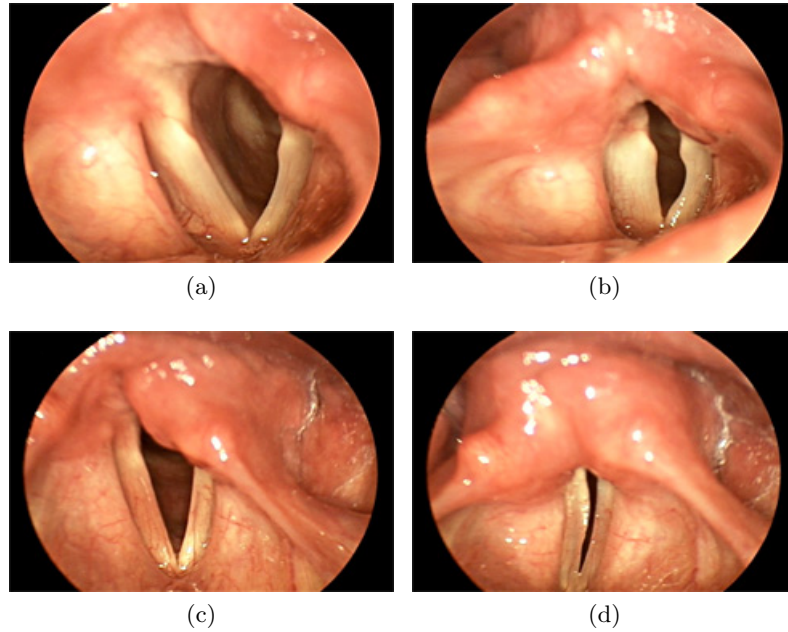
Figure 38: Unilateral vocal cord paralysis [129]. (a) The vocal cord on the right of this photo is paralyzed after a thyroid operation. (b) An effort to make voice moves the other cord to the midline, but a substantial gap remains between the two. This makes for a soft, breathy voice. (c) The vocal cord on the right of the photo is paralyzed. (d) Even with extreme effort, the opposite vocal cord cannot meet its partner.
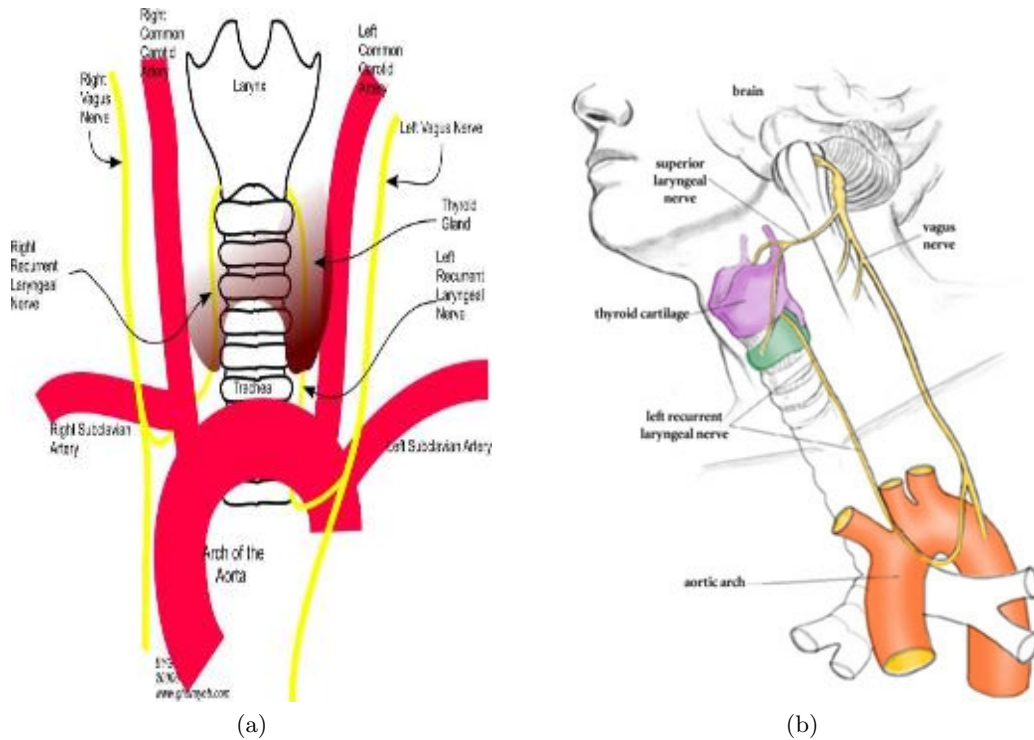
Figure 39: Nerve supply for the larynx (images acquired from internet).

6.1.1 Anatomy

6.1.1.1 The Vagus/Recurrent Laryngeal Nerve [16]

The recurrent laryngeal nerve (Figure 39) is responsible for both abduction and adduction of the vocal cord. It originates from the vagus nerve, which originates from the brainstem (nucleus ambiguous in the medulla) and travels along the carotid sheath (with the jugular vein and internal carotid artery). The left vagus nerve gives rise to the left recurrent laryngeal nerve as the vagus crosses the arch of the aorta. The left recurrent laryngeal nerve then loops under the ligamentum arteriosum and travels cephalad in the tracheoesophageal groove until it penetrates the larynx to innervate the intrinsic muscles of the larynx. The right vagus nerve delivers the recurrent laryngeal nerve branch at the level of the subclavian artery. The right recurrent laryngeal nerve loops around the subclavian artery and proceeds cephalad to the larynx. The recurrent laryngeal nerve, just prior to its entrance into the larynx, runs deep to the inferior cornu of the thyroid cartilage. For a short section, the nerve is in a space between the cricoid and thyroid cartilage. This is thought to be the space where the nerve is vulnerable to compression from the cuff on an endotracheal tube that is either overinflated or positioned too far cephalad. Because of the circuitous nature of the recurrent laryngeal nerve, multiple disease processes and operative procedures put these important nerves at risk, often resulting in vocal cord paralysis.

6.1.1.2 The Laryngeal Skeleton [133]

The major cartilages of the larynx are the thyroid, cricoid, arytenoid, and epiglottic. The upper border of the thyroid cartilage is united with the hyoid bone above by the thyrohyoid membrane. Each side of the thyrohyoid membrane has an opening posterulaterally to allow the internal branch of the superior laryngeal nerve and superior laryngeal artery to enter the larynx. The inferior horns of the thyroid cartilage articulates below with the cricoid cartilage by synovial joints. The cricoid cartilage anteriorly is united above through its arch with the thyroid cartilage by the cricothyroid ligament. Below, the cricoid connects with the trachea by the cricotracheal ligament. Articulating with the upper lateral borders of the cricoid laminae are the arytenoid cartilages. Each arytenoid resembles a 3-D pyramid.

90
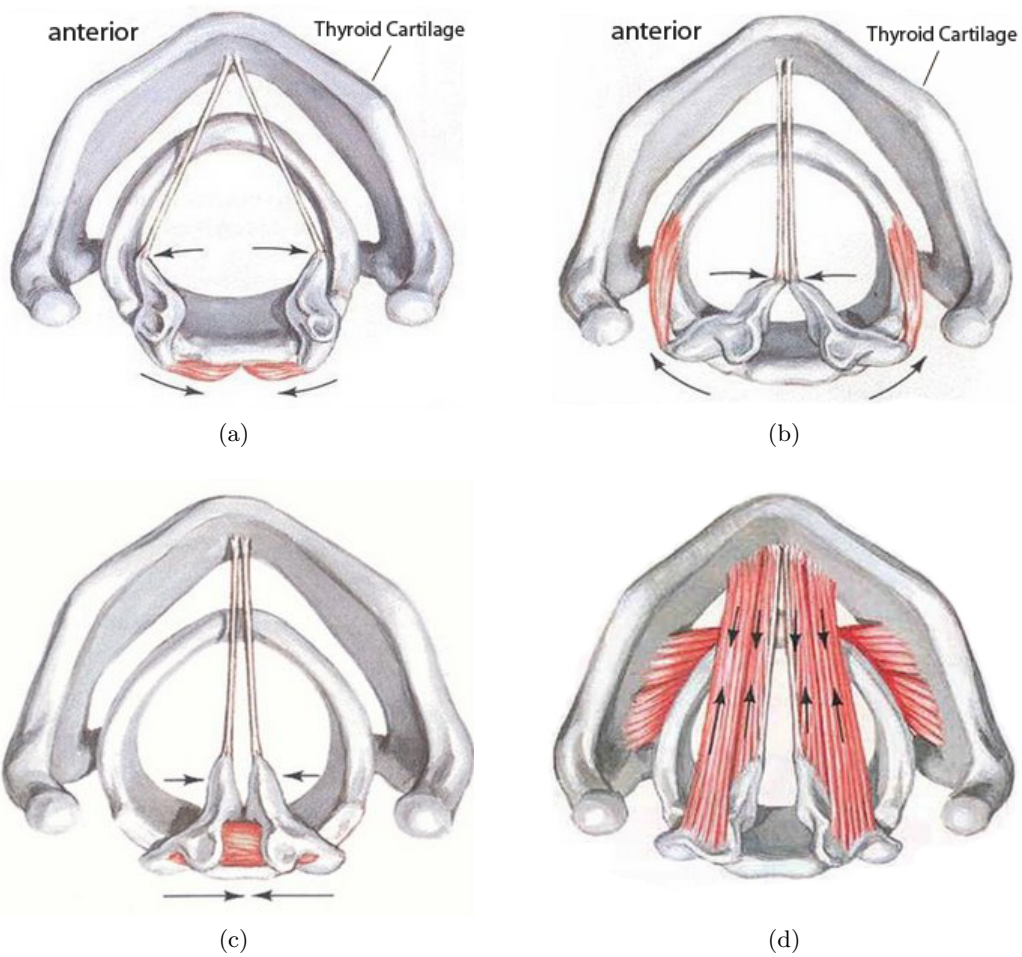
Figure 40: Muscles responsible for vocal cords abduction and adduction [75]. (a) Posterior cricoarytenoid muscle: outward rotation of the arytenoid (abduction of the vocal cord). (b) Lateral cricoarytenoid muscle: inward rotaion of the arytenoid (adduction of the vocal cord). (c) Inter arytenoid muscle: transverse, oblique & aryepiglotic parts: (adduction & close inlet). (d) Thyroarytenoid muscle: proper, vocalis & fan: (adduction, tension & open inlet).

The base of the pyramid is another synovial joint in which the arytenoid cartilage can slide laterally and medially, forward and backward, or rotate upon the cricoid cartilage. Laterally, there is a short, blunt muscular process and anteriorly, there is a thinner vocal process, to which the vocal cords are attached.

6.1.1.3 The Laryngeal Musculature [133]

The intrinsic muscles of the larynx, all of which are innervated by the recurrent laryngeal nerve, include the:

Posterior cricoarytenoid (PCA) the ONLY abductor of the vocal cords. Functions to open the glottis by rotary motion on the arytenoid cartilages (Figure 40a). Also tenses cords during phonation.

Lateral cricoarytenoid (LCA) functions to close glottis by rotating arytenoids medially (Figure 40b).

Transverse arytenoid only unpaired muscle of the larynx. Functions to approximate bodies of arytenoids closing posterior aspect of glottis (Figure 40c).

Oblique arytenoid this muscle plus action of transverse arytenoid function to close laryngeal introitus during swallowing (Figure 40c).

Thyroarytenoid (TA) very broad muscle, usually divided into three parts (Figure 40d).:

Thyroarytenoideus internus (vocalis) - adductor and major tensor of free edge of vocal cord.

Thyroarytenoideus externus - major adductor of vocal cord

Thyroepiglotticus - shortens vocal ligaments

The cricothyroid muscle is considered to be an extrinsic muscle of the larynx because it is innervated by the external branch of the superior laryngeal nerve. It functions to increase tension in the vocal cords, especially at the upper range of pitch or loudness.

6.1.2 Causes

The commonest cause of UVCP remains controversial. From the results of nine studies, dating from 1974–1991, it appears that malignancy (Table 5) is the most common cause of UVCP [133]. Nerve injury during a number of common surgeries (Table 6), often touted as the commonest cause by some authors, comes in second according to the combined results of these studies. Idiopathic causes are next in frequency. UVCP far outnumbers BVCP.

6.1.3 Symptoms and Signs

Normally the vocal cords are able to open and close symmetrically. With these two motions, they accomplish three tasks: open to allow breathing, close to prevent food from entering the trachea (windpipe) when one swallows, and vibrate to produce voice with air flowing from the lungs. In UVCP, the larynx is unable to completely close. Thus breathing is usually normal, since it depends on the vocal cords being able to open. However, people

Table 5: Medical conditions that can result in vocal cord paralysis [105]

Thyroid cancer
Tuberculosis, Sarcoid or anything that causes lymph nodes to enlarge in the chest
Stroke
Various neurologic diseases, such as Charcot-Marie-Tooth, Shy-Drager, and Multisystem atrophy

Table 6: Operations that can result in vocal cord paralysis [105]

Thyroidectomy
Thymectomy
Carotid endarterectomy
Lung operations, particularly on the left side
Heart operations, especially aortic valve replacement or repair
Repair of thoracic aortic aneurysm
Anterior cervical diskectomy
Mediastinoscopy/ mediastinal lymph node biopsy
Closure of patent ductus arteriosus
Brain surgery, especially at the base of the brain or brainstem

may find that they occasionally cough or choke when swallowing, particularly when swallowing liquids, because the resultant glottal incompetence can lead to aspiration. The most noticeable symptom is the dramatic voice change (dysphonia) due to a weak or absent vocal cord vibration: the voice become hoarse, breathy and weak. Speaking at loud volume or over background noise becomes very challenging and effortful. Patients get winded when speaking, because so much air is needed to make the vocal cords vibrate. Significant muscle tension is often seen in the larynx as a compensatory mechanism for the glottal gap. Patients with UVCP often describe pain in the throat or neck after voice use, which is likely due to the excessive muscle tension. (The texts in this paragraph are primarily based on internet resources.)

6.1.4 Current Treatment

In UVCP, the goal of treatment is to improve vocal cord closure, because all of the symptoms caused by vocal cord paralysis are due to incomplete vocal cord closure. Current treatment is based on repositioning the immobile vocal cord closer to its partner and the treatment is directed at improving vocal cord function through voice therapy, augmentation, medialization, or reinnervation. Voice therapy will need the patient to work with a speech-language pathologist on pitch alteration, increasing breath support and loudness, and finding the correct position for optimal voicing (such as turning the head to one side or manipulating the thyroid cartilage). Augmentation involves injecting pulytetrafluoroethylene (Teflon), collagen, micronized dermis, or autologous fat into the paralyzed cord to increase its size, thus bringing the cords closer together to improve the voice and prevent aspiration [133, 27, 22]. Medialization (Figure 41) is shifting the vocal cord toward the midline by inserting an adjustable spacer laterally to the affected cord. This can be done with a local anesthetic, allowing the position of the spacer to be tuned to the patient's voice. Unlike augmentation with plasticized particles, which permanently fixes the cord, the spacer is both adjustable and removable. Reinnervation is performed in the form of nerve-muscle transfer [133]. Reinnervation is surgery aimed at providing an alternate nerve supply to the vocal cord. It is not expected that this will cause the vocal cord to move again,
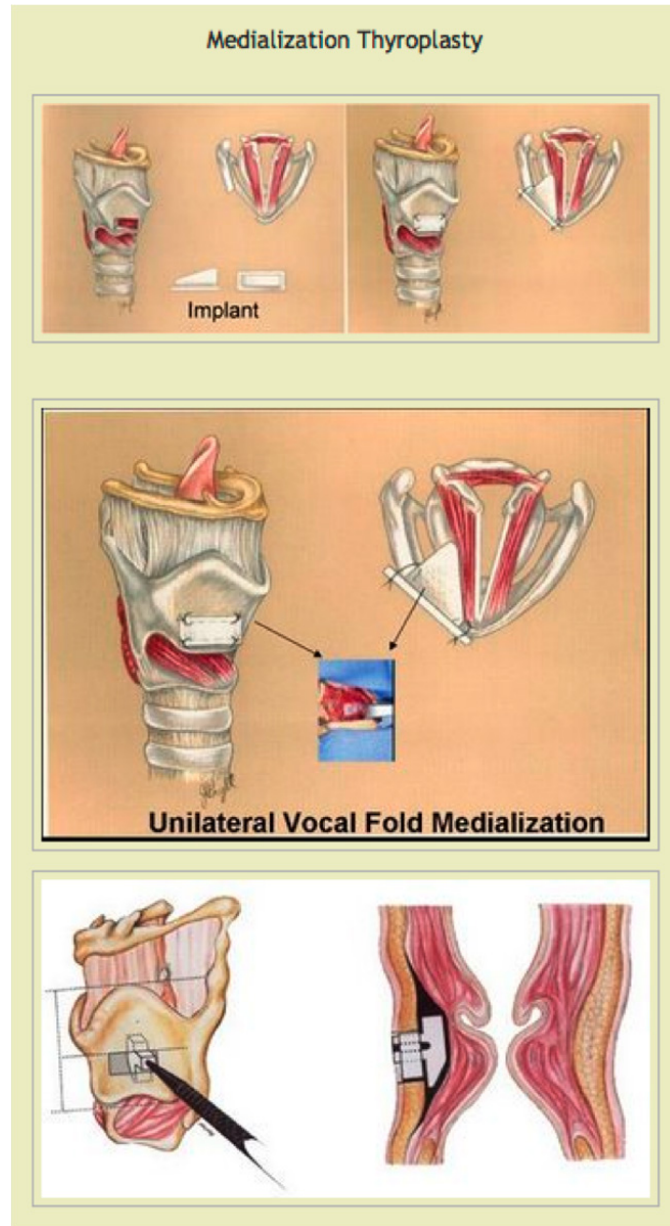
Figure 41: The medialization thyroplasty (image acquired from internet). The implant is used to bring the paralyzed vocal cord close to the midline, so that when the functional cord closes, a complete closure can be made.

but rather, that it will restore tone and bulk to a flaccid (limp) vocal cord. Observations have suggested that this may be enough to achieve a good voice result. Reinnervation is currently an investigational therapy, and is not used routinely in most centers. In most cases of UVCP, it is possible to restore near-normal conversation voice, even though, so far, it has not been possible to restore motion to an immobile vocal cord. Recent studies show

95
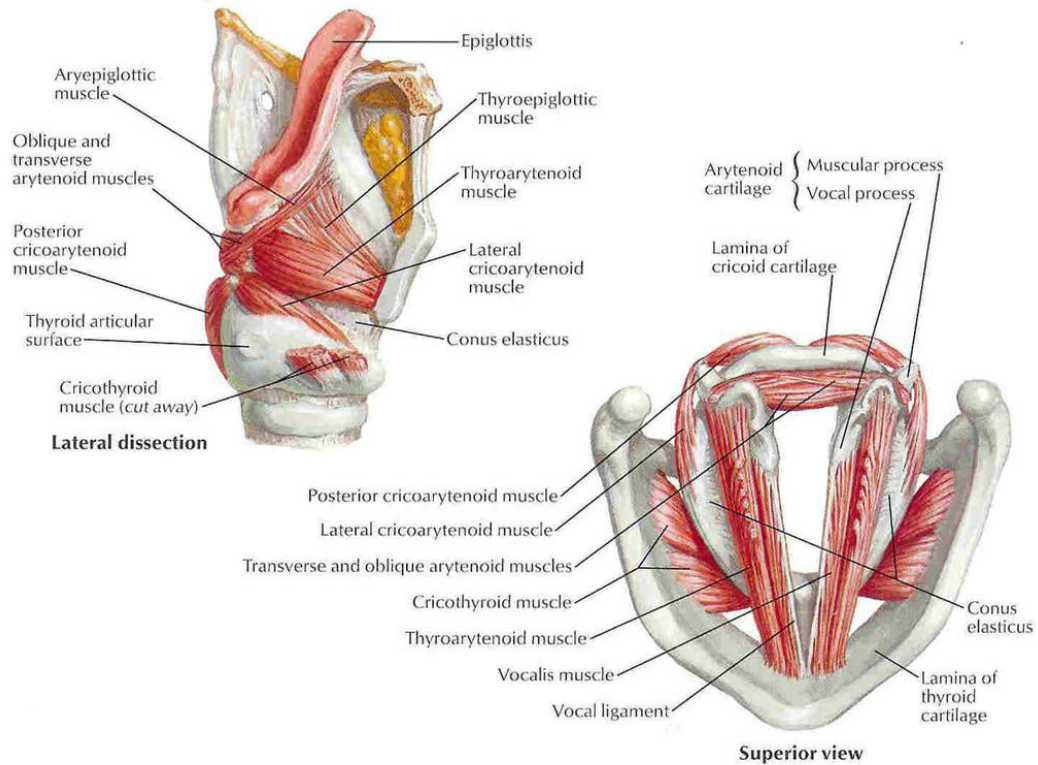
Figure 42: Lateral and superior views of the laryngeal musculature [75]. The thyroarytenoid/lateral cricoarytenoid complex (TA/LCA) is selected as the target subset of muscles for this prosthesis, because: 1) UVCP results in the inability of closing the paralyzed vocal cord, 2) this subset is responsible for adduction of the vocal cord, and 3) the muscles in this subset are easy to access to both during surgery and by the implanted device.

that another feasible approach to laryngeal rehabilitation may be using an electrical stimulation device to activate the reflexes of the paralyzed muscles that open the airway during breathing [100]. (The texts in this paragraph are primarily based on internet resources.)

6.2   The sMEA-Based Vocal Cord Prosthesis

6.2.1   Concept

The vocal cords are composed of twin infoldings of mucous membrane stretched horizontally across the larynx. They vibrate, modulating the flow of air being expelled from the lungs during phonation (wikipedia.org). And correspondingly, their controlling system is composed of two relatively independent groups of nerves and muscles. In the situation of UVCP, the nerve (the vagus and/or recurrent laryngeal nerve) in one group is damaged. Thus, the muscles in that group lose innervation and become paralyzed, even through they

96
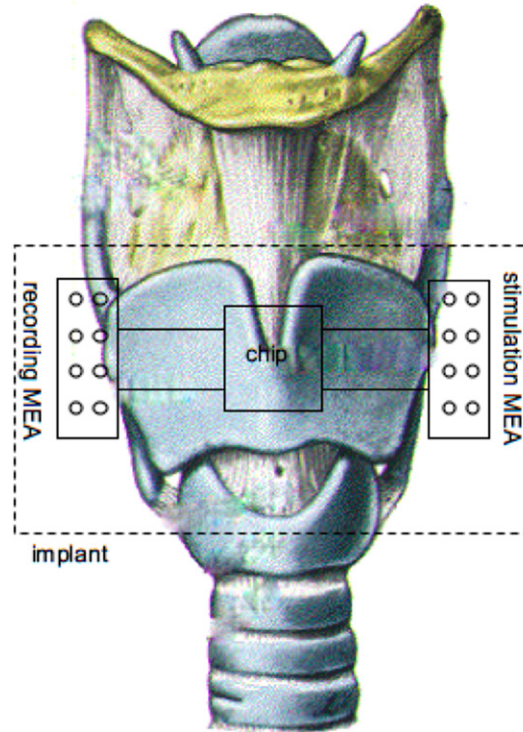
Figure 43: sMEA-based prosthesis for UVCP. The concept of this prosthesis is to epimysially record EMG activities from the functioning side and to copy them to the paralyzed side through epimysial stimulation, so that activities of the two cords can be synchronized. Our PDMS-based sMEA technology facilitates such a prosthesis by providing an integrated epimysial interface, as illustrated in the figure (the background image was acquired from internet).

still retain their functional capability.

Therefore, we propose a bypass prosthetic solution to synchronize a selected subset of vocal cord muscles [the thyroarytenoid/lateral cricoarytenoid complex (TA/LCA, Figure 42), responsible for adduction of the vocal cord (Figures 40b and 40d), since UVCP results in the inability of closing the paralyzed vocal cord], which is critical and may be sufficient in restoring major functions of the paralyzed vocal cord, on the paralyzed side with its counterpartner on the healthy side (Figure 43). This prosthesis uses information extracted from multichannel epimysial recordings on the subset muscles of the healthy side to trigger programmed simultaneous epimysial stimulation on the subset muscles of the paralyzed side, in order to synchronize the activities of the two groups of muscles.

In the following sections, I describe our pilot efforts toward the exploration of this prosthesis concept using *in vitro* and *in vivo* model systems. The technology developed

97

and knowledge gained from such models are expected to be transferable to the prosthesis development.

6.2.2 *In Vitro* Experiment: Frog Muscle Model

First, we developed a simple frog muscle model system (Figure 44b) to investigate the feasibility of the prosthesis concept. The aim is to be able to record epimysially on one muscle and to stimulate epimysially on the other, so that contractions of the two muscles can be synchronized.

6.2.2.1 *Experiment Setup*

A custom-made PCB with eight-channel amplifiers and a microcontroller unit (MCU, C8051F920, Silicon Labs) (Figure 44a) was used in this experiment. The circuit operated with a single power supply of 3 V. The amplifier settings were: gain = 200, lowpass = 1 kHz, and highpass = 1.0 Hz. A simple EMG threshold-detection algorithm ran on the MCU, which automatically monitored a selected recording channel and triggered stimulation upon detection of a muscle contraction event. The circuit had been tested to confirm the designed functionalities before being used in the experiment. Two stimulators (Analog Stimulus Isolator, Model 2200, A-M Systems) were used for stimulation.

Figure 44b shows the frog dual-muscle experiment setup. Gastrocnemius muscles from frog hind legs were dissected with the sciatic nerve attached, fixed at the ankle end, and attached by suture to a force transducer at the knee end, respectively. A PCB-integrated dual-sMEA (Figure 24c) was placed over the two muscles. The sMEA was connected to the PCB (Figure 44a) through a connector on the other end of the wire bundle. The recording reference electrode was placed on another piece of muscle that was in a resting state throughout the experiment. The sciatic nerve of *Muscle 1* was stimulated using a hook bipolar electrode with 100 μs/0.5 mA monophasic current pulses. This nerve stimulation was used to lead the contraction events in this dual-muscle model system. Three-channel EMG signals were recorded on the surface of *Muscle 1*. The signal from one of these channels was selectively digitized by the internal analog-to-digital converter (ADC) of the MCU, and EMG events on this channel were monitored by the algorithm and used to trigger the

98
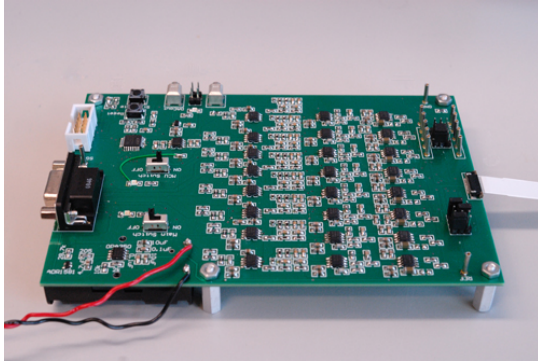
(a)
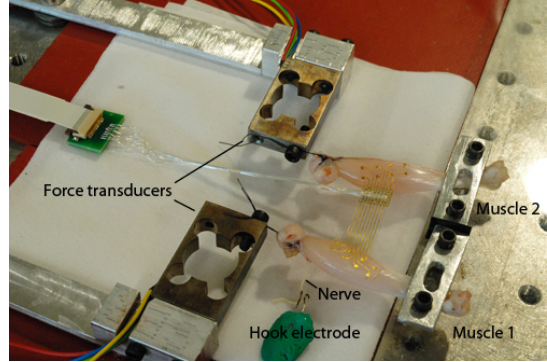
(b)
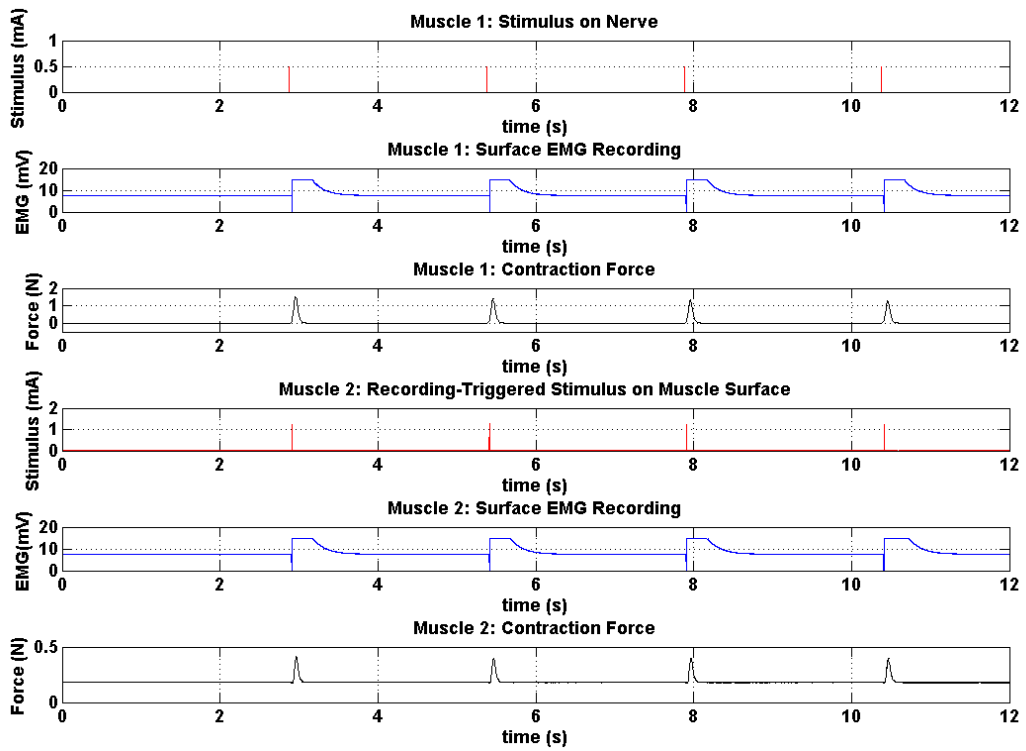
(c)

Figure 44: Experiment setup for muscle synchronization. (a) Custom-made PCB with eight-channel amplifiers and a microcontroller. (b) Experiment setup for muscle synchronization. (c) Data from one trial.

simultaneous surface stimulation on *Muscle 2*. The stimulation trigger signal was sent from the MCU to a digital-to-analog converter (DAC) which drove a stimulator. The output of the DAC was programmed to generate 100 μs wide square voltage pulses with an amplitude ranging between 0 and 2.5 V. The stimulator's bipolar output was routed to two electrodes on the sMEA placed over the surface of *Muscle 2*. Two other electrodes on the sMEA were used for simultaneous surface recording on *Muscle 2*. The contraction forces of both muscles were recorded by the force transducers.

6.2.2.2   Results

Data from one trial of the experiment is shown in Figure 44c. The top three plots correspond to *Muscle 1*, and are stimulus applied on the nerve, one of the three channels of surface EMG recording, and contraction force, respectively. The bottom three plots correspond to *Muscle 2* with the stimulus plot corresponding to the recording-triggered epimysial stimulation. During the experiment, it was observed that, in the situation that the EMG detection and stimulation triggering algorithm was not activated, when the nerve of *Muscle 1* was stimulated, *Muscle 2* did not contract, neither were any EMG or force signals observed from *Muscle 2*. In contrast, when the algorithm was activated, the contraction of *Muscle 2* was synchronized with that of *Muscle 1*, as is shown by the data plots. However, the data also shows that the amplifiers in the recording channels were caused to saturate by the high stimulation artifacts. Moreover, the data indicates that, even with a higher stimulus amplitude of 1.25 mA, surface stimulation on *Muscle 2* induced lower contraction forces than nerve stimulation on *Muscle 1* with a stimulus amplitude of 0.5 mA ($\sim$0.35 N *vs.* $\sim$1.3 N). The efficiency of muscle surface stimulation is also expected to be dependent on the placement of stimulation electrodes, as special sites on a muscle surface, such as those close to the motor point and neuromuscular junction, are known to have a lower stimulation threshold [55].

6.2.3   A Step Further—*In Vivo* Experiment: Dog Implantation

We have also attempted one dog implantation experiment, as shown in Figure 45. We adopted the same surgery procedures as used in the conventional medialization thyroplasty

www.manaraa.com
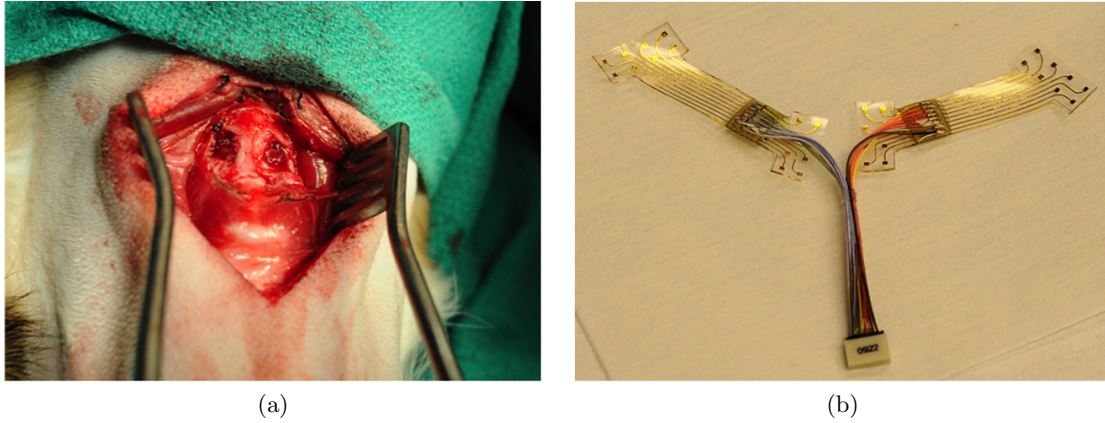
Figure 45: Implantation experiment using a canine animal model to investigate the *in vivo* performance of the proposed prosthesis.

(Figure 41). Two windows were open in the cartilage through which each head of the dual-sMEA (Figure 45b) was inserted under the cartilage to reach to the TA/LCA complex on each side. Unfortunately, no useful data was obtain from this pilot attempt, because blood in the windows caused failure even to acute recording and stimulation. So, we aborted the implantation.

6.3 Summary

We have proposed and preliminarily investigated a prosthesis for UVCP. This prosthesis involves simultaneous multichannel epimysial recording and stimulation using a pair of sMEAs to synchronize the activities of two groups of muscles responsible for vocal cord adduction. *In vitro* and *in vivo* animal models were developed to validate the prosthesis concept. However, the systems we have developed and the knowledge we have gained at this stage are still very limited in tackling this challenging prosthesis. Nonetheless, our pilot investigations on the sMEA-based vocal cord prosthesis have been intriguing and inspiring to future work. With improvements on the implant design, control algorithm development, and surgery performance, we envision encouraging advances on this sMEA-based vocal cord prosthesis in the future.

CHAPTER VII

CONCLUSIONS AND OUTLOOK

7.1 Conclusions

In this thesis, I have developed an integrated technology platform for PDMS-based sMEAs to address the demands for high-resoltion, high-density conformable/stretchable neural interfaces. This technology platform opens the door to numerous promising neural interfacing applications that require conformable device contact with biological tissue surfaces and that require minimal tissue damage that often results from rigid electrodes, e.g., high-resolution retinal prostheses, spinal-cord surface stimulation for prosthetics, electro-corticogram (ECoG)-based brain-computer interfaces (BCIs), etc.

7.1.1 Existing Problems

Although the development efforts on high-density PDMS-based sMEAs in this thesis represent significant advances on stretchable electronics, two aspects are worth attention: fabrication yield and device stretchability.

The development work has been conducted in a research-grade cleanroom environment, where quality control through the fabrication processes was minimal. The yield for fully functional electrode channels on a device is currently in the range of $50 \sim 100\%$ for low-resolution sMEA designs (depending on the packaging schemes: glass integration has a yield above 90%, while FR4-based PCB integration has a yield between $50 \sim 90\%$). The yield for high-resolution, high-density designs is even lower and more sensitive to processing parameter variations and environmental dusts. As a result, fabrication of fully functional, IC-integrated, high-density sMEAs in our current conditions is still challenging and costly. Robust packaging designs, an industry-grade cleanroom environment, and stringent quality controls are necessary to boost the yield, if this sMEA technology is to be put into production.

Our interconnect stretching study showed that the gold interconnects could withstand

longitudinal tensile strains in the range of $1 \sim 2\%$ (see Chapter III). This stretchability is considerably lower compared to that reported of flat traces produced by other groups [70, 130]. This discrepancy may be the result of different micro/nano-scale gold film morphologies deposited with different equipment under different conditions [42]. Another possibility is that our tests did not adequately assess the stretchability of the interconnects. It is possible that the junction between the trace and the contact pad (see Figure 10c) is the site where excess strains would be generated and break the trace first when subject to a strain loading. This would consequently obscure the experimental quantification of the real interconnect stretchability. Therefore, our measurement might have underestimated the interconnect stretchability. Further investigation is needed to determine the stretchability of our sandwiched interconnects more accurately.

7.1.2 Future Works

For any emerging technology, if the early development stage is not accompanied by extensive efforts on thorough evaluation and characterization, its acceptance to the (technical) community and widespread applications would not be possible. Although I have presented some biological evaluations on the technology in this thesis, these preliminary results should be enhanced with more further investigations, and more talented people need to be brought into the work. We are happy to see that efforts toward this direction are starting, as a few collaborations are being actively developed.

While currently our primary interests are in surface interfacing applications, this technology platform is capable of being adapted to the fabrication of (1) PDMS-based penetrating MEAs for applications such as intracortical recording, and (2) PDMS-based microchannel MEAs for applications such as regenerative peripheral nerve interfacing. And indeed, some efforts have also started toward these directions.

For a technology to generate impacts more widely, it is necessary that industry partners are involved to make products of the technology available to the market. We are excited that Axion Biosystems, Inc., a Georgia Tech based startup company, is pushing the commercialization process of this technology platform.

7.1.3 Concluding Remarks

It is my will that this open technology platform will provide neuroscientists with a new tool to study the nervous systems, and provide biomedical engineers and clinicians with a new capability to treat challenging neurological and neuromuscular diseases through novel neural prosthetics.

7.2 Outlook: From Passive Interfacing to Active Integration

While exciting advances in the neural interfacing field have been made toward the development of soft neural interfaces to better match the mechanical impedance of soft tissues and to be able to conform to the complex tissue surface, the present (awkward) neural interfacing technologies are *passive*, i.e., the interface (or implant) and the neural tissue function as two physically isolated systems only with electrical signals as a tie in-between. As a result the functionality and reliability of the implant diminish in a short-time. The concept of an *active* neural interfacing technology is very promising in addressing these present issues. An active neural interface is capable of dynamically remodeling in response to the tissue environment, growing into the tissue and/or guiding growth/regeneration of the tissue (both neural and others) into the interface to form an integrated hybrid tissue system with the desired functionalities. To do so, the active neural interface should have some programmed intelligence and an associated capability of physicochemical transformation. Apparently, the current electronics-based neural interfaces and the materials from which these interfaces are made are absolutely inadequate to meet such a need. The active neural interfaces should be made from biologically related materials and function in the/a same/similar way as/to biological systems. Combinational efforts from the fields of biomaterials, drug delivery, synthetic biology, regenerative medicine, and micro/nano-fabrication would potentially provide a promising route to approaching this active neural interface concept, which would potentially revolutionize the implantable medical device field in that to facilitate a better integration of the implant with the surrounding tissues to form a hybrid functional system.

APPENDIX A

A COMPARISON OF PDMS WITH POLYIMIDE AND PARALYNE AS THE SUBSTRATE MATERIAL FOR NEURAL INTERFACES: MECHANICS ANALYSES

It is believed and supported by biological experiments that softer neural implants are better than stiffer ones, however, the physical principles underlying have not been systematically explored. So, in this appendix, I use mechanics analyses to compare the common substrate materials (i.e., parylene, polyimide and PDMS) used in flexible MEA fabrications. The conclusion supports the claim that the more compliant PDMS outperforms the other two stiffer polymers as the substrate material for neural surface interfaces.

A.1   Introduction

Flexible thin-film MEAs as neural interfaces are fabricated primarily using a polymer substrate such as parylene [109], polyimide [112, 40, 101, 119, 17, 74, 63], and PDMS [85, 71, 116, 93]. These MEAs have a common sandwiched structure with thin-film noble metal conductors embedded between two polymer layers—the substrate and encapsulation (Figure 46a). With Young's Modulus of ~ 4.5 GPa [109], ~ 2.8 GPa [112], and ~ 1.0 MPa [93] (Table 7), respectively, these polymers and the resulted MEAs exhibit different level of mechanical flexibility. This appendix sets out to prove that for neural interfacing applications, the softer PDMS serves as a better substrate and encapsulation material. Mechanics analyses are conducted to evaluate the mechanical performances and the mechanical impacts to the surrounding tissues of an MEA fabricated with the three types of polymer substrates.
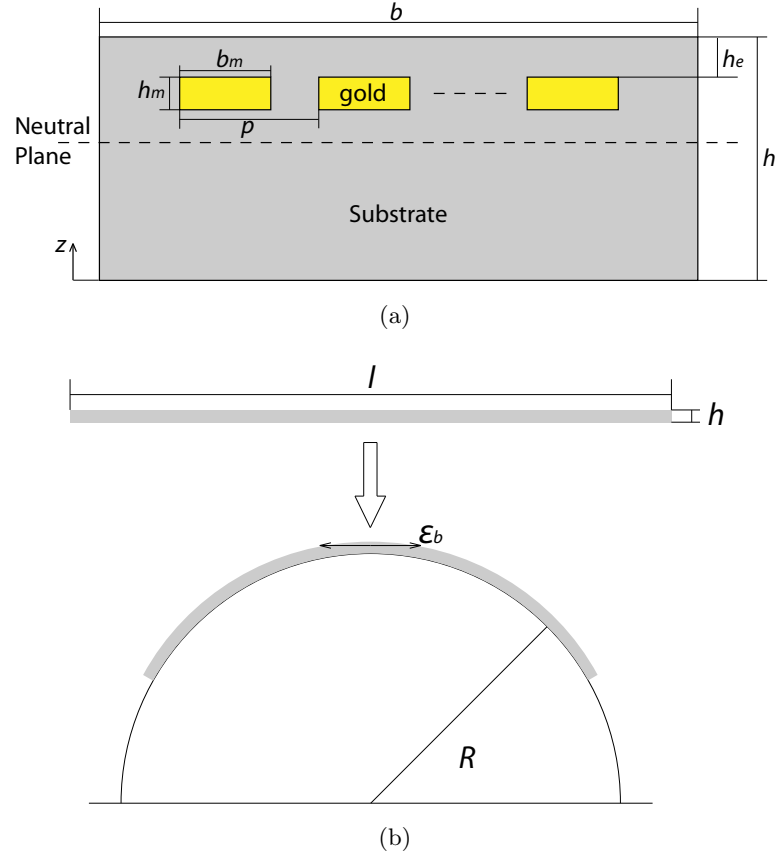
Figure 46: Dimensions of an MEA model used for calculations. (a) The sandwiched structure of the MEA (cross-sectional view). The MEA is placed with its electrodes facing up. (b) The MEA bends/wraps on a cylinder of radius R. b, l, and h are width, length, and thickness of the MEA, respectively. The gold traces are assumed to run along the length direction. These illustrations are adapted from Ref. [63].

Table 7: Properties of materials used for flexible MEAs

Material	Young's Modulus E	Poisson's Ratio ν	Relative Permittivity ε_r	Electrical Resistivity ρ
Parylene	~4.5 GPa	0.4	2.95–3.15	6 x 10^{16} $\Omega \cdot cm$
Polyimide	~2.8 GPa	0.34	3.4	1.5 x 10^{17} $\Omega \cdot cm$
PDMS	~1.0 MPa	0.5	2.3–2.8	1.2 x 10^{14} $\Omega \cdot cm$
Gold	78 GPa	0.44	–	$\sim$ 5 x 10^{-6} $\Omega \cdot cm$ [†]

[†] For gold thin films patterned on glass slides [70].

A.2   Mechanical Performance

A.2.1   Bending Strain—Softer Is Better

For flexible MEAs, the first technical question arising in our minds is how the substrate's stiffness affects the sustainability of the thin-film metal conductors during deformation. While the substrate material can withstand a large amount of mechanical strain before rupture, the metal film usually can only tolerate a small amount of stain (e.g., a few percent). So, MEA designs need to minimize the strain induced in the metal film during deformation. *Bending Strain* is usually used to characterize the strain induced in a flexible film device when it is bent into a cylindrical roll [123] (Figure 46b).

To study how the bending strain in the MEA is affected by the substrate's stiffness, we start our calculations using the MEA model shown in Figure 46a. The problem is formulated such that the device is bent along its length l into a cylindrical roll of radius R (Figure 46b). The bending strain ε_b at a normal coordinate z is

$$\varepsilon_b = \frac{z - z_0}{R} \tag{1}$$

where z_0 is the position of the neutral plane in which $\varepsilon_b = 0$ [123, 128]. In the bending condition in Figure 46b, a point above the neutral plane is subject to tension, while its mirror point with respect to the neutral plane has the same strain value but is subject to compression. Here, we consider the case that the electrodes face upward in Figure 46b, so if the metal layer is above the neutral plane, the metal film is in tension.

Assuming $b = np$, where n is the number of gold traces; and define a fill factor $f = b_m/p$, with $f = 0$ and $f = 1$ corresponding to no embedded gold and an embedded gold sheet, respectively. The neutral plane for the MEA structure shown in Figure 46a is worked out as

$$z_0 = \frac{h}{2} \frac{1 + f(\frac{E_{Au}}{E_{sub}} - 1)\frac{(2h - 2h_e - h_m)h_m}{h^2}}{1 + f(\frac{E_{Au}}{E_{sub}} - 1)\frac{h_m}{h}} \tag{2}$$

where E_{Au} and E_{sub} are the Young's Moduli of gold and the substrate, respectively [63]. Therefore, the tensile strain on the top surface of the gold film is

$$\varepsilon_{b\_gold} = \frac{h}{2R} \frac{1 - \frac{2h_e}{h} + f(\frac{E_{Au}}{E_{sub}} - 1)(\frac{h_m}{h})^2}{1 + f(\frac{E_{Au}}{E_{sub}} - 1)\frac{h_m}{h}} \tag{3}$$

107
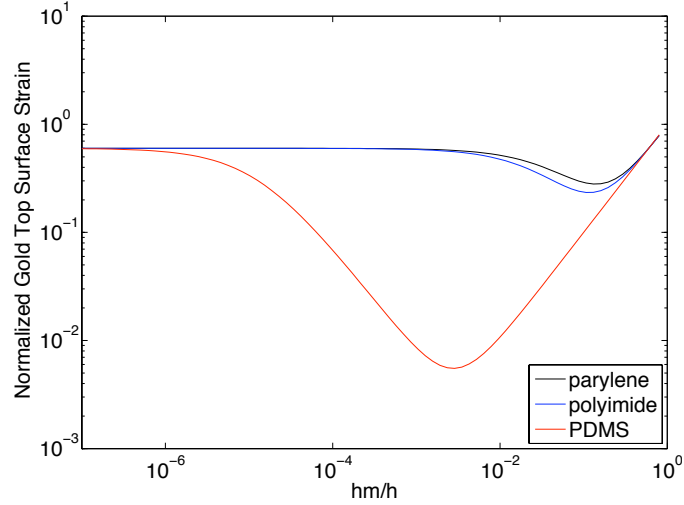
Figure 47: Normalized bending strain $[\varepsilon_{b\_gold}/(\frac{h}{2R})]$ in the gold top surface as a function of h_m/h for parylene, polyimide, and PDMS substrates, respectively. It is assumed that $f = 1$ and $h_e/h = 1/5$.

Figure 47 plots the normalized bending strain in the gold top surface as a function of h_m/h for parylene, polyimide, and PDMS substrates, respectively. It is assumed that the fill factor $f = 1$. It is clear that the softer PDMS substrate can significantly reduce the bending strain in the gold film by as much as a factor of more than 40, as compared to polyimide and parylene substrates. For PDMS MEAs, the minimum bending strain for $h_e = h/5$ is achieved when $h_m/h = 2.9 \times 10^{-3}$.

To minimize the bending strain in the metal film, flexible MEA designs need to position the interconnect layer in or as close as possible to the neutral plane. When the encapsulation uses the same material as the substrate, the interconnect layer lies in the neutral plane if the encapsulation thickness equals to the substrate thickness. In this case, the bending curvature is no longer limited by the rupture strain of the metal material, but by that of the substrate and encapsulation material [123]. Consequently, thin PDMS MEAs with such an optimal design can be bent to extremely small radii without losing its functionality.

In summary, from a perspective of being resistant to metal conductor rupture, PDMS serves as a better substrate and encapsulation material for the fabrication of flexible MEAs.

108
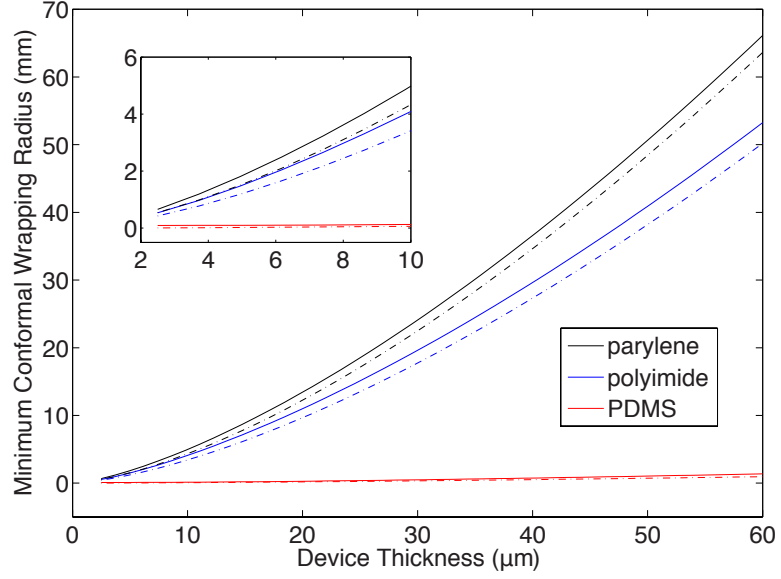
Figure 48: Minimum conformal wrapping radius as a function of the total device thickness for parylene, polyimide, and PDMS substrates, respectively. The parameters used are $h_m = 300$ nm, $h_e = 1/5h$, $f = 1$ (solid lines), $f = 0$ (dashdot lines), $l = b = 1$ cm, and $\gamma_n = 10\ mJ/m^2$ [128]. For the dashdot lines, the colors correspond to the same legend as those of the solid lines. Inset, zooming-in view of the device thickness range of $2 \sim 10\ \mu m$. The units for the axes are same as the main axes.

A.2.2 Conformability—Softer Is Better

Device conformability is characterized by comparing the elastic energy U_b of the MEA under bending to the normal capillary adhesion energy U_{na} between the device and a moist surface (e.g., a muscle surface) [128]. For the MEA of an equivalent bending stiffness $(EI)_{eq}$ wrapping conformally on the moist cylinder surface as shown in Figure 46b, we have

$$U_b \leq U_{na} \tag{4}$$

The elastic energy in the bended MEA is

$$U_b = \frac{(EI)_{eq}l}{2R^2} \tag{5}$$

and the normal adhesion energy between the MEA and the cylinder is

$$U_{na} = \gamma_n lb \tag{6}$$

where γ_n is the normal adhesion energy per unit area between the device and the cylinder [63, 128]. Combining Equations (4) – (6), we have

$$\gamma_n \geq \frac{(EI)_{eq}}{2bR^2} \tag{7}$$

109

The equivalent bending stiffness of the MEA illustrated in Figure 46a is

$$(EI)_{eq} = E_{sub}bh(\frac{1}{3}h^2 - hz_0 + z_0^2) + (E_{Au} - E_{sub})fbh_m[\frac{1}{3}h_m^2 + h_m(h' - z_0) + (h' - z_0)^2] \quad (8)$$

where $h' = h - h_e - h_m$ and z_0 is given in Equation (2) [63].

For simplicity, we study the two extreme cases in which $f = 1$ and $f = 0$. Figure 48 plots the minimum conformal wrapping radius as a function of the total device thickness for each substrates, respectively. Clearly, reducing the substrate material's stiffness and the device's thickness makes the device more conformal, and the PDMS-based device is highly conformal across all thicknesses. The effect of the fill factor f is small. From Equations (7) and (8), to conformally wrap around a cylinder of radius 0.75 mm (the radius of the rat's sciatic nerve), a PDMS-based MEA needs to be thinner than 40.2 μm , whereas a parylene-based MEA needs to be thinner than 2.7 μm and a polyimide-based MEA needs to be thinner than 3.1 μm. Since parylene and polyimide films of a few micrometers thick are very delicate to handle, a PDMS-based MEA, which is more than one order of magnitude thicker but has a similar level of conformability, provides obvious benefits for handling during both fabrication and application.

In summary, from a perspective of forming an intimate contact to the soft tissue surface, the more compliant PDMS serves as a better MEA substrate material that provides an excellent conformability to moist soft tissue surface for electrically interfacing to these tissues, as compared to the two other commonly used substrate materials, parylene and polyimide.

A.2.3 Stretching Rupture Strain

Freestanding metal thin films usually rupture at a strain of ~1% [79], smaller than their bulk counterpart. However, when the metal film is supported by a polymer substrate with good interfacial adhesion, the rupture strain can exceed a few tens of percent [122, 80, 73]. Freestanding metal films rupture through strain localization which causes necking and subsequent rupture of the metal film at a single neck. Given the small thickness-to-length ratio of the metal film, the local elongation of length comparable to the film thickness at the single neck contributes little to the overall rupture strain [78, 122, 79, 80]. The

existence of a polymer substrate suppresses the formation of a single neck by constraining the local elongation of the metal film and thus delocalizing the strain in the film [77, 122, 80]. The high stretchability of the polymer-supported metal film is facilitated by the formation of a percolating network [122, 69], and the polymer substrate acts to stabilize such a network from rupture [79]. As a result, the strains for the microcracks to fully develop and coalesce can be much higher than the strains that initiate the microcracks. Simulation and experimentation have revealed that good interfacial bonding is critical for the yield of a high rupture strain [77, 122].

When the stiffness of the substrate is considered, finite element modeling suggests that the stiffer the substrate, the higher density the induced microcracks in the percolating network, and the larger the rupture strain [78, 79]. A substrate that is too compliant is not good at suppressing strain localization in the metal film. Thus, gold interconnects patterned on parylene and polyimide substrates could be stretched to a higher rupture strain than those patterned on a PDMS substrate. However, in contrast to the elastic deformation of PDMS, parylene and polyimide undergo plastic deformation under strain loadings and thus cannot restore to their initial state once relaxed. Furthermore, to reach to a certain strain, stiffer substrates require a larger force [79], whereas in neural interfacing applications, such a large force is neither possible nor desirable. With PDMS as the substrate, a rupture strain of 23% for gold interconnects was demonstrated [73]. Such a level of stretchability seems to be sufficient for most neural and muscular interfacing applications.

In summary, stiffer substrates like parylene and polyimide lead to higher rupture strain of the bonded metal interconnects; however, they are not suitable for stretchable applications because of their inherent plastic nature, and the much higher force required to stretch the stiffer device is not available nor desired in neural interfacing applications. PDMS-based MEAs, though offering a relatively lower interconnect stretchability, suffice the stretchable functionality as needed in most neural interfacing applications.
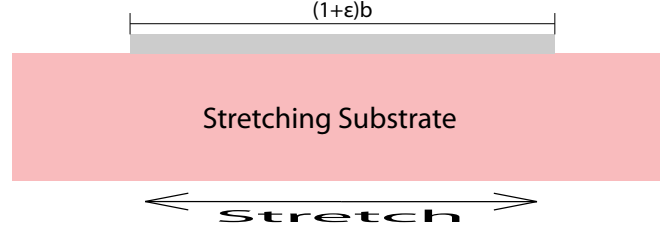
Figure 49: An MEA is driven to stretch by the stretching substrate.

A.2.4   Conformal Stretchability—Softer is Better

When the MEA is applied on a soft tissue surface, e.g. wrapping on a muscle surface in epimysial applications, the MEA is driven to stretch by the interfacial shear forces, as the tissue stretches. The strength of such shear forces depends on the moisture level of the tissue surface, and usually is not very high, particularly in implantation situations where the tissue surface is wetted by physiological fluids. In Section A.2.2, we study the relationship between the MEA's bending stiffness $(EI)_{eq}$ and the normal interfacial adhesion strength γ_n in determining the device's wrapping state. A similar relationship exists between the MEA's tension stiffness $(Eh)_{eq}$ and the tangential interfacial adhesion strength γ_t in determining the device's conformal stretchability (i.e., no relative displacement is initiated between the MEA and the stretching substrate). The two energies under consideration in the stretched state in Figure 49 are the elastic energy U_t in the stretched MEA and the tangential adhesion energy U_{ta} between the MEA and stretching substrate. Assume uniaxially stretching along the width direction, we have

$$U_t = \frac{1}{2}(Eh)_{eq}l\varepsilon^2 \tag{9}$$

$$U_{ta} = \gamma_t l b \tag{10}$$

where ε is the overall tensile strain transferred to the device, and γ_t is the tangential adhesion energy per unit area between the device and the stretching substrate.

The equivalent tension stiffness of the device illustrated in Figure 46a is

$$(Eh)_{eq} = bh\overline{E}_{sub}\frac{1 + (\frac{\overline{E}_{Au}}{\overline{E}_{sub}} - 1)\frac{h_m}{h}}{1 + (1-f)(\frac{\overline{E}_{Au}}{\overline{E}_{sub}} - 1)\frac{h_m}{h}} \tag{11}$$

where $\overline{E}_{sub} = \frac{E_{sub}}{1-\nu_{sub}^2}$ and $\overline{E}_{Au} = \frac{E_{Au}}{1-\nu_{Au}^2}$ are the plane-strain modulus of the substrate and

112
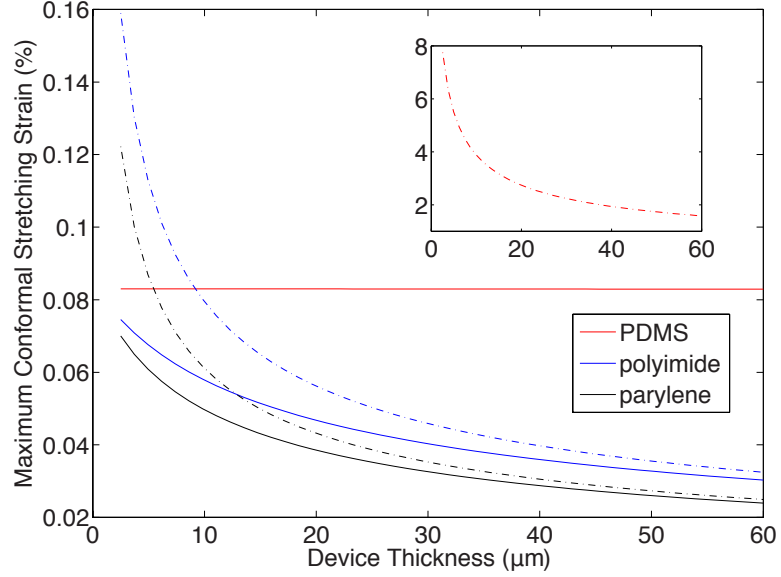
Figure 50: Maximum conformal stretching strain as a function of the total device thickness for a substrate material of parylene, polyimide, and PDMS, respectively. Parameters used are $\gamma_t = \gamma_n = 10\ mJ/m^2$, $f = 1$ (solid lines), $f = 0$ (dashdot lines), $h_m = 300$ nm, $b = l = 1$ cm. For the dashdot lines, the colors correspond to the same legend as those of the solid lines. The inset plots the strain for the PDMS film for $f = 0$. The units for the axes are same as the main axes.

gold, respectively; ν_{sub} and ν_{Au} are the Poisson's ratio as listed in Table 7.

For conformal stretching, we have

$$U_t \leq U_{ta} \tag{12}$$

This gives

$$\gamma_t \geq \frac{(Eh)_{eq}\varepsilon^2}{2b} \tag{13}$$

The exact value of γ_t on a moist surface is currently unknown. To get an impression on how the substrate stiffness affects the MEA's conformal stretchability, we assume $\gamma_t = \gamma_n$ $= 10\ mJ/m^2$ and investigate the two extreme cases of $f = 1$ and $f = 0$. Figure 50 plots the maximum conformal stretching strain as a function of the total MEA thickness for a substrate material of parylene, polyimide, and PDMS, respectively. It is seen that, with γ_t $= 10\ mJ/m^2$, the conformal stretching can only be sustained at very small strains. Thus, in applications like epimysial interfacing, the relative displacement between the device and the tissue is inevitable. Obviously, thinner and softer substrates do facilitate conformal stretching, and for $f = 1$, the conformal stretchability of the PDMS-based device is uniform
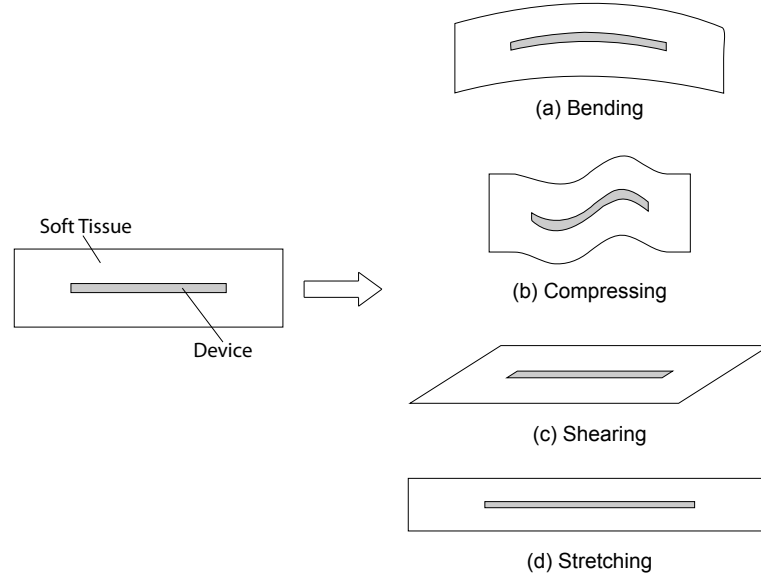
Figure 51: Possible deformation modes of an MEA in the body (cross-sectional view).

across the thicknesses. Furthermore, it is clear that incorporating the gold film reduces the maximum conformal stretching strain. The effect is more prominent for the PDMS substrate. Relative displacements between the MEA and the stretching substrate are undesired, because (1) motion artifacts can contaminate the electrical recording, and (2) the spatial resolution of the MEA is compromised by motion "blurring". Therefore, PDMS significantly excels parylene and polyimide as the MEA substrate material when the gold film fill factor f is small.

To summarize, conformal stretchability is important to applications, such as epimysial interfacing, where the soft tissue interfaced stretches. Although under the physiological moist condition, relative displacement between the MEA and the tissue surface seems to be unavoidable, using a thinner and softer device substrate material and limiting the interconnect fill factor enhace the device's conformal stretchability, and thus minimizing motion artifacts and improving the spatial resolution. The softer substrate material, PDMS, greatly facilitates such an effort.

A.3   Biological Performance—Softer is Better

When an MEA is implanted, it is usually surrounded by soft tissues. During body movements, the soft tissues may deform and the device thus acts to impede these deformations.

114
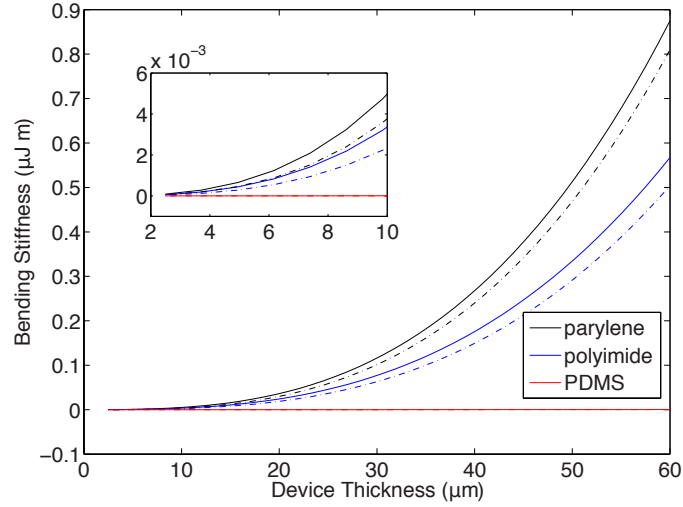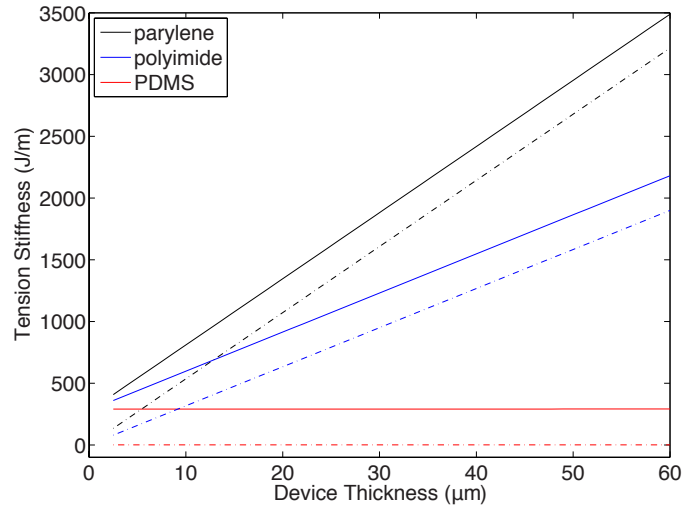
Figure 52: Bending and tension stiffnesses as a function of device thickness for different substrate materials. The parameters used are $h_m = 300$ nm, $h_e = 1/5h$, $f = 1$ (solid lines), $f = 0$ (dashdot lines), and $l = b = 1$ cm. For the dashdot lines, the colors correspond to the same legend as those of the solid lines. (a) The bending stiffness curves. The inset plots the thickness range of $2 \sim 10 \ \mu m$. The units for the axes are same as the main axes. (b)The tension stiffness curves.

The device and the tissue interact with each other by generating stresses. These stresses, if large and/or prolonged, harm the tissues and the implant. It is reported that micromotions between the implanted silicon-based MEAs and surrounding tissues are one major factor that leads to damage to the soft tissue and dysfunction of the implant in the long run [66]. It is also reported that inflammation at the implant site is reduced by using polyimide-based probes as compared to using silicon-based ones [112].

115

Figure 51 illustrates four types of deformations that an implanted MEA may experience in the body. In the bending and compressing deformations, the device is bent; in the shearing deformation, the device may bend and stretch at different sites; and in the stretching deformation, the device stretching along with the surrounding tissues (assuming a sufficient tangential adhesion energy U_{ta}, , e.g., the adhesion is reinforced by suturing the device to the tissue). Thus, the stress level induced in the soft tissues is directly correlated to the bending stiffness of the device for the bending, compressing, and shearing deformations [Equation (5)], and to the tension stiffness of the device for the shearing and stretching deformations [Equation (9)]. Figures 52a and 52b plot the device's bending stiffness $(EI)_{eq}$ and tension stiffness $(Eh)_{eq}$ as a function of the device thickness for the three types of substrate materials, respectively. It is assumed that $f = 1$ ($f = 0$), which corresponds to the maximum (minimum) bending and tension stiffnesses that arise from the fill factor f [Equations (8) and (11)]. Clearly, the bending and tension stiffnesses of PDMS-based devices are uniform across the thicknesses and are much smaller than those of parylene- and polyimide-based devices. The fill factor f has a more prominent effect on the tension stiffness than on the bending stiffness. Therefore, it is expected that PDMS-based MEAs would cause a lower degree of inflammation and foreign body responses in the body. So far, no systemic experimental studies have been conducted to compare the long-term *in vivo* performances of these substrate materials, thus we are looking forward to experimental verification of this hypothesis.

To summarize, by reducing the implant's stiffness, the stresses induced by micromotions between the implant and the surrounding tissue are expected to decrease, and the chance of trauma to the tissue and mechanical damage to the device can both be lowered. PDMS excels parylene and polyimide in its low and uniform bending and tension stiffnesses across all device thicknesses.

A.4   Other Properties

As shown in Table 7, all the three polymers are good insulators with comparable electrical properties. Moreover, PDMS is optically clear and colorless. This provides an additional

advantage for placing the MEA and visualizing the underlying tissue during surgery and experiment. A comparison on the long-term biocompatibility of the three polymers is beyond the scope of this current mechanics study and is subjected to future investigations.

A.5 Summary

In this appendix, I used mechanics analyses to compare the performances of flexible MEAs fabricated using the three commonly used substrate materials—parylene, polyimide, and PDMS—in the context of neural surface interfacing applications. The compliant PDMS material excels the other two stiffer materials, i.e. parylene and polyimide, in many mechanical aspects. The conclusion supports the claim that softer MEAs make better neural interfaces.

APPENDIX B

A STRETCHABLE MICRONEEDLE-ELECTRODE ARRAY

In addition to the development efforts on surface sMEAs presented in the main texts, in this appendix, I describe a low-cost, easy-fabricating stretchable microneedle-electrode array (sMNEA) for intramuscular recording and stimulation. We are currently comparing EMG recorded intramuscularly using this type of sMNEA to that recorded epimysially using a surface sMEA. This work appears in Ref. [51].

B.1   Introduction

The application of intramuscular electrode technology to a large muscle area, with the inter-electrode distance maintained, has the potential to increase both the controllability and observability of the muscle. Intramuscular recordings have been the classical technique for investigating the properties of individual motor units. However, individually implanted electrodes fail to preserve the relative electrode positions from experiment to experiment, and the implantation process becomes cumbersome when the number of electrodes increases. The widely used microfabricated microneedle electrode arrays [135, 134, 108, 15, 60] are, however, constrained in a small interfacing area. While flexible electrode arrays [74, 109, 85, 116, 93, 128, 63, 52] can conform to a large area, their interface is restricted to the muscle surface, thus access to the signal sources or the stimulating targets is limited and consequently the recording resolution or spatial selectivity is low. Microneedle probes have also been fabricated using a flexible substrate [40, 112], but the interfacing area is still very limited. Devices that incorporate microneedles at discrete locations on a large-area flexible substrate have been rare, presumably due to the difficulty in fabricating such a structure with microfabrication techniques.

Inspired by previous work of embedding nail-head pins in a PDMS substrate [131], we have developed a simple method for fabricating stretchable microneedle-electrode arrays

118
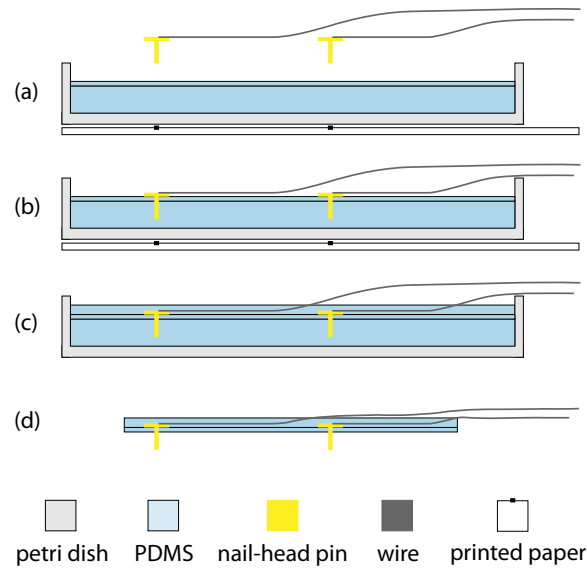
Figure 53: Fabrication procedures.

(sMNEAs). The sMNEA is formed by embedding micro-sized, gold-coated nail-head pins between two PDMS layers. The nail-head pins function as microneedle electrodes, which are sharp enough to penetrate a muscle easily, while the PDMS substrate holds each electrode at a fixed position, conforms to the muscle surface curvature, and stretches along with muscle deformation. Our method produces sMNEAs that are moderate in precision, medium in scale, and low in cost, with a fast turnaround time. And with microneedle electrodes distributed across a large stretchable substrate, our sMNEA is suitable for large-area, multichannel intramuscular recording and stimulation. In this work, we describe the fabrication of our sMNEA, demonstrate its application to a muscle, and characterize its operation. The resulting device is resilient to bending and stretching, and its placement on and electrode insertion into a muscle are easy and efficient.

B.2 Methodology

B.2.1 Device Fabrication

The fabrication requires no cleanroom facilities and can be performed in a regular lab environment. If baking is employed to cure the PDMS, the turnaround time can be within hours.

119

B.2.1.1 Preparation

PDMS (Sylgard 184, Dow Corning) elastomer base was mixed with curing agent at a 10 : 1 weight ratio, and the mixture was left at room temperature for at least 40 minutes to let air bubbles rise out. A bulk PDMS substrate was cured in a petri dish either by leaving the prepolymer at room temperature for more than 48 hours or by baking it in a 60 ℃ oven for one hour. A fine insulated copper wire (93 μm total diameter, 40 AWG, Essex Soderon 155) was exposed at the tip and soldered on the head of each gold-coated nail-head pin (254 μm tip diameter, 762 μm head diameter, and 1.778 mm pin length, Mill-Max MGF). Subsequent insulation of the nail-head pins, except for the tips, with parylene or polyimide is optional. A microscope glass slide (75 x 50 x 1 mm, Fisherbrand, Fisher Scientific) was coated with a sacrificial releasing layer. A thin PDMS film (e.g. 150 μm thick) was then cured on the slide and released. The pattern of electrode positions was drawn on a computer, printed onto a piece of paper, and cut out for guiding insertion of the pins into the bulk PDMS substrate.

B.2.1.2 Fabrication Process

The cut-out pattern was taped at the bottom of the petri dish in which the bulk PDMS substrate had been cured and the thin PDMS film was laid on the surface of the bulk PDMS (no sacrificial layer in between is needed). Microholes were made in the PDMS assembly, using a 200-μm–diameter needle, according to the cut-out pattern; and a nail-head pin was inserted into each hole with the connecting wire placed on the PDMS surface and oriented accordingly (Figures 53a and 53b).

Once pin insertion and wire placement had been completed, PDMS prepolymer was poured into the petri dish to encapsulate the pins and wires until the PDMS reached the desired thickness (Figure 53c). Finally, the encapsulation PDMS layer was given time to cure, and the device was cut out using a razor blade and peeled off the bulk PDMS substrate in the petri dish (Figure 53d). Separation of the device at the interface between the laid thin PDMS film and the bulk PDMS substrate was easy after fabrication.

B.2.2 Impedance Spectroscopy

Electrode impedance spectra of a sample sMNEA were measured using a spectrum analyzer (SRS Dynamic Signal Analyzer, SR785). A custom-made comparing circuit was used to interface each electrode channel to the spectrum analyzer. The array was flipped over and placed on the surface of a saline bath (HBSS 1X, Gibco) in a petri dish. The hydrophobic nature of the PDMS material allowed the device to float on the saline surface. One probe was connected to a silver wire that was dipped into the bath, while the other probe was hooked to one of the connector pins. A sine sweep from 10 Hz to 20 kHz, with a peak-peak voltage amplitude of 100 mV, was applied across the probes and the impedance spectrum measured. This was performed with each of the connector pins, where each pin corresponded to one of the 16 electrode channels or the reference electrode channel.

B.2.3 Saline Bath Recording

A function generator was used to apply a 20 Hz sine wave, with a peak-peak amplitude of 50 mV, through a silver wire into a saline bath (PBS 10X, Mediatech) in a petri dish. The sample sMNEA was flipped over and placed on the surface of the saline bath. Three electrodes were randomly selected from the array, two of which were configured as a bipolar recording channel and the other as a monopolar recording channel. These electrode channels were connected to an instrumentation amplifier (Model 440, Brownlee Precision). The gain of the bipolar recording channel was set to 20, while that of the monopolar channel was set to 1. Data was collected through a dSPACE system (RTI1104, dSPACE).

B.3 Results

B.3.1 Fabrication Results

An sMNEA with 16 recording electrodes and one reference electrode was fabricated and characterized. Figure 54 shows the 16-channel sMNEA. The thickness of the device substrate is ∼1.5 mm, with each microneedle electrode protruding out of the plane by ∼1.6 mm. Figure 54a corresponds to the fabrication stage of Figure 53c, in which the nail-heads and leads were encapsulated by a second PDMS layer poured into the petri dish and cured;

(a)

(b)

(c)

(d)
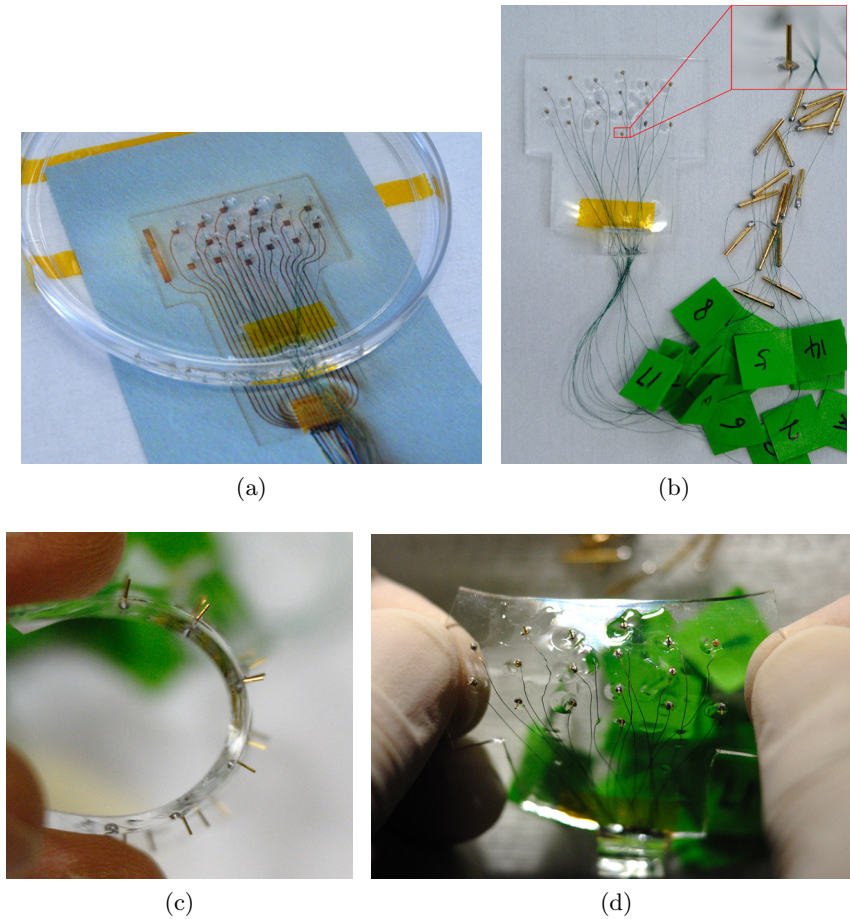
Figure 54: Fabrication results. (a) After fabrication, but before cutting out and detaching the device from the petri dish. The yellow Kapton tape in the petri dish had been used to fix the wires onto the substrate surface before the PDMS prepolymer was pored in. (b) The fully packaged device. The width of the sMNEA head is 4.2 cm. Inset shows a close-up view of one of the microneedle electrodes. (c) Bending of the device. The thickness of the device substrate is ∼1.5 mm, while the protrusion of the electrodes is ∼1.6 mm. (d) Uniaxial stretching of the device (∼ 15% stain).

Figure 54b corresponds to the stage of Figure 53d, in which the array was cut out along the outline on the printed paper and peeled off the bulk PDMS substrate in the petri dish. Each electrode lead was then soldered to a connector pin and labeled. The device retained its integrity after bending and stretching (Figures 54c and 54d), as confirmed by electrode impedance measurements afterwards. Because the metal components—nail-head pins and wires—are many orders of magnitude stiffer than the PDMS substrate, most of the strain generated during deformation is taken by the elastomeric material, while the rigid components bear very little strain.

(a)

(b)
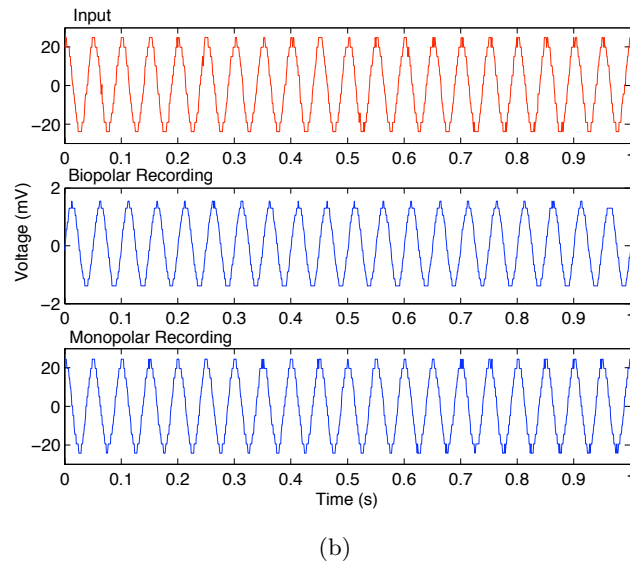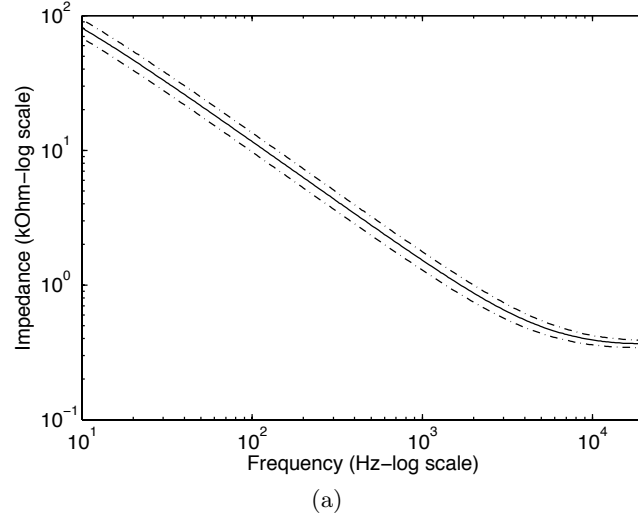
Figure 55: *In vitro* characterization. (a) Average electrode impedance spectrum of the sMNEA. Solid line, average spectrum of the 16 recording electrodes and the reference electrode; dash-dotted lines, one standard deviation from the average. (b) Saline bath recording of sine waves. Top red, input sine signal into the saline bath from a function generator; middle, a bipolar recording; bottom, a monopolar recording.

B.3.2 Characterization and Evaluation

Figure 55a shows the average electrode impedance spectrum of the 16 recording electrodes and the reference electrode. The electrode pins of this sample had not been insulated by polymer coating (e.g. parylene). The average electrode impedance at 1 kHz is 1.53 $k\Omega$. The recording capability of the sMNEA was tested by recording sine waves from a saline bath using both bipolar and monopolar electrode configurations. Figure 55b shows sample

123
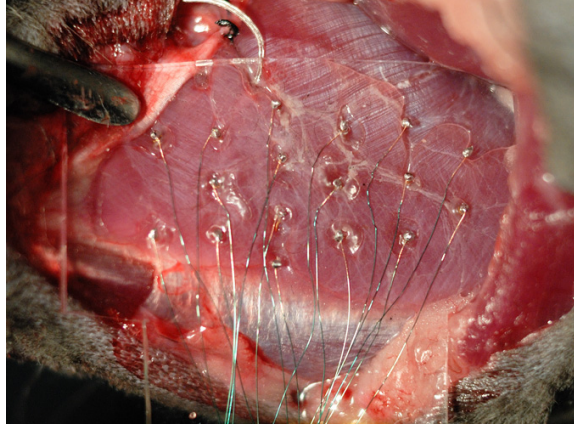
Figure 56: Successful insertion of the microneedle electrodes into the MG muscle of cat after death.

plots of these recorded signals as well as the input signal. Note that the signal recorded using a bipolar configuration has an amplitude of ∼1.5 mV, which is in the same order of magnitude as that of intramuscularly recorded electromyogram (EMG) signals. To test the capability of penetration, the sMNEA was placed on the medial gastrocnemius muscle of a cat's hind limb, and a small force was applied to the back of each electrode area sequentially using a surgical tool; insertion of the electrode pins into the muscle was easy and efficient, as demonstrated in Figure 56.

B.4   Discussion

B.4.1   Electrode Geometry

There is a diverse collection of nail-head pins provided by Mill-Max MGF Corp and other suppliers. Nail-head pins with suitable geometry parameters, such as diameter, length, etc., can be selected to best fit the needs of an application. Electrode diameter and protrusion height can be customized by using nail-head pins with the desired tip diameter and pin length respectively. For example, a surface electrode array can be made by using short pins in place of long pins, such that the pin tips only slightly protrude from the PDMS surface.

B.4.2   Insulation of Electrode Shaft

The recording resolution and spatial selectivity of the sMNEA may be improved by insulating the pin shafts with a parylene or polimide coating prior to fabrication, while keeping the pin tip clear of insulating material.

124

B.4.3   Increase of Device Compliance

Devices fabricated from the presented procedure are thick (e.g., at least a few hundred micrometers) due to constraints from dimensions of the nail heads, solder balls, and connecting wires. As a result, device conformability is compromised. However, holes can be punched in spare areas of the PDMS substrate to increase the device compliance.

B.4.4   Advantages

Although this method of fabrication limits the electrode count and the precision of sMNEA parameters, it has some obvious advantages: (1) Costs of materials and fabrication are low. No special equipment is required and no cleanroom environment is needed. (2) The fabrication method is easy and simple. No special skills/trainings are required. (3) The turnaround time is short. If baking is employed to cure the PDMS, the turnaround time can be within hours. (4) This type of sMNEA offers the unique utility of large-area, deep-source access by distributing microneedle electrodes discretely on a large stretchable substrate that can conform to a surface of complex curvatures and deform. And (5) transparency of the PDMS material is helpful both during fabrication and application.

B.4.5   Applications

We are currently comparing EMG signals recorded intramuscularly using an sMNEA to those recorded epimysially using a surface sMEA in acute feline preparations (see the companion paper). The expected data will help characterize the new multichannel epimysial recording technique and will shed light on the differences between EMG signals recorded intramuscularly and epimysially. Besides recording motor unit activity, this type of sMNEA can also be used to activate a muscle using distributed stimulation protocols. There are also other applications that can benefit from this type of device, e.g., large-area multichannel intracortical recordings.

B.5 Summary

We have developed a simple and low-cost method for fabricating sMNEAs. Devices with a moderate precision and a medium-scale electrode number can easily be fabricated in a regular lab environment within hours. The resulting device is robust to bending and stretching, and insertion of the microneedle electrodes into soft tissues is easy and efficient. Potential applications include intramuscular recording and stimulation, intracortical recording, etc., in which large-area, deep-source neural interfacing is desired.

REFERENCES

[1] ADREGA, T. and LACOUR, S. P., "Stretchable gold conductors embedded in PDMS and patterned by photolithography: fabrication and electromechanical characterization," *J. Micromech. Microeng.*, vol. 20, p. 055025, 2010.

[2] AHUJA, A. K., BEHREND, M. R., WHALEN, J. J., HUMAYUN, M. S., and WEILAND, J. D., "The dependence of spectral impedance on disc microelectrode radius," *IEEE Trans. Biomed. Eng.*, vol. 55, pp. 1457–1460, April 2008.

[3] AKERS, J. M., PECKHAM, P. H., KEITH, M. W., and MERRITT, K., "Tissue response to chronically stimulated implanted epimysial and intramuscular electrodes," *IEEE Trans. Rehabil. Eng.*, vol. 5, no. 2, pp. 207–220, 1997.

[4] AL-HALHOULI, A. T., KAMPEN, I., KRAH, T., and BUTTGENBACH, S., "Nanoindentation testing of SU-8 photoresist mechanical properties," *Microelectronic Engineering*, vol. 85, pp. 942–944, 2008.

[5] AL-SARAWI, S. F., ABBOTT, D., and FRANZON, P. D., "A review of 3-D packaging technology," *IEEE Transactions on Components, Pakcaging, and Manufacturing Technology–Part B*, vol. 21, no. 1, pp. 2–14, 1998.

[6] AXISA, F., BROSTEAUX, D., DE LEERSNYDER, E., BOSSUYT, F., VANFLETEREN, J., HERMANS, B., and PUERS, R., "Biomedical stretchable sytems using MID based stretchable electronics technology," *Proceedings of the 29th Annual International Conference of the IEEE EMBS*, pp. 5687–5690, 2007.

[7] BALGUDE, A. P., YU, X., SZYMANSKI, A., and BELLAMKONDA, R. V., "Agarose gel stiffness determines rate of DRG neurite extension in 3D cultures," *Biomaterials*, vol. 22, pp. 1077–1084, 2001.

[8] BARTHÉLEMY, D., LEBLOND, H., PROVENCHER, J., and ROSSIGNOL, S., "Nonlocomotor and locomotor hindlimb responses evoked by electrical microstimulation of the lumbar cord in spinalized cats," *J. Neurophysiol.*, vol. 96, no. 6, pp. 3273–3292, 2006.

[9] BAUER, C. E., "Micropackaging for multi-chip modules," in *Proc. of ISHM Int. Symp. Microelectronics*, pp. 613–616, 1992.

[10] BOGDANOV, A. L., "Use of su-8 negative photoresist for optical mask manufacturing," *Proc. SPIE*, vol. 3999, p. 1215, 2000.

[11] BORKHOLDER, D. A., *Cell based biosensors using microelectrodes*. PhD thesis, Stanford University, 1998.

[12] BURNS, J. A., AULL, B. F., CHEN, C. K., CHEN, C.-L., KEAST, C. L., KNECHT, J. M., SUNTHARALINGAM, V., WARNER, K., WYATT, P. W., and YOST, D.-R. W., "A wafer-scale 3-D circuit integration technology," *IEEE Trans. Electron Devices*, vol. 53, no. 10, pp. 2507–2516, 2006.

[13] Butler, J. T. and Bright, V. M., "An embedded overlay concept for microsystems packaging," *IEEE Trans. Adv. Pack.*, vol. 23, pp. 617 – 622, November 2000.

[14] C.-X. Liu and Choi, J., "Patterning conductive PDMS nanocomposite in an elastomer using microcontact printing," *J. Micromech. Microeng.*, vol. 19, p. 085019, 2009.

[15] Campbell, P. K., Jones, K. E., Huber, R. J., Horch, K. W., and Normann, R. A., "A silicon-based, three-dimensional neural interface: manufacturing processes for an intracortical electrode array," *IEEE Trans. Biomed. Eng.*, vol. 38, pp. 758–768, August 1991.

[16] Carroll, T. L. and Rosen, C. A., "Vocal fold paralysis, unilateral." http://emedicine.medscape.com/article/863779-overview, November 2008.

[17] Ceballos, D., Valero-Cabre, A., Valderrama, E., Schuttler, M., Stieglitz, T., and Navarro, X., "Morphologic and functional evaluation of peripheral nerve fibers regenerated through polyimide sieve electrodes over long-term implantation," *J. Biomed. Mater. Res.*, vol. 60, pp. 517–528, 2002.

[18] Chan, Y. C. and Luk, D. Y., "Effects of bonding parameters on the reliability performance of anisotropic conductive adhesive interconnects for flip-chip-on-flex packages assembly II. Different bonding pressure," *Microelectronics Reliability*, vol. 42, no. 8, pp. 1195–1204, 2002.

[19] Cheng, Y., Lin, C., Wei, D., Loechel, B., and Gruetzner, G., "Wall profile of thick photoresist generated via contact printing," *IEEE J. Microelectromechanical Sys.*, vol. 8, pp. 18–26, 1999.

[20] Cheung, K. C., "Implantable microscale neural interfaces," *Biomed Microdevices*, vol. 9, pp. 923–938, 2007.

[21] Cho, S.-H., Lu, H. M., Cauller, L., Romero-Ortega, M. I., Lee, J.-B., and Hughes, G. A., "Biocompatible SU-8-based microprobes for recording neural spike signals from regenerated peripheral nerve fibers," *IEEE Sensors Journal*, vol. 8, no. 11, pp. 1830–1836, 2008.

[22] CIGNA, "Injections for unilateral vocal cord paralysis (UVCP)." Cigna Healthcare Coverage Position, November 2005.

[23] Cui, X., Hetke, J. F., Wiler, J. A., Anderson, D. J., and Martin, D. C., "Electrochemical deposition and characterization of conducting polymer polypyrrole/PSS on multichannel neural probes," *Sensors and Actuators A*, vol. 93, pp. 8–18, 2001.

[24] Cui, X. and Martin, D. C., "Fuzzy gold electrodes for lowering impedance and improving adhesion with electrodeposited conducting polymer films," *Sensors and Actuators A*, vol. 103, pp. 384–394, 2003.

[25] Daum, W., Burdick Jr., W. E., and Fillion, R. A., "Overlay high-density interconnect: a chips-first multichip module technology," *Computer*, vol. 26, pp. 23–29, April 1993.

[26] Dimitrijevic, M. R., Gerasimenko, Y., and Pinter, M. M., "Evidence for a spinal central pattern generator in humans," *Ann. N. Y. Acad. Sci.*, vol. 860, pp. 360–376, 1998.

[27] Divi, V., Pou, A., and Quinn, F. B., "Treatment of unilateral adductor vocal cord paralysis." http://www.utmb.edu/otoref/grnds/VC-paralysis-001108/VC-paralysis-001108.htm, November 2000.

[28] Duffy, D. C., Jackman, R. J., Vaeth, K. M., Jensen, K. F., and Whitesides, G. M., "Patterning electroluminescent materials with feature sizes as small as $5\mu m$ using elastomeric membranes as masks for dry lift-off," *Adv. Mater.*, vol. 11, no. 7, pp. 546–552, 1999.

[29] Edell, D. J., "A peripheral nerve information transducer for amputees: long-term multichannel recordings from rabbit peripheral nerves," *IEEE Trans. Biomed. Eng.*, vol. 33, pp. 203–214, 1986.

[30] Elliott, D. J., *Integrated Circuit Fabrication Technology.* McGraw-Hill, New York, USA, 2nd ed., 1989.

[31] Fan, J.-L., "Biomechanics of peripheral nerves - an in vivo study," Master's thesis, National Cheng Kung University, 2003.

[32] Fillion, R., Wojnarowski, R., Saia, R., and Kuk, D., "Demonstration of a chip scale chip-on-flex technology," in *Proc. of Int. Conf. on Multichip Modules*, vol. 2794, pp. 351–356, 1996.

[33] FitzGerald, J. J., Lacour, S. P., McMahon, S. B., and Fawcett, J. W., "Microchannels as axonal amplifiers," *IEEE Trans. Biomed. Eng.*, vol. 55, no. 3, pp. 1136–1146, 2008.

[34] FitzGerald, J. J., Lacour, S. P., McMahon, S. B., and Fawcett, J. W., "Microchannel electrodes for recording and stimulation: in vitro evaluation," *IEEE Trans. Biomed. Eng.*, vol. 56, no. 5, pp. 1524–1534, 2009.

[35] Flanagan, L. A., Ju, Y.-E., Marg, B., Osterfield, M., and Janmey, P. A., "Neurite branching on deformable substrates," *Neuroreport.*, vol. 13, no. 18, pp. 2411–2415, 2002.

[36] Franks, W., Schenker, W., Schmutz, P., and Hierlemann, A., "Impedance characterization and modeling of electrodes for biomedical applications," *IEEE Trans. Biomed. Eng.*, vol. 52, pp. 1295–1302, 2005.

[37] Garra, J., Long, T., Currie, J., Schneider, T., White, R., and Paranjape, M., "Dry etching of polydimethylsiloxane for microfluidic systems," *J. Vac. Sci. Technol. A*, vol. 20, no. 3, pp. 975–982, 2002.

[38] Garrou, P., "Wafer level chip scale packaging (WL-CSP): an overview," *IEEE Trans. Adv. Pack.*, vol. 23, no. 2, pp. 198–205, 2000.

[39] Gerasimenko, Y. P., Lavrov, I. A., Bogacheva, I. N., Shcherbakova, N. A., Kucher, V. I., and Musienko, P. E., "Formation of locomotor patterns in decerebrate cats in conditions of epidural stimulation of the spinal cord," *Neurosci. Behav. Physiol.*, vol. 35, no. 3, pp. 291–298, 2005.

[40] Gonzalez, C. and Rodriguez, M., "A flexible perforated microelectrode array probe for action potential recording in nerve and muscle tissues," *J. Neurosci. Methods*, vol. 72, pp. 189–195, April 1997.

[41] Grandjean, P. A. and Mortimer, J. T., "Recruitment properties of monopolar and bipolar epimysial electrodes," *Ann. Biomed. Eng.*, vol. 14, pp. 53–66, 1986.

[42] Graudejus, O., Gorrn, P., and Wagner, S., "Controlling the morphology of gold films on poly(dimethylsiloxane)," *Appl. Mater. Interfaces*, vol. 2, no. 7, pp. 1927 – 1933, 2010.

[43] Gray, D. S., Tien, J., and Chen, C. S., "High-conductivity elastomeric electronics," *Adv. Mater.*, vol. 16, no. 5, pp. 393–397, 2004.

[44] Guiraud, D., Stieglitz, T., Taroni, G., and Divoux, J.-L., "Original electronic design to perform epimysial and neural stimulation in paraplegia," *J. Neural Eng.*, vol. 3, pp. 276–286, 2006.

[45] Guo, L., Kitashima, L. J., Villari, C. R., Klein, A. M., and DeWeerth, S. P., "Muscle surface recording and stimulation using integrated PDMS-based microelectrode arrays: Recording-triggered stimulation for prosthetic purposes," in *Proc. of IEEE BioCAS*, 2009.

[46] Guo, L., Clements, I. P., Li, D., Bellamkonda, R. V., and DeWeerth, S. P., "A conformable microelectrode array (cMEA) with integrated electronics for peripheral nerve interfacing," in *Proc. of IEEE BioCAS*, 2010.

[47] Guo, L. and DeWeerth, S. P., "Implementation of integratable PDMS-based conformable microelectrode arrays using a multilayer wiring interconnect technology," in *Proc. of IEEE EMBC*, pp. 1619–1622, 2009.

[48] Guo, L. and DeWeerth, S. P., "PDMS-based conformable microelectrode arrays with selectable novel 3-D microelectrode geometries for surface stimulation and recording," in *Proc. of IEEE EMBC*, pp. 1623–1626, 2009.

[49] Guo, L. and DeWeerth, S. P., "An effective lift-off method for patterning high-density gold interconnects on an elastomeric substrate," *Small*, vol. 6, no. 24, pp. 2847–2852, 2010.

[50] Guo, L. and DeWeerth, S. P., "High-density stretchable electronics: Toward an integrated multilayer composite," *Adv. Mater.*, vol. 22, no. 36, pp. 4030–4033, 2010.

[51] Guo, L., Guvanasen, G., Tuthill, C., Nichols, T. R., and DeWeerth, S. P., "A low-cost, easy-fabricating stretchable microneedle-electrode array for intramuscular recording and stimulation," in *Proc. of IEEE EMBS Conf. on Neural Engineering*, 2011.

[52] Guo, L., Meacham, K. W., and DeWeerth, S. P., "A PDMS-based conical-well microelectrode array for surface stimulation of neural tissues," *IEEE Trans. Biomed. Eng.*, vol. 57, no. 10, pp. 2485–2494, 2010.

[53] HEUSCHKEL, M. O., FEJTL, M., RAGGENBASS, M., BERTRAND, D., and RENAUD, P., "A three-dimensional multi-electrode array for multi-site stimulation and recording in acute brain slices," *J. Neurosci. Methods*, vol. 114, no. 2, pp. 135–148, 2002.

[54] HOCHMAN, S. and SCHMIDT, B. J., "Whole cell recordings of lumbar motoneurons during locomotor-like activity in the in vitro neonatal rat spinal cord," *J Neurophysiol*, vol. 79, pp. 743–752, February 1998.

[55] HORCH, K. W. and DHILLON, G. S., eds., *Neuroprosthetics: Theory and Practice*, vol. 2 of *Series on Bioengineering & Biomedical Engineering*. World Scientific, 2004.

[56] HUGHES, A. C., GUO, L., and DEWEERTH, S. P., "Interleaved multichannel epimysial stimulation for eliciting smooth contraction of muscle with reduced fatigue," in *Proc. of IEEE EMBC*, 2010.

[57] ICHIYAMA, R. M., GERASIMENKO, Y. P., ZHONG, H., ROY, R. R., and EDGERTON, V. R., "Hindlimb stepping movements in complete spinal rats induced hindlimb stepping movements in complete spinal rats induced by epidural spinal cord stimulation," *Neuroscience Letters*, vol. 383, pp. 339–344, 2005.

[58] IWAHARA, T., ATSUTA, Y., GARCIA-RILL, E., and SKINNER, R. D., "Spinal cord stimulation-induced locomotion in the adult cat," *Brain Res. Bull.*, vol. 28, no. 1, pp. 99–105, 1992.

[59] JO, B. H., LERBERGHE, L. V., MOTSEGOOD, K. M., and BEEBE, D. J., "Three-dimensional micro-channel fabrication in polydimethylsiloxane (pdms) elastomer," *Journal of Microelectromechanical Systems*, vol. 9, no. 1, pp. 76–81, 2000.

[60] JONES, K. E., CAMPBELL, P. K., and NORMANN, R. A., "A glass/silicon composite intracortical electrode array," *Ann. Biomed. Eng.*, vol. 20, pp. 423–437, 1992.

[61] JOSHI, R., "Chip on glass—interconnect for row/column driver packaging," *Microelectronics Journal*, vol. 29, no. 6, pp. 343–349, 1998.

[62] KIEHN, O. and KJAERULFF, O., "Spatiotemporal characteristics of 5-HT and dopamine-induced rhythmic hindlimb activity in the in vitro neonatal rat," *J. Neurophysiol.*, vol. 75, no. 4, pp. 1472–1482, 1996.

[63] KIM, D.-H., VIVENTI, J., AMSDEN, J. J., XIAO, J., VIGELAND, L., KIM, Y.-S., BLANCO, J. A., PANILAITIS, B., FRECHETTE, E. S., CONTRERAS, D., KAPLAN, D. L., OMENETTO, F. G., HUANG, Y., HWANG, K.-C., ZAKIN, M. R., LITT, B., and ROGERS, J. A., "Dissolvable films of silk fibroin for ultrathin conformal bio-integrated electronics," *Nat. Mater.*, vol. 9, pp. 511–517, 2010.

[64] KIM, K. S., ZHAO, Y., JANG, H., LEE, S. Y., KIM, J. M., KIM, K. S., AHN, J., KIM, P., CHOI, J., and HONG, B. H., "Large-scale pattern growth of graphene films for stretchable transparent electrodes," *Nature*, vol. 457, pp. 706–710, 2009.

[65] KIM, K., PARK, D. S., LU, H. M., CHE, W., KIM, K., LEE, J.-B., and AHN, C. H., "A tapered hollow metallic microneedle array using backside exposure of su-8," *J. Micromech. Microeng.*, vol. 14, pp. 597–603, 2004.

[66] Kotov, N. A., Winter, J. O., Clements, I. P., Jan, E., Timko, B. P., Campidelli, S., Pathak, S., Mazzatenta, A., Lieber, C. M., Prato, M., Bellamkonda, R. V., Silva, G. A., Kam, N. W. S., Patolsky, F., and Ballerini, L., "Nanomaterials for neural interfaces," *Adv. Mater.*, vol. 21, pp. 1–35, 2009.

[67] Kovacs, G. T. A., Storment, C. W., and Rosen, J. M., "Regeneration microelectrode array for peripheral nerve recording and stimulation," *IEEE Trans. Biomed. Eng.*, vol. 39, no. 9, pp. 893–902, 1992.

[68] Kunnavakkam, M. V., Houlihan, F. M., Schlax, M., Liddle, J. A., Kolodner, P., Nalamasu, O., and Rogers, J. A., "Low-cost, low-loss microlens arrays fabricated by soft-lithography replication process," *Appl. Phys. Lett.*, vol. 82, pp. 1152–1154, 2003.

[69] Lacour, S. P., Chan, D., Wagner, S., Li, T., and Suo, Z., "Mechanisms of reversible stretchability of thin metal films on elastomeric substrates," *Appl. Phys. Lett.*, vol. 88, p. 204103, 2006.

[70] Lacour, S. P., Jones, J. E., Wagner, S., Li, T., and Suo, Z., "Stretchable interconnects for elastic electronic surfaces," *Proc. of the IEEE*, vol. 93, pp. 1459–1467, 2005.

[71] Lacour, S. P., Tsay, C., Wagner, S., Yu, Z., and Morrison, B., "Stretchable micro-electrode arrays for dynamic neuronal recording of in vitro mechanically injured brain," *Proc. of the 4th IEEE Conference on Sensors*, pp. 617–620, 2005.

[72] Lacour, S. P., Atta, R., FitzGerald, J. J., Blamire, M., Tarte, E., and Fawcett, J., "Polyimide micro-channel arrays for peripheral nerve regenerative implants," *Sensors and Actuators A: Physical*, vol. 147, pp. 456–463, 2008.

[73] Lacour, S. P., Wagner, S., Huang, Z., and Suo, Z., "Stretchable gold conductors on elastomeric substrates," *Appl. Phys. Lett.*, vol. 82, no. 15, pp. 2404–2406, 2003.

[74] Lapatki, B. G., Dijk, J. V., Jonas, I. E., Zwarts, M. J., and Stegeman, D. F., "A thin, flexible multielectrode grid for high-density surface EMG," *J. Appl. Physiol.*, vol. 96, pp. 327–336, January 2004.

[75] Larynx - Anatomy. http://ent4students.blogspot.com/2008/04/larynx.html.

[76] Lau, J. H., ed., *Chip On Board: Technology for Multichip Modules*. Springer, 1994.

[77] Li, T., Huang, Z. Y., Xi, Z. C., Lacour, S. P., Wagner, S., and Suo, Z., "Delocalizing strain in a thin metal film on a polymer substrate," *Mechanics of Materials*, vol. 37, pp. 261–273, 2005.

[78] Li, T., Huang, Z., Suo, Z., Lacour, S. P., and Wagner, S., "Stretchability of thin metal films on elastomer substrates," *Appl. Phys. Lett.*, vol. 85, no. 16, pp. 3435–3437, 2004.

[79] Li, T. and Suo, Z., "Deformability of thin metal films on elastomer substrates," *International Journal of Solids and Structures*, vol. 43, pp. 2351–2363, 2006.

[80] Li, T. and Suo, Z., "Ductility of thin metal films on polymer substrates modulated by interfacial adhesion," *International Journal of Solids and Structures*, vol. 44, pp. 1696–1705, 2007.

[81] Lin, I.-K., Liao, Y.-M., Chen, K.-S., and Zhang, X., "Viscoelastic characterization of soft micropillars for cellular mechanics study," in *Proc. 12th Int. Conf. on Miniaturized Systems for Chemistry and Life Sciences*, pp. 278–280, 2008.

[82] Linder, V., Gates, B. D., Ryan, D., Parviz, B. A., and Whitesides, G. M., "Water-soluble sacrificial layers for surface micromachining," *Small*, vol. 1, pp. 730–736, 2005.

[83] Lu, J.-Q., Kwon, Y., Rajagopalan, G., Gupta, M., McMahon, J., Lee, K.-W., Kraft, R. P., McDonald, J. F., Cale, T. S., Gutmann, R. J., Xu, B., Eisenbraun, E., Castracane, J., and Kaloyeros, A., "A wafer-scale 3D IC technology platform using dielectric bonding glues and copper damascene patterned inter-wafer interconnects," in *Proc. of the IEEE Int. Conf. on Interconnect Technology*, pp. 78–80, 2002.

[84] Maathuis, E. M., Drenthen, J., van Dijk, J., Visser, G. H., and Blok, J. H., "Motor unit tracking with high-density surface EMG," *Journal of Electromyography and Kinesiology*, vol. 18, no. 6, pp. 920–930, 2008.

[85] Maghribi, M., Hamilton, J., Polla, D., Rose, K., Wilson, T., and Krulevitch, P., "Stretchable micro-electrode array [for retinal prosthesis]," in *2nd Annual International IEEE-EMB Special Topic Conference on Microtechnologies in Medicine & Biology*, pp. 80–83, May 2002.

[86] Magnuson, D. S. and Trinder, T. C., "Locomotor rhythm evoked by ventrolateral funiculus stimulation in the neonatal rat spinal cord in vitro," *J. Neurophysiol.*, vol. 77, no. 1, pp. 200–206, 1997.

[87] Mata, A., Fleischman, A. J., and Roy, S., "Characterization of polydimethylsiloxane (PDMS) properties for biomedical micro/nanosystems," *Biomed. Microdevices*, vol. 7, pp. 281–293, 2005.

[88] McClain, M. A., Clements, I. P., Shafer, R. H., Bellamkonda, R. V., LaPlaca, M. C., and Allen, M. G., "Highly-compliant, microcable neuroelectrodes fabricated from thin-film gold and pdms," *Biomed. Microdevices*, 2011, advanced online publication.

[89] McClain, M. A., LaPlaca, M. C., and Allen, M. G., "Spun-cast micromolding for etchless micropatterning of electrically functional PDMS structures," *J. Micromech. Microeng.*, vol. 19, p. 107002, September 2009.

[90] McCreery, D. B., Agnew, W. F., Yuen, T. G., and Bullara, L., "Charge density and charge per phase as cofactors in neural injury induced by electrical stimulation," *IEEE Trans. Biomed. Eng.*, vol. 37, pp. 996–1001, October 1990.

[91] McDonald, J. C. and Whitesides, G. M., "Poly(dimethylsiloxane) as a material for fabricating microfluidic devices," *Acc. Chem. Res.*, vol. 35, no. 7, pp. 491–499, 2002.

[92] McDonnall, D., Clark, G. A., and Normann, R. A., "Interleaved, multisite electrical stimulation of cat sciatic nerve produces fatigue-resistant, ripple-free motor responses," *IEEE Trans. Neural. Syst. Rehabil. Eng.*, vol. 12, no. 2, pp. 208–215, 2004.

[93] Meacham, K. W., Giuly, R. J., Guo, L., Hochman, S., and DeWeerth, S. P., "A lithographically-patterned, elastic multi-electrode array for surface stimulation of the spinal cord," *Biomedical Microdevices*, vol. 10, pp. 259–269, April 2008.

[94] Meacham, K. W., *Selective surface activation of motor circuitry in the injured spinal cord.* PhD thesis, Georgia Institute of Technology, 2008.

[95] Merletti, R., Holobar, A., and Farina, D., "Analysis of motor units with high-density surface electromyography," *Journal of Electromyography and Kinesiology*, vol. 18, no. 6, pp. 879–890, 2008.

[96] Meyer, R. D., Cogan, S. F., Nguyen, T. H., and Rauh, R. D., "Electrodeposited iridium oxide for neural stimulation and recording electrodes," *IEEE Trans. Neural Syst. Rehab. Eng.*, vol. 9, pp. 2–11, March 2001.

[97] MicroChem, "Product data sheet."

[98] Millet, L. J., Stewart, M. E., Nuzzo, R. G., and Gillette, M. U., "Guiding neuron development with planar surface gradients of substrate cues deposited using microfluidic devices," *Lab Chip*, vol. 10, pp. 1525–1535, 2010.

[99] Minev, I. R. and Lacour, S. P., "Impedance spectroscopy on stretchable microelectrode arrays," *Appl. Phys. Lett.*, vol. 97, p. 043707, 2010.

[100] National Institute on Deafness and Other Communication Disorders (NIDCD), "Vocal cord paralysis." http://www.nidcd.nih.gov/health/voice/vocalparal.asp, June 1999.

[101] Navarro, X., Calvet, S., Rodriguez, F. J., Stieglitz, T., Blau, C., Buti, M., Valderrama, E., and Meyer, J. U., "Stimulation and recording from regenerated peripheral nerves through polyimide sieve electrodes," *J. Peripher. Nerv. Syst.*, vol. 3, pp. 91–101, 1998.

[102] Newman, J., "Current distribution on a rotating disk below the limiting current," *J. Electrochem. Soc.*, vol. 113, pp. 1235–1241, December 1966.

[103] Ng, L. H., "Economic impact of processing technologies on thin film MCMs," in *Proc. of the 42nd Electronic Components and Technology Conf.*, pp. 1042–1045, 1992.

[104] Nicolelis, M. A., Ghazanfar, A. A., Stambaugh, C. R., Oliveira, L. M., Laubach, M., Chapin, J. K., Nelson, R. J., and Kaas, J. H., "Simultaneous encoding of tactile information by three primate cortical areas," *Nat Neurosci*, vol. 1, no. 7, pp. 621–630, 1998.

[105] nyee. http://www.nyee.edu/cfv-neuro.html#unilateral.

[106] Oka, H., Shimono, K., Ogawa, R., Sugihara, H., and Taketani, M., "A new planar multielectrode array for extracellular recording: application to hippocampal acute slice," *J. Neurosci. Methods*, vol. 93, no. 1, pp. 61–67, 1999.

[107] Park, J., Kim, H. S., and Han, A., "Micropatterning of poly(dimethylsiloxane) using a photoresist lift-off technique for selective electrical insulation of microelectrode arrays," *J. Micromech. Microeng.*, vol. 19, p. 065016, May 2009.

[108] Qing, B. and Wise, K. D., "Single-unit neural recording with active microelectrode arrays," *IEEE Trans. Biomed. Eng.*, vol. 48, no. 8, pp. 911–920, 2001.

[109] Rodger, D. C., Fong, A. J., Li, W., Ameri, H., Ahuja, A. K., Gutierrez, C., Lavrov, I., Zhong, H., Menon, P. R., Meng, E., Burdick, J. W., Roy, R. R., Edgerton, V. R., Weiland, J. D., Humayun, M. S., and Tai, Y.-C., "Flexible parylene-based multielectrode array technology for high-density neural stimulation and recording," *Sensors & Actuators: B. Chemical*, vol. 132, no. 2, pp. 449–460, 2008.

[110] Rogers, J. A., Someya, T., and Huang, Y., "Materials and mechanics for stretchable electronics," *Science*, vol. 327, pp. 1603–1607, 2010.

[111] Rosset, S., Niklaus, M., Dubois, P., and Shea, H. R., "Metal ion implantation for the fabrication of stretchable electrodes on elastomers," *Adv. Funct. Mater.*, vol. 19, pp. 470–478, 2009.

[112] Rousche, P. J., Pellinen, D. S., Pivin, D. P., Williams, J. C., Vetter, R. J., and Kipke, D. R., "Flexible polyimide-based intracortical electrode arrays with bioactive capability," *IEEE Trans. Biomed. Eng.*, vol. 48, pp. 361–371, March 2001.

[113] Rubinstein, J. T., Spelman, F. A., Soma, M., and Suesserman, M. F., "Current density profiles of surface mounted and recessed electrodes for neural prostheses," *IEEE Trans. Biomed. Eng.*, vol. 34, pp. 864–875, November 1987.

[114] Rutten, W. L., van Wier, H. J., and Put, J. H., "Sensitivity and selectivity of intraneural stimulation using a silicon electrode array," *IEEE Trans. Biomed. Eng.*, vol. 38, pp. 192–198, 1991.

[115] Schmit, B. D. and Mortimer, J. T., "The tissue response to epimysial electrodes for diaphragm pacing in dogs," *IEEE Trans. Biomed. Eng.*, vol. 44, no. 10, pp. 921–930, 1997.

[116] Schuettler, M., Stiess, S., King, B. V., and Suaning, G. J., "Fabrication of implantable microelectrode arrays by laser cutting of silicone rubber and platinum foil," *J. Neural Eng.*, vol. 2, pp. S121–S128, 2005.

[117] Shay, B. L., Sawchuk, M., Machacek, D. W., and Hochman, S., "Serotonin 5-ht2 receptors induce a long-lasting facilitation of spinal reflexes independent of ionotropic receptor activity," *J. Neurophysiol.*, vol. 94, no. 4, pp. 2867–2877, 2005.

[118] Stieglitz, T., Beutel, H., Blau, C., and Meyer, J. U., "Flexible multichannel microelectrodes with integrated leads for use in neuroprosthetics," in *Biomed Tech (Berl)*, vol. 42 Suppl, pp. 449–450, 1997.

[119] Stieglitz, T., Beutel, H., and Meyer, J., "Micromachined, polyimide-based devices for flexible neural interfaces," *Biomed. Microdevices*, vol. 2, no. 4, pp. 283–294, 2000.

[120] SUANING, G. J., SCHUETTLER, M., ORDONEZ, J. S., and LOVELL, N. H., "Fabrication of multi-layer, high-density micro-electrode arrays for neural stimulation and bio-signal recording," *Proceedings of the 3rd International IEEE EMBS Conference on Neural Engineering*, pp. 5–8, 2007.

[121] SUESSERMAN, M. F., SPELMAN, F. A., and RUBINSTEIN, J. T., "In vitro measurement and characterization of current density profiles produced by nonrecessed, simple recessed, and radially varying recessed stimulating electrodes," *IEEE Trans. Biomed. Eng.*, vol. 38, pp. 401–408, May 1991.

[122] SUO, Y. X. T. L. Z. and VLASSAK, J. J., "High ductility of a metal film adherent on a polymer substrate," *Appl. Phys. Lett.*, vol. 87, p. 161910, 2005.

[123] SUO, Z., MA, E. Y., GLESKOVA, H., and WAGNER, S., "Mechanics of rollable and foldable film-on-foil electronics," *Appl. Phys. Lett.*, vol. 74, no. 8, pp. 1177–1179, 1999.

[124] TAWFICK, S., O'BRIEN, K., and HART, A. J., "Flexible high-conductivity carbon-nanotube interconnects made by rolling and printing," *Small*, vol. 5, pp. 2467–2473, 2009.

[125] TIMPANO, K., "Mechanical characterization of gold thin films for RF-MEMS," in *Virginia Space Grant Consortium Student Research Conference*, 2005.

[126] TUOMIKOSKI, S. and FRANSSILA, S., "Free-standing su-8 microfluidic chips by adhesive bonding and release etching," *Sensors and Actuators A*, vol. 120, pp. 408–415, 2005.

[127] VAN DIJK, J., BLOK, J. H., LAPATKI, B. G., VAN SCHAIK, I., ZWARTS, M. J., and STEGEMAN, D. F., "Motor unit number estimation using high-density surface electromyography," *Clinical Neurophysiology*, vol. 119, no. 1, pp. 33–42, 2008.

[128] VIVENTI, J., KIM, D.-H., MOSS, J. D., KIM, Y.-S., BLANCO, J. A., ANNETTA, N., HICKS, A., XIAO, J., HUANG, Y., CALLANS, D. J., ROGERS, J. A., and LITT, B., "A conformal, bio-interfaced class of silicon electronics for mapping cardiac electrophysiology," *Sci. Transl. Med.*, vol. 2, no. 24, p. ra22, 2010.

[129] VOICEMEDICINE. http://www.voicemedicine.com/unilateral.htm.

[130] WAGNER, S., LACOUR, S. P., JONES, J., HSU, P. I., STURM, J. C., LI, T., and SUO, Z., "Electronic skin: architecture and components," *Physica E*, vol. 25, pp. 326–334, 2004.

[131] WEI, P., TAYLOR, R., DING, Z., HIGGS, G., NORMAN, J. J., PRUITT, B. L., and ZIAIE, B., "A stretchable cell culture platform with embedded electrode array," in *Proc. of IEEE MEMS*, pp. 407–410, 2009.

[132] WEILAND, J. D., LIU, W., and HUMAYUN, M. S., "Retinal prosthesis," *Annu. Rev. Biomed. Eng.*, vol. 7, pp. 361–401, 2005.

[133] WILSON, D., DRISCULL, B., and QUINN, F. B., "Vocal cord paralysis." http://www.utmb.edu/otoref/Grnds/vocalparal.htm, November 1995.

[134] WISE, K. D. and ANGELL, J. B., "A low-capacitance multielectrode probe for neu-rophysiology," *IEEE Trans. Biomed. Eng.*, vol. 22, pp. 212–219, May 1975.

[135] WISE, K. D., ANGELL, J. B., and STARR, A., "An integrated circuit approach to extracellular microelectrodes," *IEEE Trans. Biomed. Eng.*, vol. 17, pp. 238–247, July 1970.

[136] WU, Y. P., ALAM, M. O., CHAN, Y. C., and WU, B. Y., "Dynamic strength of anisotropic conductive joints in flip chip on glass and flip chip on flex packages," *Microelectronics Reliability*, vol. 44, no. 2, pp. 295–302, 2004.

[137] XIA, Y. and WHITESIDES, G. M., "Soft lithography," *Angew. Chem. Int. Ed.*, vol. 37, pp. 550–575, 1998.

[138] YIM, M. J., HWANG, J.-S., KIM, J. G., AHN, J. Y., KIM, H. J., KWON, W., and PAIK, K.-W., "Highly reliable flip-chip-on-flex package using multilayered anisotropic conductive film," *Journal of Electronic Materials*, vol. 33, no. 1, pp. 76–82, 2004.

[139] YIM, M. J., HWANG, J., and PAIK, K. W., "Anisotropic conductive films (ACFs) for ultra-fine pitch chip-on-glass (COG) applications," *International Journal of Adhesion and Adhesives*, vol. 27, no. 1, pp. 77–84, 2007.

[140] ZHANG, W. Y., FERGUSON, G. S., and TATIC-LUCIC, S., "Elastomer-supported cold welding for room temperature wafer-level bonding," *17th IEEE Int. Conf. MEMS*, pp. 741–744, 2004.

VITA

Liang Guo received the B.E. degree in Biomedical Engineering from Tsinghua University (Beijing, China) in 2004. He has been pursuing the Ph.D. degree in the Bioengineering Program at Georgia Institute of Technology (Atlanta, GA) since August 2005. He will continue his research as a postdoctoral associate in the Laboratory of Prof. Robert Langer at Massachusetts Institute of Technology (Boston, MA).

His current research interests focus on reliable, high-throughput neural interfacing technology for neural prosthetics.

Mr. Guo is a Student Member of the IEEE Engineering in Medicine and Biology Society, the Society for Neuroscience, and the Materials Research Society. He is also a Full Member of Sigma Xi.

138